Master's thesis

NTNU
Norwegian University of Science and Technology
Faculty of Natural Sciences
Department of Physics

Håvard Kjellmo Arnestad

A Fast Simulation Method for Ultrasonic Wave Propagation in Coupled Non-parallel Plates

With applications to inversion of pitch-catch through-tubing well logging

Master's thesis in Applied Physics and Mathematics
Supervisor: Erlend Magnus Viggen
June 2021

NTNU
Norwegian University of Science and Technology

Håvard Kjellmo Arnestad

A Fast Simulation Method for Ultrasonic Wave Propagation in Coupled Non-parallel Plates

With applications to inversion of pitch-catch through-tubing well logging

Master's thesis in Applied Physics and Mathematics
Supervisor: Erlend Magnus Viggen
June 2021

Norwegian University of Science and Technology
Faculty of Natural Sciences
Department of Physics

Abstract

Some systems in ultrasonic testing can be approximated as two non-parallel plates coupled by a fluid, where leaky Lamb waves propagate in each plate. This thesis develops a fast and accurate simulation method for such systems. The guiding example is through-tubing well logging, where the aim is to determine the presence of cement through two nested pipes of steel. However, to be able to feasibly determine this through inversion, recent studies have called for a computationally efficient forward model.

The proposed method models each plate using reflection and transmission coefficients. An angular spectrum approach combined with a coordinate rotation method in the wave vector domain handles the multiple reflections between tilted plates.

Two-dimensional propagation is verified against reference simulations in COMSOL Multiphysics. The deviations have known origins and are of little practical significance, and the moderately optimized code executes roughly 10 000 times faster than COMSOL. Three-dimensional propagation is also shown. A mechanism based on Lamb mode conversion between tilted plates is explained for detecting cement types other pitch-catch setups struggle with. As proof of concept, simulation parameters from a COMSOL simulation are successfully retrieved via inversion.

Sammendrag

Enkelte systemer i ultralydtesting kan tilnærmes som to ikke-parallelle plater koblet med et fluid, der utstrålende Lamb-bølger brer seg ut i hver plate. Denne oppgaven utvikler en rask og nøyaktig simuleringsmetode for slike systemer. Det veiledende eksemplet er gjennomrørs brønnlogging, der målet er å fra innsiden fastslå tilstedeværelsen av sement bak to stålrør. For å være i stand til å bestemme dette gjennom inversjon, har nyere studier etterspurt mer effektive beregningsmodeller.

Den foreslåtte metoden modellerer hver plate ved hjelp av refleksjon- og transmisjonskoeffisienter. *Angular spectrum*-metoden kombinert med en koordinatrotasjonsmetode i bølgevektordomenet håndterer multiple refleksjoner mellom skråstilte plater.

Todimensjonal utbredelse er verifisert mot referansesimuleringer i COMSOL Multiphysics. Avvikene har kjent opprinnelse og er av liten praktisk betydning, og den moderat optimaliserte koden er omtrent 10 000 ganger raskere enn COMSOL. Tredimensjonal utbredelse er også vist. En mekanisme basert på konvertering av Lamb-moder mellom skråstilte plater er forklart for oppdagelse av sementtyper som andre *pitch-catch*-oppsett sliter med. For å demonstrere konseptet blir simuleringsparametere fra en COMSOL-simulering vellykket hentet ut via inversjon.

Preface

This master's thesis is submitted for the degree of Master of Science / Sivilingeniør in Applied Physics at the Norwegian University of Science and Technology (NTNU), Department of Physics. The project was conducted under the supervision of Dr. Erlend Magnus Viggen at the Centre for Innovative Ultrasound Solutions (CIUS) hosted by the Department of Circulation and Medical Imaging, NTNU.

The thesis has aimed to model ultrasonic wave propagation in coupled non-parallel plates, with through-tubing well logging as the guiding example. The work is a continuation of a specialization project written in the autumn of 2020, from which some parts are borrowed and adapted. The specialization project took a different approach than presented in this thesis to modeling already initialized leaky Lamb waves. A condensed version was submitted as a proceedings article to the 44^{th} Scandinavian Symposium on Physical Acoustics under the title *A fast semi-analytical method for propagating leaky Lamb wavefields* (Appendix B).

The work also led to some ideas that culminated in an extended abstract submitted to the same symposium titled *Understanding sound radiation from surface vibrations moving at subsonic speeds* (Appendix C). An extended journal article on the topic is planned.

On a personal level, working with this thesis has been a joy from start to finish. Some years ago, I concluded that I most enjoy topics I've always had a relation to but never grasped the theoretical depth of. The first time it was heat flow and spheres, and it is a good feeling to conclude my studies in Trondheim with another such combination: waves and plates. I was already, before embarking on this work, very interested in learning about guided elastic waves, and in many ways, I've come a bit further than I first anticipated. That is, however, not only to my credit.

I would especially like to thank my supervisor Erlend Magnus Viggen for his excellent guidance and for giving me every opportunity to succeed. Our weekly meetings have been appreciated and extremely useful, and the willingness to follow up on the work and be available has been inspiring. Thanks are also owed to Tonni Franke Johansen for co-suggesting the initial project, Tor Nordam for internally following up the project at the Department of Physics, and the professors of the acoustics group; Hefeng Dong for useful discussions and help finding an article, and Peter Svensson and Guillaume Dutilleux for having provided me with a fundamental understanding of acoustics over the past few years.

A huge thanks also go out to friends, family, and my girlfriend. Your support, but especially all the things *not* related to this thesis, have made the whole experience much better,

Håvard Kjellmo Arnestad

Trondheim June 24, 2021

Contents

Abstract i
Sammendrag iii
Preface v
List of figures vii
List of symbols x

1 Introduction **1**
1.1 Background and motivation 1
1.2 Ultrasonic well logging and previous work 4
1.3 Thesis aims and structure 5

2 Theory **7**
2.1 Some fundamentals of waves and propagation 7
2.1.1 Gaussian wave packets and dispersion 7
2.1.2 Different types of acoustic waves 8
2.2 Towards semi-guided waves in elastic media 10
2.2.1 Bulk waves in elastic media 11
2.2.2 Guided plane wave formulation 13
2.2.3 Matrix formulation of guided waves 15
2.3 Lamb waves I: Derivation and understanding 16
2.3.1 A quick primer: Surface waves 17
2.3.2 From boundary conditions to a characteristic equation 18
2.3.3 Symmetric solution 19
2.3.4 Antisymmetric solution 21
2.4 Lamb waves II: Methods for leaky waves 22
2.4.1 Generalized Lamb waves 22
2.4.2 Attenuation of Lamb waves in light fluids 23
2.4.3 Attenuation of Lamb waves in contact with light solids 25
2.4.4 Normal mode expansion 27
2.5 The angular spectrum method 30
2.5.1 Parallel plane propagation 30
2.5.2 A fast method for diffraction on tilted planes 31
2.6 Response methods: Reflection and transmission 33
2.6.1 A single plate 33
2.6.2 Two coupled plates 36
2.7 The inverse problem 38

2.7.1 What is non-linear inversion? . . . 38
2.7.2 Inversion strategies: Brute force and simulated annealing . . . 39

3 Setup, simulation methods, and implementation 41
3.1 System setup in simulations . . . 41
3.1.1 Materials and geometry . . . 41
3.1.2 Excitation source in simulations . . . 42
3.1.3 COMSOL simulation . . . 44
3.2 Modal method implementation . . . 45
3.2.1 Numerical solution of the Lamb dispersion relation . . . 45
3.2.2 Single plate excitation using NME . . . 48
3.3 Response method implementation . . . 49
3.4 Strategy for the inverse problem . . . 50
3.4.1 Choice of cost function . . . 50
3.4.2 Inversion method . . . 51

4 Results and discussion 53
4.1 Verification of the forward model . . . 54
4.1.1 Transmission through a plate in water . . . 54
4.1.2 Reflection from a plate on a cement half-space . . . 55
4.1.3 Reflection from coupled tilted plates . . . 56
4.2 Inversion of the two-dimensional problem . . . 59
4.2.1 Parameter sensitivity and limits to inversion . . . 59
4.2.2 The mechanism for cement detection with tilted plates . . . 63
4.2.3 Inversion results . . . 65
4.2.4 The case for and against practical inversion . . . 67
4.3 Additional topics . . . 69
4.3.1 Three-dimensional simulations . . . 69
4.3.2 Comments on execution time . . . 69

5 Conclusion 73
5.1 Extended summary . . . 73
5.2 Suggestions for further work . . . 74
5.3 List of achieved results . . . 75

Bibliography 77

A Code for simulating tilted plates in two dimensions 83

B SSPA article: Propagating leaky Lamb waves 90

C SSPA extended abstract: Subsonic radiation 113

List of Figures

1.1 Oil well with double casing. 2
1.2 Pitch-catch method. 3

2.1 Matrix formulation for three layers. 15
2.2 Schematic Lamb wave representation. 17
2.3 Phase speeds of Lamb waves. 17
2.4 Group speeds of Lamb waves. 18
2.5 Displacement field of the S_0 mode. 20
2.6 Displacement field of the A_0 mode. 21
2.7 Displacement field of the A_1 mode. 22
2.8 Power flow balance. 24
2.9 Attenuation curves for a plate in water. 25
2.10 Attenuation for a plate in contact with light cement and water. 26
2.11 Attenuation for a plate in contact with heavy cement and water. 27
2.12 Schematic of the angular spectrum approach. 31
2.13 Angular spectrum between tilted planes. 32
2.14 Reflection vs. incidence angle, some configurations at 250 kHz. 34
2.15 Reflection coefficients, steel plate in water. 35
2.16 Difference in reflection coefficients, from plate on water vs. cement. . . . 36
2.17 Multiple reflections in double plates. 36
2.18 Construction an inverse problem. 38

3.1 Single plate COMSOL model. 42
3.2 Two plates COMSOL model. 43
3.3 Mode excitation vs. incidence angle. 44
3.4 Maximum model deviance in excitation pressure. 46
3.5 Lamb mode tracing, ωd against β. 47
3.6 NME integration flowchart. 48
3.7 Response method flowchart. 49
3.8 Interpolation of response coefficients. 50

4.1 Excitation and transmission spectrum. 53
4.2 Transmission through plate in water: NME, response, and COMSOL. . 54
4.3 Waveforms, transmission through plate in water. 55
4.4 Reflection from plate on cement: NME, response, and COMSOL. 56
4.5 Waveforms, reflection from plate on cement. 57
4.6 Snapshots of wave propagation in coupled plates. 57

4.7 Reflected pressures, two plates tilted by 3°. 58
4.8 Reflected pressures, two plates tilted by 0° and −3°. 59
4.9 Waveforms, two plates and varying tilts. 60
4.10 Cost sensitivity to different parameters. 62
4.11 Sensitivity to water in different geometries, assuming cement. 63
4.12 Spectrum of transmission for two tilt angles. 64
4.13 Spectrum of detected differences for two tilt angles. 65
4.14 Brute force inversion, cement. 66
4.15 Cost generating envelopes. 67
4.16 Brute force inversion, water. 68
4.17 Snapshots of three-dimensional propagation between tilted plates. 70
4.18 Closer look at three-dimensional wavefields. 71

List of symbols

This list explains most of the used symbols. Some symbols are re-purposed, but the correct meaning should be possible to understand from the context.

Wave-related

c	Wave speed	c_{ph}	Phase speed
c_{gr}	Group speed	f	Frequency
ω	Angular frequency	k	Wavenumber
β	Horizontal wavenumber	γ	Vertical wavenumber
α	Attenuation	Z	Impedance
I	Intensity	P_x	Power flow
D	Downwards wave	U	Upwards wave
R	Reflection coefficient	T	Transmission coefficient
S	Angular spectrum propagator	$\measuredangle_\theta$	Tilting operation
K	Lamb wave scaling	r	Reflection component
ϕ	P-wave potential or incidence/radiation angle	ψ	S-wave potential

Other mechanical quantities

x, y, z	Cartesian directions	t	Time
ρ	Density	v	Velocity
u	Displacement	p or P	Pressure (time or frequency)
θ	Tilt angle	F	Force
σ	Stress or standard deviation	ϵ	Strain
λ, G	Lamé parameters	ν	Poisson's ratio
E	Young's modulus	s	Plate separation distance
d	Plate thickness	h	Plate half-thickness

Subscripts

p	P-wave	s	S-wave
S, A	Lamb wave symmetry	w	Water
c	Center or cement	f	Fluid
r	Reflected (pressure)	in	Incident (pressure)
m, n	Mode indices	i, j, k, l	Indices
L	Lost (power)	A, B	Plate label

Matrix formulation

$l1$	Layer 1, etc.	$i2$	Interface 2, etc.
$\boldsymbol{a}$	Potential amplitudes	$\boldsymbol{f}$	Field values
$\boldsymbol{T}$	Transport matrix	$\boldsymbol{M}$	Potential-to-field matrix
$\boldsymbol{D}$	Field matrix	$\boldsymbol{L}$	Layer matrix
$\boldsymbol{S}$	System matrix	$\boldsymbol{N}$	Compound matrix connecting waves (D and U) on both side of a layered structure

Miscellaneous symbols

$\mathrm{S}_{0,1,2...}$	Symmetric Lamb modes	$\mathrm{A}_{0,1,2...}$	Antisymmetric Lamb modes
$\boldsymbol{x}, \boldsymbol{X}$	Vector or matrix	x, X	Scalar
$\hat{\boldsymbol{x}}$	Unit vector	$\tilde{x}$	Complex conjugate
$\lvert x \rvert$	Absolute value	i	$\sqrt{-1}$
env{x}	Envelope	$\mathcal{F}$	Fourier transform
mrNSR	mean root Noise-to-Signal Ratio	$a_{n,m}$	Modal participation factor (in NME)

Chapter 1

Introduction

1.1 Background and motivation

Every oil well will one day, for whatever reason, need to be permanently plugged and abandoned (P&A). Some petroleum will always remain in the ground when wells are abandoned, and the plugs must be tight so that hydrocarbons cannot leak out from a poorly sealed well and harm the environment. The tubes of concrete and steel, stretching kilometers into the ground, cannot be removed entirely. Therefore, Norwegian legislation imposes strict demands on the oil companies to ensure that the wells are plugged safely [1], but the associated costs are high. SINTEF estimates that with today's technology, the cost of plugging every remaining well would reach several hundreds of billions of NOK [2], 78 percent of which falls on the Norwegian taxpayers. Better P&A technology that can reduce the overhanging cost of closing wells can potentially save both the state and a global industry massive resources to be allocated elsewhere.

A significant step forward in P&A technology can be made by improving the flexibility of cement evaluation techniques also to cover double casings, as exemplified in Fig. 1.1. An oil well runs from the ground surface down to a petroleum reservoir. The casings, which are large-diameter steel pipes, keep the hole from caving in, and cement is placed between the casing and the surrounding rock walls. The cement acts as a seal that ensures the only way for petroleum to flow is through the casing. A perfect cement seal is required before abandonment to keep hydrocarbons from migrating outside the plugged casings towards the surface. Poor cement quality is linked with several defects, e.g., microannuli[1], channeling[2], and cracks[3] that give fluids a path of migration.

In existing wells, cement bond logs may already be available. However, they can be decades old and performed during construction with only a single casing. New logs will therefore have to be made in many situations. Today the evaluation of cement quality can only be performed through one casing, and if two casings are present, the procedure gets very costly as casings must be pulled out of the borehole. A better option would be to leave the casings in place and perform the logging through the inner casing. Promising initial results have been published by Viggen et al. [3, 4], suggesting that the ultrasonic pitch-catch logging method in a single casing (illustrated in Fig. 1.2a, but explained

[1] A small gap between the casing and the surrounding cement sheath.
[2] The condition where cement flows in a channel only on some sides of the casing.
[3] As in everyday speech, a crack in the material where fluid can enter.

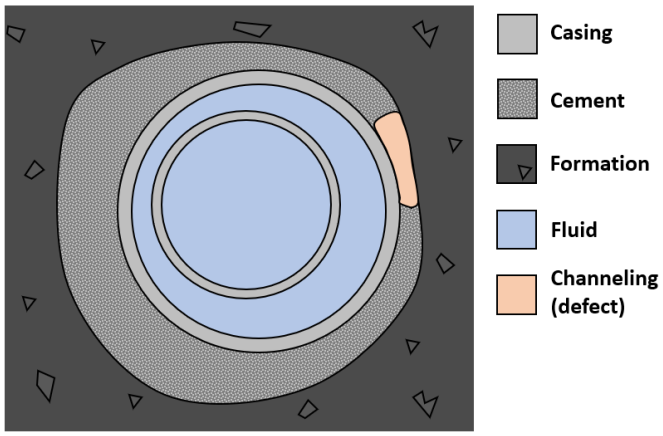

Fig. 1.1. Oil well with double casing. In through-tubing logging, measurements are performed from the inner casing (without removal), here with aim to detect the channeling outside the outer casing.

in greater detail in Sec. 1.2) can be extended to a double casing setup (illustrated in Fig. 1.2c).

Unfortunately, the step from single to double casing adds a great deal of complexity to the problem, and the quality of the cement cannot be inferred directly. An evaluation of the cement quality behind two casings will therefore rest on an inversion method. A key ingredient in inversion schemes is the *forward model*, essentially a computational model that bridges the parameters of interest (e.g., cement quality) to real measurement data from an actual well. The forward model is calculated many times with continuously updated parameters as its output converges towards the measurement; when the deviance between model and measurement is small, one assumes that the true state of the system measured has been captured. In principle, the forward model could be implemented in a finite element analysis software such as COMSOL Multiphysics, but a computation time of several hours for each iteration would be prohibitive for practical well logging. Therefore, it is necessary to develop an efficient forward model that captures all the relevant physics in the pitch-catch method, such as casing eccentricity.

A common simplifying assumption usually made about the casings is that they can be locally approximated to be plates [5, 6], which in general is valid when the wavelengths considered and wall thickness are much smaller than the casing diameter [7]. Wave propagation in plates, a form of guided wave referred to as *Lamb waves*, and in layered media in general, is well studied, with applications in, e.g., non-destructive testing (NDT), marine acoustics, and seismology. With the plate approximation, casing eccentricity translates into non-parallel plates. However, should the casings be concentric, they can still be non-parallel along a different axis if one casing is tilted.

This thesis aims at developing an efficient forward model for through-tubing well logging that captures all of the relevant physics when using the plate approximation for the casings. Previous results related to this thesis project [8], for a single plate, have already verified that a model based on Lamb wave theory in combination with an angular spectrum approach can be feasible.

The developed model will be relevant for many problems, as plates and plate-like

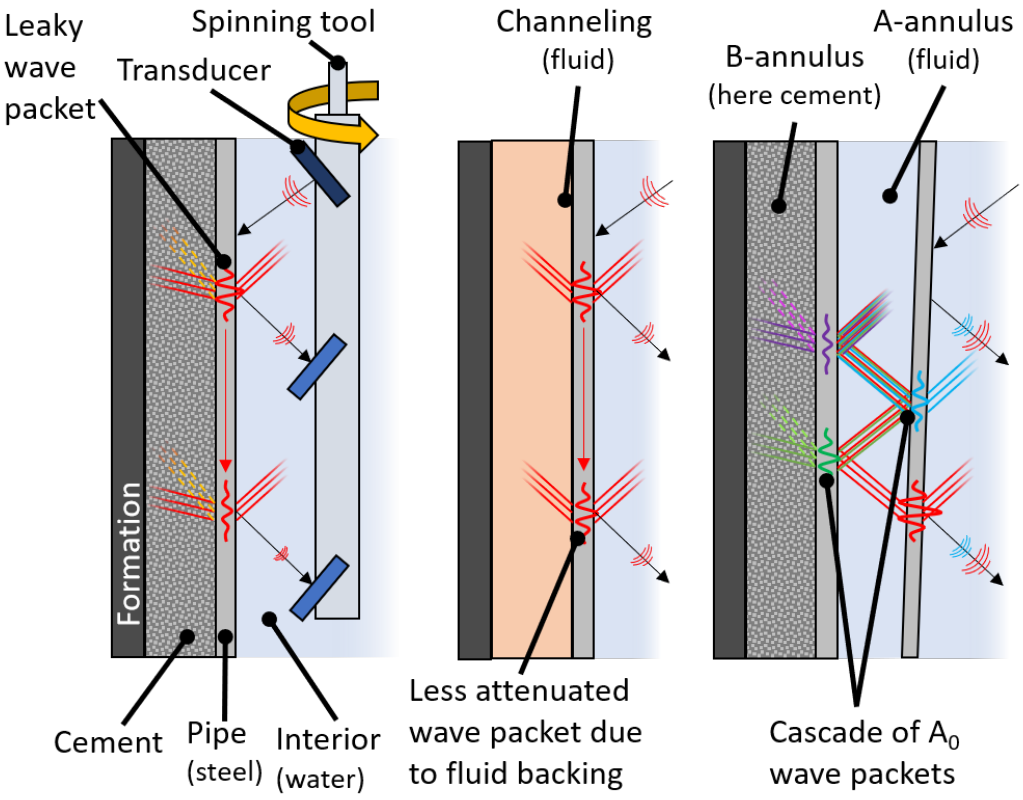

(a) Pitch-catch through a single casing. A leaky A_0 wave packet is shown at two different times, with reduced amplitude due to attenuation.

(b) If a defect such as channeling is present, the wave packet is less attenuated.

(c) The double casing situation, here as a snapshot in time. The leakage from the initial wave packet causes a cascade of wave packets to be set up due to the (nearly) parallel plates and equal casing thickness. The cement quality must be inferred from the later wave packets on the inner casing (e.g., ●).

Fig. 1.2. Different situations that illustrate the pitch-catch technique in the single and double casing setup. Cement quality is measured from the attenuation a wave packet undergoes as it propagates along with the casing. Attenuation is primarily due to the leakage from each packet, as is indicated by wavefronts; solid lines indicate longitudinal waves, and dashed lines indicate shear waves.

structures are found in many systems. Examples include the walls of a house, the hull of a ship, and the ice on a frozen lake. Another relevant example, which includes two plates, is for the potential ultrasonic inspection of components inside the main vessel in sodium-cooled nuclear reactors [9, 10], as an alternative to immersed ultrasonic transducers in liquid sodium.

1.2 Ultrasonic well logging and previous work

Different acoustic methods exist for evaluating oil wells [11]. The first is a sonic method [12] that measures the attenuation of a compressional wave, more specifically an S_0 Lamb wave [13], of about 20 kHz propagating in the casing along its axis. No azimuthal information is obtained, making it challenging to distinguish poor cement from other types of defects. Energy loss is mainly due to shear coupling, which can be an issue if there is no solid contact, e.g., due to "wet" microannuli [14].

Ultrasonic pulse-echo measurements were introduced in part to get azimuthal information. In the pulse-echo method, the tool carrying the sensors is pulled up the well along a helical path. The transducer repeatedly emits short pulses at normal incidence to the casing and measures the returning echo. The echo contains information about the decay of mode resonance which is related to the acoustic impedance of the material behind the casing. A higher measured impedance translates to a better coupling to cement or better cementing quality. The accuracy of the impedance measurements requires a difference in 1.0 MRayls between fluids and solids to separate one from the other [15].

The pulse-echo technique is limited in evaluating light-weight cement and foam cement with low acoustic impedance contrast to mud. That motivated the development of the pitch-catch technique [16], which is often used in conjunction with pulse-echo. It is based on exciting the flexural mode of the casing or, in other words, the A_0 Lamb mode. The method is shown in Fig. 1.2a. A pulse is emitted from a transducer at an angle that couples well to the casing. As the wave packet propagates along with the casing, it leaks energy both to the fluid towards receiving transducers and to the material on the other side of the casing. If the material is cement, the pulse is more heavily attenuated because of the lower contrast in impedance. Energy is radiated in outgoing P-waves and S-waves; however, the finer details depend on the casing and surrounding media. If the material behind the casing is poor cement, a fluid, or some other defect, the pulse is less attenuated, as shown in Fig. 1.2b, due to the weaker acoustic coupling to the plate. The pulse is measured at two or more receivers, and the attenuation is used to infer the material impedance behind the casing. The method may also probe deeper into the cement layer when the echo reflected at the interface between rock and cement, the third interface echo (TIE), is reliable. Rough and non-parallel interfaces are factors that contribute to reduced TIEs.

Recent studies have investigated the possibility of using pitch-catch for through-tubing logging with numerical simulations and various numbers of receivers [3, 4]. As depicted in Fig. 1.2c, the two plates may support a cascade of wave packets. If the two plates' dispersion characteristics are similar and relatively parallel, the packets will be well separable. The second packet on the inner casing (●) depends in part on a wave packet propagating on the outer casing (●), and carries information about the

cement quality. It was shown in [4] that with five receivers and a simple forward model, a limited inversion was possible. However, to perform a general inversion as will be needed in a practical setting, a complete forward model is needed that, quote *"can deal with factors such as differing dispersion relations on the casings, casing eccentricity, misaligned casings, and attenuating fluids"*.

In the literature, the theory of elastic waves in layered media is thoroughly described in, e.g., [17], or [18]. However, it is limited to parallel planes, meaning casing eccentricity cannot be readily included in the model. A proceedings article by Zeroug [19] very briefly describes a method to include eccentricity by combining reflection and transmission coefficients with a high frequency, approximate, "wavenumber-shifting scheme". Unfortunately, the shifting scheme is unpublished and only explained with a ray-based argument.

1.3 Thesis aims and structure

The primary aim of this project is to create a computationally efficient forward model for through-tubing well logging, simulating a situation as depicted in Fig. 1.2c, where the casings are approximated as plates. The relevant physics considered is

- how an incident wave couples to the plate,
- how waves or wave packets propagate in a plate,
- how the waves are attenuated when the plate is in contact with different materials,
- how the leaked wave propagates between the plates and to the receiver,
- how the plates can be simulated as non-parallel.

The developed method will, in general, apply to any system consisting of multiple plates and motivates the title *"A Fast Simulation Method for Ultrasonic Wave Propagation in Coupled Non-parallel Plates"*.

In order to test the model's validity, the simulations are compared to reference simulations in COMSOL Multiphysics. Also, because the model is developed to solve the inverse problem, simplified inversion will be attempted. It is also a goal to understand wave propagation and the possibilities of solving the inverse problem. Therefore, the theory of Lamb waves will be treated in detail.

The structure of the thesis is as follows. **Ch. 2** covers the theory required, including waves in elastic media, wave propagation in plates, the angular spectrum approach, and inversion. In **Ch. 3**, the practical implementation is discussed, including tuning of algorithms and choices in deciding parameters and system setups in the simulations. The results are shown and discussed in **Ch. 4**, with the two main topics being to validate the methods and performing inversion on a chosen example. In **Ch. 5** the thesis is concluded, and topics for further work are suggested.

Readers who are only interested in the developed simulation method for two non-parallel plates may focus on the following sections: 2.2.3, 2.5, 2.6, 3.1, 3.3, and 4.1.

Chapter 2

Theory

The theory can thematically be divided into three parts, where the first serves to give context for the rest of the chapter. **Sec. 2.1** takes up a common theme throughout this thesis, which is the synthesis of spatially localized waves from infinite plane wave solutions, and different wave types. **Sec. 2.2** develops the basic theory by briefly giving the necessary background for waves in solid media and then describes how matrix techniques can be employed for layered elastic media. The focus is particularly on three-layered media such as plates in contact with cement or water.

A significant portion of the theory is intended to give a good understanding of Lamb waves. In **Sec. 2.3** the modal theory of Lamb waves will be derived from the context of the matrix framework for a plate in vacuum. **Sec. 2.4** extends the practical applicability of Lamb waves, as perturbation methods can be used to include the plate interaction with surrounding media. That includes the attenuation of leaky Lamb waves, as well as a technique called normal mode expansion (NME) that is valuable for assessing both stationary and transient mode excitability. Because perturbation methods are not exact, proper generalized Lamb waves that deviate from the free plate solution are also discussed in this section.

The remaining sections cover different topics related to the forward and inverse problem of two coupled, non-parallel plates. In **Sec. 2.5** the angular spectrum approach is presented, which is a natural method to model the leaked wavefields. A method from optics, which seems not to have been applied in acoustics, is also presented that makes it computationally cheap to connect two non-parallel plates. In **Sec. 2.6** a complementary derivation from the matrix framework is shown, leading to response methods. Response methods provide little in terms of understanding but make it much easier to exactly model generalized Lamb waves. Finally **Sec. 2.7** discusses how to construct and solve the inverse problem.

2.1 Some fundamentals of waves and propagation

2.1.1 Gaussian wave packets and dispersion

A natural way of specifying a localized wave is by using a Gaussian wave packet. A benefit of the shape that the frequency spectrum is also Gaussian, where a sharply localized spatial wave packet must contain a broad band, i.e., a wide Gaussian, of

spatial frequencies, and vice-versa.

The Gaussian wave packet is a product of two parts: the Gaussian envelope, and the carrier wave. In one dimension, the envelope is given by a center location x_0 and spatial width given by the variance σ^2. The full width at half maximum (FWHM) is useful for describing the width, and the two are related as FWHM $\approx 2.355\sigma$ [20]. The complex carrier wave gives the wave-like structure and propagation direction, specified from the carrier wavenumber k_c at the center frequency of the wave packet. Their product is the Gaussian wave packet $g(x)$ at $t = 0$. Via the Fourier transform, it can be expressed in the wavenumber domain instead as $G(k)$

$$\begin{aligned} & g(x) = e^{-\frac{(x-x_0)^2}{2\sigma^2}} \cdot e^{-ik_c x} \\ \xrightarrow{\mathcal{F}} \quad & G(k) = \frac{\sigma}{\sqrt{2\pi}} e^{-\frac{\sigma^2(k+k_c)^2}{2}} \cdot e^{ix_0(k-k_c)}, \end{aligned} \tag{2.1}$$

The wave packet can be propagated with time t when the dispersion relation $\omega(k)$ is given. The relation connects the temporal angular frequency ω and the wavenumber. Each wavenumber component can be treated separately by adjusting the phase according to the dispersion relation and then reconstructing the wave packet again using the inverse Fourier transform

$$g(x,t) = \mathcal{F}^{-1}\{e^{i\omega(k)t} G(k)\}. \tag{2.2}$$

If the Gaussian wave packet is reasonably sharp in the frequency domain, an analytical solution for time propagation can be found [21]. Here only a few key features will be discussed relating to the Taylor expansion of the dispersion relation. Around the carrier wavenumber up to the second derivative, it reads

$$\omega(k) = \underbrace{\omega(k_c)}_{k_c c_{ph}} + (k-k_c) \underbrace{\frac{\partial \omega(k_c)}{\partial k}}_{c_{gr}} + \frac{1}{2}(k-k_c)^2 \underbrace{\frac{\partial^2 \omega(k_c)}{\partial k^2}}_{\Gamma} + \dots , \tag{2.3}$$

where the phase velocity c_{ph} and the group velocity c_{gr} are recognized. The phase velocity gives the propagation velocity of a monochromatic wave, whereas the group velocity gives the propagation velocity of a wave packet and also the energy propagation velocity unless the wave is attenuated somehow [22]. By substituting the Taylor expansion with three terms back into Eq. (2.2) and discarding the phase factor, one gets that the Gaussian envelope develops according to

$$\mathrm{env}\{g(x,t)\} = \exp\left[-\frac{1}{2}\left(\frac{x - x_0 - c_{gr}t)}{\sigma\sqrt{1 + \frac{\Gamma^2}{\sigma^4}t^2}} \right)^2 \right]. \tag{2.4}$$

It is clear that the Gaussian wave packet propagates at the group velocity. However, if the wave packet contains a range of group velocities, the packet will disperse with time, as captured by Γ.

2.1.2 Different types of acoustic waves

Fluid waves

Liquids and gases can only support one type of compressional wave that is non-dispersive. Covered in most textbooks on engineering or marine acoustics [18, 23].

Elastic waves

Elastic media, such as steel, can support two types of waves that travel at different speeds. One is a longitudinal P-wave, where "P" is for primary or pressure. The other is a slower transversal S-wave, where "S" stands for secondary or shear. The wave type is covered in some detail in Sec. 2.2.1.

Free waves

Free waves describe all waves that propagate without energy loss and include fluid and elastic waves that are not subject to attenuation. Classical Lamb waves, a type of guided wave covered in Sec. 2.3, are also free waves.

Attenuated waves

Waves that propagate with loss of energy and are dampened along their propagation direction. Heat conduction, viscoelasticity, and scattering are examples of underlying causes of attenuation. In this work, any attenuation is due to the wave being leaky, as covered more in Sec. 2.4.2.

Inhomogeneous waves

A wave that is exponentially increasing or decreasing along its wavefront. The situation can be realized when a wave propagates in viscous fluids or plates while radiating into a half-space of an ideal fluid. In the plate example, the waves will exponentially increase away from the plate because they were emitted from a position where the plate vibration was less attenuated.

The mathematical formulation includes a distinction between the real and imaginary wave vector. The two do not have to be parallel, and the imaginary component normal to the real wave vector is sometimes called the inhomogeneity vector [24].

The wave type is not widely known, and the term is sometimes also used to describe wave attenuation in general. The wave type is again referenced in Sec. 2.4.2, and one of the key components in the extended abstract submitted to the Proceedings of the 44th Scandinavian Symposium on Physical Acoustics [25], attached in Appendix C.

Evanescent waves

Waves that do not propagate but decays exponentially with distance. An example is a surface vibration on a plate in water. If the surface vibration is subsonic to the water, it does not radiate energy away. Instead, the water "sloshes" around (hydrodynamic short-circuit), and the wave vanishes exponentially away from the plate. Most relevant to angular spectrum wave propagation, in Sec. 2.5.

Guided waves

The term describes free waves that travel along with plates or multiple layers without radiating away energy. For Lamb waves, the plate is assumed to be non-viscous and in a vacuum, so all energy is guided between the two plate surfaces.

Leaky waves / semi-guided waves

If a plate supporting Lamb waves is immersed in a fluid, the wave may become leaky in the sense that energy is transported away by the fluid, and the Lamb wave attenuates with distance. The term semi-guided is also descriptive; the P- and S-waves bouncing between the plate boundaries are mostly reflected, but not entirely.

In practice, ultrasonic methods like pitch-catch rely on fluid or solid coupling and, therefore, on leaky waves. Proper classical Lamb modes, which by definition require a vacuum, can not be excited or detected acoustically. However, they are usually very reasonable as a first approximation when the surrounding medium is not a vacuum, as long as the density is relatively low compared to the plate.

Surface and interface waves

A solid half-space adjacent to a vacuum may support a surface wave, with the best-known example being Rayleigh waves, owing to Lord Rayleigh's prediction of the wave type in 1885. Because the wave is confined to roughly two wavelengths into the solid medium, it retains its amplitude over long propagation distances. That has a severe effect when earthquakes occur, as the surface waves generated usually cause the most material destruction. Surface waves are discussed in some more detail in Sec. 2.3.1.

If the vacuum is replaced with a material, the interface between can support a wave which can be considered a generalization of surface waves. The two examples usually given are Scholte waves for solid-fluid interfaces and Stoneley waves for solid-solid interfaces. This type of wave mode can also be seen when a plate is adjacent to a fluid or a solid half-space, then sometimes called, e.g., quasi-Scholte.

2.2 Towards semi-guided waves in elastic media

In many textbooks on acoustics, the attention is typically directed towards sound waves that propagate through air or water. While strings, membranes, plates, and bars in some cases are covered before the acoustic wave equation, the analysis is usually limited to situations of low frequencies where some of the complexities of elastic wave propagation are hidden [23, 26].

To more generally handle guided waves in elastic media, it is necessary to go back to the fundamentals for multiple reasons. Firstly, waves in bulk solid materials are more complicated; in the simplest case of an isotropic, homogeneous material, the material can support polarized shear waves in addition to longitudinal waves. Secondly, when these waves are guided, the boundary conditions are more complex and give rise to wave modes that are not intuitive, at least initially, such as the aforementioned surface waves.

When the elastic medium is bounded from two sides, as is the case for a plate in a vacuum, the elastic medium becomes a waveguide. The propagating modes that are supported are called Lamb waves after Horace Lamb, who analyzed the waves and published the equations in 1917 [27]. The modes come in two flavors, the symmetric modes S_0, S_1, S_2, etc., and the antisymmetric modes A_0, A_1, A_2, etc., where symmetric and antisymmetric refers to the symmetries of displacements around the midplane of the plate. The A_0 mode is often called the flexural mode, as it for low frequencies tends

toward the flexural waves derived for thin plates and bars. The mode is also the primary target for the pitch-catch method.

In most practical settings, the plate will not be situated in a vacuum but rather be in contact with water or even cement. It is possible to treat such cases generally, but the theory of ideal, classical Lamb waves provide the most intuitive framework for thinking about plate waves, and may often be very reasonable, such as for a steel plate in air or water. The most significant deviation from the vacuum case is that Lamb waves become attenuated. The secondary effect is when the dispersion relation and mode characteristics change, and in the situations where that becomes noticeable, the classical Lamb waves are no longer a good approximation, and more general approaches are required.

Numerous sources underpin this chapter in different ways. The book of Viktorov [28] is one of the first books on the topic of Lamb waves and still a referenced source in literature. Rose [29] includes or points to relevant new techniques since Viktorov, some from another important work by Auld [30, 31] that borrows a great deal from electromagnetism and is a bit more focused on piezoelectric materials. Hovem's book on marine acoustics [18] is also used, in particular for its coverage of many fundamental concepts in addition to elastic waves and multilayered media, the latter of which is an essential technique for generally analyzing ultrasonic waves through matrix techniques [17].

2.2.1 Bulk waves in elastic media

The Cauchy momentum equation describes the non-relativistic momentum transport in any continuum, much like Netwon's 2nd law:

$$\frac{\partial(\rho \boldsymbol{v})}{\partial t} + \nabla \cdot (\rho \boldsymbol{v} \otimes \boldsymbol{v}) = \nabla \cdot \boldsymbol{\sigma} + \boldsymbol{F}, \tag{2.5}$$

where $\otimes$ denotes the outer product, ρ is the density, $\boldsymbol{v}$ is the velocity, t is time, $\boldsymbol{\sigma}$ the second rank stress tensor, and $\boldsymbol{F}$ the force vector containing body forces such as gravitation. The left-hand side could also have been expressed using the material derivative, D/Dt. When considering a solid, the $\mathcal{O}(v^2)$ term can be neglected since the material moves around an equilibrium, and the velocity will generally be very small. To express the displacement $\boldsymbol{u}$, as common in solid mechanics, one can linearise the momentum derivative as $\partial(\rho \boldsymbol{v}/\partial t) \simeq \rho \partial^2 \boldsymbol{u}/\partial t^2$ to get

$$\rho \frac{\partial^2 \boldsymbol{u}}{\partial t^2} = \nabla \cdot \boldsymbol{\sigma} + \boldsymbol{F}. \tag{2.6}$$

We now want to insert the general stress-strain relationship through the constitutive relation, i.e., Hooke's law in three dimensions. The strain tensor is defined as

$$\epsilon_{ij} = \frac{1}{2}\left(\frac{\partial u_i}{\partial x_j} + \frac{\partial u_j}{\partial x_i}\right) = \frac{1}{2}(u_{i,j} + u_{j,i}), \tag{2.7}$$

where indicial notation is used, along with the Einstein summation convention where repeated indices imply summation. The most general linear relation among all the components of the stress and strain tensor is $\sigma_{ij} = C_{ijkl}\epsilon_{kl}$, where C_{ijkl} are the components of the fourth-order stiffness tensor with 81 components. Several symmetries

can be exploited, so for anisotropic materials, it reduces to 21 components, and by imposing rotational invariance as for isotropic media, it further reduces to the two Lamé parameters λ and G:

$$\sigma_{ij} = \lambda \delta_{ij} \epsilon_{kk} + 2G\epsilon_{ij}. \tag{2.8}$$

Here G, often named μ, is the shear modulus. The Lamé parameters can be expressed through more experimentally available material parameters such as

$$\lambda = \frac{\nu E}{(1+\nu)(1-2\nu)}, \tag{2.9a}$$

$$G = \frac{E}{2(1+\nu)}, \tag{2.9b}$$

where E is Young's modulus and ν Poisson's ratio. Via tensor algebra, it is possible to come to the following expression for the divergence of stress

$$\nabla \cdot \boldsymbol{\sigma} = (\lambda + G)\nabla(\nabla \cdot \boldsymbol{u}) + G\nabla^2 \boldsymbol{u}, \tag{2.10}$$

and inserted into Eq. (2.6) and one obtains the *Navier-Cauchy equation* for momentum conservation in an isotropic solid. Since the body force $\boldsymbol{F}$ is no longer interesting, it is not included, and the resulting equation is

$$\rho \frac{\partial^2 \boldsymbol{u}}{\partial t^2} = (\lambda + G)\nabla(\nabla \cdot \boldsymbol{u}) + G\nabla^2 \boldsymbol{u}. \tag{2.11}$$

This already implies a wave equation in the displacement. The next step is to invoke the Helmholtz decomposition theorem, where the displacement field $\boldsymbol{u}$ can be written as

$$\boldsymbol{u} = \nabla\phi + \nabla \times \boldsymbol{\Psi} = \boldsymbol{u_p} + \boldsymbol{u_s}, \tag{2.12}$$

and this decomposition has an essential property in that

$$\nabla \times \boldsymbol{u_p} = \nabla \times (\nabla\phi) = \boldsymbol{0}, \tag{2.13a}$$

$$\nabla \cdot \boldsymbol{u_s} = \nabla \cdot (\nabla \times \boldsymbol{\Psi}) = 0. \tag{2.13b}$$

Because $\boldsymbol{u_p}$ is curl-free, one has that $\nabla(\nabla \cdot \boldsymbol{u_p}) = \nabla^2 \boldsymbol{u_p}$, which can be used to split displacement into the two components $\boldsymbol{u_p}$ and $\boldsymbol{u_s}$ and thus write Eq. (2.11) as

$$\left[\frac{1}{c_p^2}\frac{\partial^2 \boldsymbol{u_p}}{\partial t^2} - \nabla^2 \boldsymbol{u_p}\right] + \left[\frac{1}{c_s^2}\frac{\partial^2 \boldsymbol{u_s}}{\partial t^2} - \nabla^2 \boldsymbol{u_s}\right] = \boldsymbol{0}. \tag{2.14}$$

The two bracketed terms should hold separately, and they do indeed turn out to be the wave equations for elastic isotropic media. They also hold for the corresponding potentials, so the substitutions $\boldsymbol{u_p} \to \phi$ and $\boldsymbol{u_s} \to \psi$ are valid. If the area where the solution is sought is infinite, these equations are sufficient for describing elastic wave propagation. c_p and c_s are the two wave velocities of the longitudinal P-wave and

transversal S-waves of two polarizations. Their velocities and ratios are given by

$$c_p = \sqrt{\frac{\lambda + 2G}{\rho}}, \tag{2.15a}$$

$$c_s = \sqrt{\frac{G}{\rho}}, \tag{2.15b}$$

$$\frac{c_s}{c_p} = \sqrt{\frac{1 - 2\nu}{2(1 - \nu)}}. \tag{2.15c}$$

From Eq. (2.15c), it is seen that shear waves cannot exist in materials with a Poisson's ratio of 0.5. An expression for the components of the intensity field $\boldsymbol{I}$ will be needed and can be calculated from

$$I_i = -\sigma_{ij} v_i. \tag{2.16}$$

In relation to intensity, the impedance is sometimes used, of which there are two in solids

$$Z_p = \rho c_p, \tag{2.17}$$

$$Z_s = \rho c_s. \tag{2.18}$$

2.2.2 Guided plane wave formulation

Plane waves present a tractable method for handling guided waves that, with relatively few assumptions, leads to a matrix formulation for the fields inside a plate or layer. It is customary to consider the two-dimensional case, and here the plane waves in question have a wave vector on the form $\boldsymbol{k} = k_x\hat{\boldsymbol{x}} + k_y\hat{\boldsymbol{y}} + 0\hat{\boldsymbol{z}}$. The coordinate system is aligned as in Fig. 2.1 so that the propagation is in the x-y plane, and the wave fields are invariant in the z-direction. That lets us write $\boldsymbol{u}$ from Eq. (2.12) as

$$\boldsymbol{u} = \underbrace{\left(\frac{\partial \phi}{\partial x} + \frac{\partial \Psi_z}{\partial y}\right)}_{u_x}\hat{\boldsymbol{x}} + \underbrace{\left(\frac{\partial \phi}{\partial y} - \frac{\partial \Psi_z}{\partial x}\right)}_{u_y}\hat{\boldsymbol{y}} + \underbrace{\left(\frac{\partial \Psi_y}{\partial x} - \frac{\partial \Psi_x}{\partial y}\right)}_{u_z(\text{discarded})}\hat{\boldsymbol{z}}. \tag{2.19}$$

Although the movement is invariant in the z-direction, it is clear that the displacement component u_z is non-zero and depends only on the potentials Ψ_x and Ψ_y that are associated with the horizontally polarised shear wave (SH). The other two components depend on potentials ϕ and $\Psi_z = \psi$, associated with longitudinal waves (P) and vertically polarised shear waves (SV). It is, therefore, possible to seek solutions separately for the P + SV wave combination [32]. In practice, the SH waves are often discarded; the inner casing in the pitch-catch method is filled with fluid, and the SH waves can neither be excited nor measured by fluid-immersed transducers.

In a solid layer, the fields of a right-going wave may thus be expressed as the superposition of four plane waves. These are the P- and SV-waves (from here on S for short), propagating in the upwards and downwards directions. For a given frequency, Snell's law requires that the wave vectors of all waves are oriented so that they all have the same component β along the waveguide propagation direction, and the consequence is

that any solution propagates with a given phase speed. Note that in this particular case $\beta = k_x$, but in three dimensions $\beta^2 = k_x^2 + k_z^2$. For plates with lossless boundaries, the concept of transverse resonance is implied; the mode solutions are traveling along the waveguide axis and are standing waves in the transverse direction. For a single layer, these four plane waves then read

$$\phi = \left[D_p e^{i\gamma_p y} + U_p e^{-i\gamma_p y}\right] e^{i(\omega t - \beta x)}, \tag{2.20a}$$

$$\psi = \left[D_s e^{i\gamma_s y} + U_s e^{-i\gamma_s y}\right] e^{i(\omega t - \beta x)}, \tag{2.20b}$$

where D_p and D_s are the amplitudes of downward-moving P- and S-waves respectively, and U_p and U_s travel upwards, as in Fig. 2.1. The horizontal wavenumbers β are the same for all the plane waves, as mentioned. Because of the different wave speeds, the wavenumbers of P- and S-waves differ: $k_p = \omega/c_p$ and $k_s = \omega/c_s$. The vertical wavenumbers k_y, are therefore also different for P- and S-waves, and are denoted by γ_p and γ_s respectively:

$$\gamma_s = \sqrt{k_s^2 - \beta^2}, \tag{2.21a}$$

$$\gamma_p = \sqrt{k_p^2 - \beta^2}. \tag{2.21b}$$

The real power of the formulation emerges when introducing the field variables as expressed via the four wave components. Naturally, when two layers are in contact, forming an interface, the boundary conditions need to be matched. For elastic waves, that means the continuity of particle displacement and normal and shear stress (σ_{yy} and σ_{xy}). By inserting the expressions for the components of particle displacement via potentials (2.19) into the equation for strain (2.7), and piping the result into the constitutive relation for stress (2.8) one obtains

$$\sigma_{xx} = \lambda\left(\frac{\partial^2\phi}{\partial x^2} + \frac{\partial^2\phi}{\partial y^2}\right) + 2G\left(\frac{\partial^2\phi}{\partial x^2} + \frac{\partial^2\psi}{\partial x\partial y}\right), \tag{2.22a}$$

$$\sigma_{xy} = G\left(2\frac{\partial^2\phi}{\partial x\partial y} - \frac{\partial^2\psi}{\partial x^2} + \frac{\partial^2\psi}{\partial y^2}\right), \tag{2.22b}$$

$$\sigma_{yy} = \lambda\left(\frac{\partial^2\phi}{\partial x^2} + \frac{\partial^2\phi}{\partial y^2}\right) + 2G\left(\frac{\partial^2\phi}{\partial y^2} - \frac{\partial^2\psi}{\partial x\partial y}\right). \tag{2.22c}$$

Any stress component with a z-index is zero, and although σ_{xx} is not an imposed boundary condition, it will be needed in a later section. The last step is to substitute the plane wave formulation of the potentials into the stress and displacement equations. A bit of rearrangement yields a matrix equation for the stress and displacement through the plane wave amplitudes in $y = 0$, which is an arbitrary origin

$$\underbrace{\begin{bmatrix}\sigma_{yy}\\ \sigma_{yx}\\ u_y\\ u_x\end{bmatrix}}_{\mathbf{f}(0)} = \underbrace{\begin{bmatrix} G(\beta^2-\gamma_s^2) & G(\beta^2-\gamma_s^2) & -2G\beta\gamma_s & 2G\beta\gamma_s \\ 2G\beta\gamma_p & -2G\beta\gamma_p & G(\beta^2-\gamma_s^2) & G(\beta^2-\gamma_s^2) \\ i\gamma_p & -i\gamma_p & i\beta & i\beta \\ -i\beta & -i\beta & i\gamma_s & -i\gamma_s \end{bmatrix}}_{\mathbf{M}} \underbrace{\begin{bmatrix}D_p\\ U_p\\ D_s\\ U_s\end{bmatrix}}_{\mathbf{a}(0)}. \tag{2.23}$$

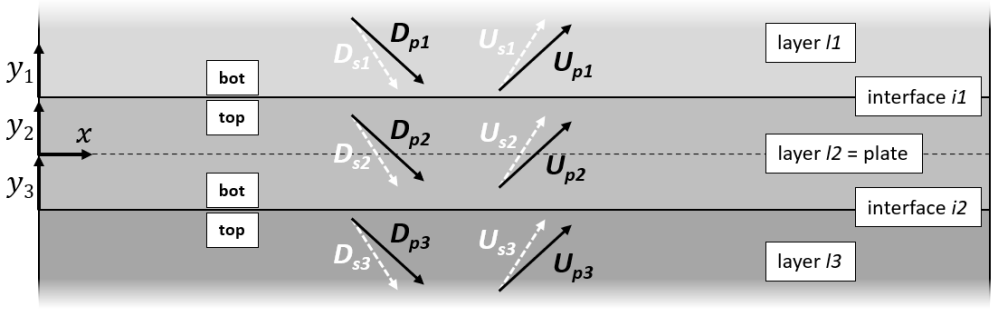

Fig. 2.1. Matrix formulation for one layer between two semi-infinite half-spaces. Layer $l2$ can be imagined to be a plate, and $l1$ and $l3$ two infinite half spaces. Each layer has its own y-axis, with the origins in the half-spaces coinciding with the interfaces.

The fields $\mathbf{f}$ anywhere else can be found by considering the phase information, as included in what Hovem [18] refers to as the transport matrix $\mathbf{T}$. It relates the waves to a different vertical position a distance y above the plane of origin

$$\mathbf{a}(y) = \underbrace{\begin{bmatrix} e^{i\gamma_p y} & 0 & 0 & 0 \\ 0 & e^{-i\gamma_p y} & 0 & 0 \\ 0 & 0 & e^{i\gamma_s y} & 0 \\ 0 & 0 & 0 & e^{-i\gamma_p y} \end{bmatrix}}_{\mathbf{T}(y)} \mathbf{a}(0), \tag{2.24}$$

such that the fields in any position y can be written as $\mathbf{f}(y) = \mathbf{M}\mathbf{T}(y)\mathbf{a}(0) = \mathbf{D}(y)\mathbf{a}(0)$, where $\mathbf{D}$ is the field matrix defined in Lowe's work [17].

2.2.3 Matrix formulation of guided waves

Using a matrix formulation gives a systematic way of working with guided waves in multilayered media. In this project, we deal with triple layers as illustrated in Fig. 2.1; a plate supporting Lamb waves, and two semi-infinite layers above and below the plate that might be vacuum or any other material. The only condition is that the boundary conditions at each interface must be satisfied. There are two main techniques available, and here the *transfer matrix method* will be discussed. The alternative is a *global matrix method* that is more numerically robust at higher frequency-thickness products but involves larger matrices as all wave components are solved simultaneously. According to Lowe, the transfer matrix method should be valid for A_0 modes up to roughly 15 MHz-mm using 128-bit precision for complex numbers, which is six times the center frequency-thickness used in pitch-catch logging, assuming a frequency of 0.25 MHz and a thickness of 10 mm.

The transfer matrix method works by relating the boundary conditions on one interface to the boundary conditions on another interface. The schematic is shown in Fig. 2.1. Assuming that displacements and stresses are known at interface $i1$ as $\mathbf{f}_{l2}(\text{top})$ the amplitudes of the waves can be found by inverting the field matrix

$$\mathbf{a}_{l2}(0) = \mathbf{D}_{l2}^{-1}(\text{top}) \cdot \mathbf{f}_{l2}(\text{top}). \tag{2.25}$$

The field variables at the bottom of the same layer can be found by using the field matrix again

$$\mathbf{f}_{l2}(\text{bot}) = \underbrace{\mathbf{D}_{l2}(\text{bot}) \cdot \mathbf{D}_{l2}^{-1}(\text{top})}_{\text{Layer matrix}=\mathbf{L}_{l2}} \cdot \mathbf{f}_{l2}(\text{top}). \tag{2.26}$$

The layer matrix is defined for convenience. The displacements and stresses must be continuous across the interfaces, e.g., $\mathbf{f}_{l2}(\text{bot}) = \mathbf{f}_{l3}(\text{top})$. This process can be continued layer for layer. If multiple layers are present one can define a system matrix $\mathbf{S} = \mathbf{L}_{l2} \cdot \mathbf{L}_{l3} ... \mathbf{L}_{l(n-1)}$, but for this example of a homogeneous plate $\mathbf{S} = \mathbf{L}_{l2}$. The waves in layer $l1$ and $l3$ can then be related. Remembering the different coordinate systems in each layer, one gets top = 0 in $l3$ and bot = 0 in $l1$, and the relation

$$\mathbf{a}_{l3}(0) = \mathbf{D}_{l3}^{-1}(0) \cdot \mathbf{S} \cdot \mathbf{D}_{l1}(0) \cdot \mathbf{a}_{l1}(0), \tag{2.27}$$

As stated by Lowe, two types of solutions can be found, both related to a group of ultrasonic inspection methods. The first goes under the name *response methods*, discussed in detail in Sec. 2.6, where reflection and transmission characteristics are examined. Typically one of the four incoming waves in $l1$ and $l3$ is given unit amplitude, and the remaining are set to be zero. Then the reflection and transmission coefficients are given by the amplitudes of the four outgoing waves.

The second category is *modal methods*, the main topic of Sec. 2.3 and 2.4, where propagation properties such as Lamb wave velocities are examined. The condition is that the wave should exist without forcing, and no energy comes into the system. This can be mathematically expressed via Eq. (2.27), with two entries on the left-hand side equal to zero, and two non-zero entries in $\boldsymbol{a}_{l1}(0)$. The determinant of the subsystem must be 0 to have a non-zero mode as a solution. This ensures that the matrix cannot be inverted due to a free row, and the additional degree of freedom gives an amplitude-independent relationship between the wave components.

The two approaches should be considered complementary. Modal methods provide the best intuition and clearest framework for thinking about plate waves and will be treated first. In the absence of an excitation source, it is also the only method that makes sense. On the other hand, response methods trade the intuition that makes the modal approach a great tool, for a more straightforward calculation of all the mode contributions, under the condition that the source is given.

2.3 Lamb waves I: Derivation and understanding

Lamb waves describe the most practically relevant modal solutions to guided wave propagation in a free plate. The shear-horizontal modes will not be discussed, as they do not couple into a fluid. Fig. 2.2 shows how Lamb waves come to be. An excitation creates P- and S-wave that bounce between the two boundaries to vacuum. After some distance, a steady pattern of up- and downwards-going waves emerge. As will be shown, this steady pattern can be decomposed into symmetric and antisymmetric contributions, where each constitutes a set of modes. The mode solutions are traveling along the waveguide axis and are standing waves in the transverse direction. Examples of phase velocities for a steel plate are shown in Fig. 2.3, and group velocities are shown in Fig. 2.4. The material parameters are given in table 3.1 on page 41.

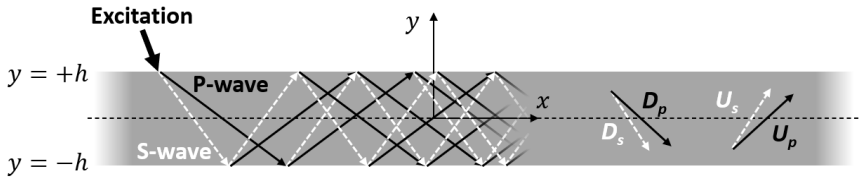

Fig. 2.2. Schematic representation of how Lamb waves, which is a certain combination of D_s, D_p, U_s and U_p, can exist as a coupling between P- and S-waves.

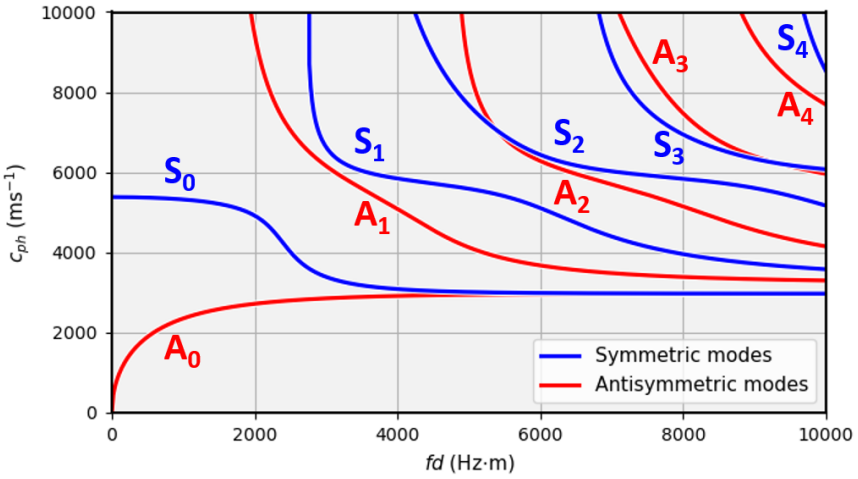

Fig. 2.3. Phase velocities for Lamb modes in a generic steel plate as a function of the frequency-thickness product fd.

2.3.1 A quick primer: Surface waves

Before taking on Lamb waves, it is good to understand the simpler example of surface waves that are self-sustaining and propagate along the surface of a solid medium. The technique of derivation is the same, covering roughly half of the problem. Also, surface waves are related to Lamb waves. At higher frequencies, the S_0 and A_0 Lamb waves tend toward being composed of two surface waves on each side of the plate.

Here a short derivation of Rayleigh waves will be given, existing on the interface between an elastic material and vacuum, and the propagation is non-dispersive with propagation velocity always less than the shear wave velocity, $c_R < c_s$. The particles follow an ellipse which amplitudes decrease with depth because Rayleigh waves do not penetrate the bulk.

One can find the characteristic equation for Rayleigh waves by using Eq. (2.23), where the coordinate system is placed on the surface. The two necessary conditions are that the surface stress $\sigma_{yy} = \sigma_{xy} = 0$, since a vacuum cannot resist motion. Also, since there are no incoming waves, it is sufficient to look at two downwards going waves D_p and D_s. That gives the matrix system

$$\begin{bmatrix} 0 \\ 0 \end{bmatrix} = \begin{bmatrix} G(\beta^2 - \gamma_s^2) & -2G\beta\gamma_s \\ 2G\beta\gamma_p & G(\beta^2 - \gamma_s^2) \end{bmatrix} \begin{bmatrix} D_p \\ D_s \end{bmatrix}. \tag{2.28}$$

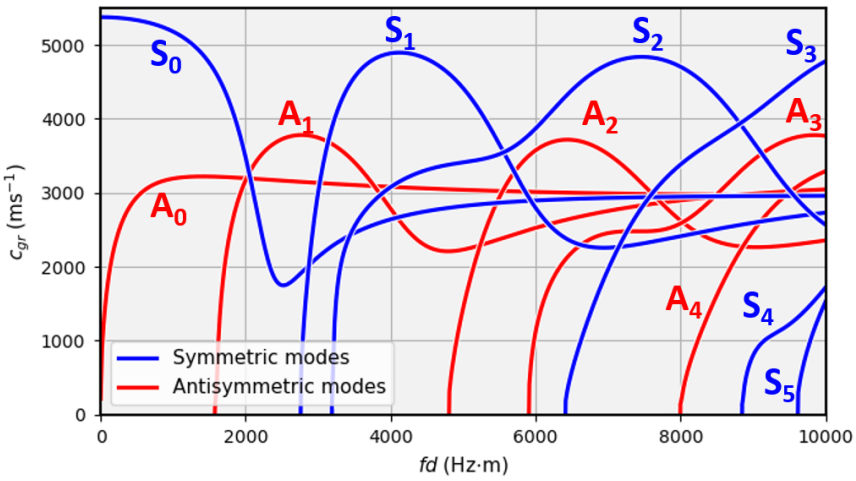

Fig. 2.4. Group velocities for Lamb modes in a generic steel plate as a function of the frequency-thickness product fd.

The determinant must be 0 to have a non-zero mode as a solution. That ensures the matrix cannot be inverted due to a free row, and the additional degree of freedom gives an amplitude-independent relationship between D_p and D_s. The characteristic equation that gives a determinant of 0 reads

$$(\beta^2 - \gamma_s^2)^2 + 4\beta^2\gamma_s\gamma_p = 0, \tag{2.29}$$

which is equivalent to the equation stated in [28]. It has three double roots but only one real solution that turns out to be independent of frequency, corresponding to the Rayleigh wave velocity. Eq. (2.30) is a universally accepted approximated solution for c_R obtained by best-fitting to a numerical solution of the characteristic equation [31]

$$c_R(\nu) = c_s\left(\frac{0.87 + 1.12\nu}{1+\nu}\right). \tag{2.30}$$

Rayleigh waves can, as stated in Sec. 2.1.2, be generalized into Scholte and Stoneley waves by replacing the vacuum with a fluid or solid material. Concerning modeling the pitch-catch setup, a useful fact is that interface waves on a steel plate in water cannot be excited by plane waves but requires a near-field source [18].

2.3.2 From boundary conditions to a characteristic equation

The plate considered is a single layer with thickness $d = 2h$, and boundaries to vacuum at $y = \pm h$. As with Rayleigh waves, the boundary conditions require that the relevant stresses are zero. Evaluated with respect to the mid-plane of the plate, the system matrix reads

$$\begin{bmatrix}\sigma_{yy}(+h)\\ \sigma_{xy}(+h)\\ \sigma_{yy}(-h)\\ \sigma_{xy}(-h)\end{bmatrix} = \begin{bmatrix}0\\0\\0\\0\end{bmatrix} = \begin{bmatrix} ae^{+i\gamma_p h} & ae^{-i\gamma_p h} & -be^{+i\gamma_s h} & be^{-i\gamma_s h}\\ ce^{+i\gamma_p h} & -ce^{-i\gamma_p h} & ae^{+i\gamma_s h} & ae^{-i\gamma_s h}\\ ae^{-i\gamma_p h} & ae^{+i\gamma_p h} & -be^{-i\gamma_s h} & be^{+i\gamma_s h}\\ ce^{-i\gamma_p h} & -ce^{+i\gamma_p h} & ae^{-i\gamma_s h} & ae^{+i\gamma_s h}\end{bmatrix}\begin{bmatrix}D_p\\U_p\\D_s\\U_s\end{bmatrix}, \tag{2.31}$$

where $a = G(\beta^2 - \gamma_s^2)$, $b = 2G\beta\gamma_s$, and $c = 2G\beta\gamma_p$ are introduced for compactness. With a priori knowledge about the solution, or close consideration, one can see that the first and second pair of columns make a good match. Instead of solving for the up- and down-going wave components, a solution to their combinations is sought

$$\begin{bmatrix} 0 \\ 0 \\ 0 \\ 0 \end{bmatrix} = \begin{bmatrix} +a\cos(\gamma_p h) & +ai\sin(\gamma_p h) & -ib\sin(\gamma_s h) & -b\cos(\gamma_s h) \\ +ci\sin(\gamma_p h) & +c\cos(\gamma_p h) & +a\cos(\gamma_s h) & +ai\sin(\gamma_s h) \\ +a\cos(\gamma_p h) & -ai\sin(\gamma_p h) & +ib\sin(\gamma_s h) & -b\cos(\gamma_s h) \\ -ci\sin(\gamma_p h) & +c\cos(\gamma_p h) & +a\cos(\gamma_s h) & -ai\sin(\gamma_s h) \end{bmatrix} \begin{bmatrix} D_p + U_p \\ D_p - U_p \\ D_s + U_s \\ D_s - U_s \end{bmatrix}. \quad (2.32)$$

Then the following substitutions are performed $D_p + U_p \to A_2$, $D_p - U_p \to A_1$, $D_s + U_s \to B_2$, and $D_s - U_s \to B_1$. The potentials in Eq. (2.20) can thus be rewritten as

$$\phi = [A_2\cos(\gamma_p y) + iA_1\sin(\gamma_p y)]e^{i(\omega t - \beta x)}, \quad (2.33a)$$

$$\psi = [B_2\cos(\gamma_s y) + iB_1\sin(\gamma_s y)]e^{i(\omega t - \beta x)}, \quad (2.33b)$$

The new equations show transverse resonance, and the substitutions will take on a more significant meaning soon, as they explain the symmetric and antisymmetric modes in the final solution. The final step is to simplify a bit further by row operations on row 1 and 3, and row 2 and 4:

$$\begin{bmatrix} 0 \\ 0 \\ 0 \\ 0 \end{bmatrix} = \begin{bmatrix} a\cos(\gamma_p h) & 0 & 0 & -b\cos(\gamma_s h) \\ ci\sin(\gamma_p h) & 0 & 0 & ai\sin(\gamma_s h) \\ 0 & -ai\sin(\gamma_p h) & +ib\sin(\gamma_s h) & 0 \\ 0 & c\cos(\gamma_p h) & a\cos(\gamma_s h) & 0 \end{bmatrix} \begin{bmatrix} A_2 \\ A_1 \\ B_2 \\ B_1 \end{bmatrix}. \quad (2.34)$$

The matrix must have a determinant of 0 to have a wave that can exist without forcing. Otherwise, it would be invertible, and a non-zero solution of the vector of unknowns could not exist. Writing out the determinant gives

$$\begin{aligned} &[a^2\cos(\gamma_p h)\sin(\gamma_s h) + bc\cos(\gamma_s h)\sin(\gamma_p h)] \\ \cdot&[a^2\cos(\gamma_s h)\sin(\gamma_p h) + bc\cos(\gamma_p h)\sin(\gamma_s h)] = 0. \end{aligned} \quad (2.35)$$

The determinant is also the product of two individual 2-by-2 determinants in the two upper and two bottom rows. Each can be equal to 0 on its own, as seen from the two square brackets. It will be shown that the two brackets are associated with the symmetric and antisymmetric modes.

After choosing the material parameters and thickness for the plate, the two remaining unknowns are frequency and wavenumber. The two can be matched to give the dispersion relation $\omega(\beta)$ by solving for the zeros of one of the two brackets, a method for which is presented in Sec. 3.2.1. The wavefields in the plate can be described entirely once the dispersion relation is known.

2.3.3 Symmetric solution

When the first part of the characteristic equation (2.35), which describes the symmetric components A_2 and B_1, is set to zero, the dispersion relation for symmetric Lamb waves is implicit in

$$\frac{\tan(\gamma_s h)}{\tan(\gamma_p h)} + \frac{4\beta^2\gamma_s\gamma_p}{(\beta^2 - \gamma_s^2)^2} = 0. \quad (2.36)$$

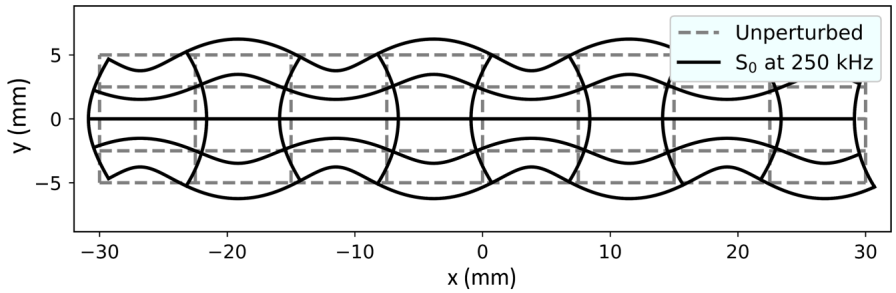

Fig. 2.5. Displacement field of the S_0 mode at 250 kHz in a 1 cm thick steel plate.

To obtain the dispersion relation in practice, the roots of Eq. (2.36) have to be found numerically.

When the dispersion relation holds, the corresponding 2-by-2 submatrix in Eq. (2.34) has a determinant of 0, and therefore also a free row. That makes it possible to express the ratio of A_2 and B_1 as

$$R_{\mathrm{S}} = \frac{B_1}{A_2} = \frac{(\beta^2 - \gamma_s^2)\cos(\gamma_p h)}{2\beta\gamma_s \cos(\gamma_s h)}. \tag{2.37}$$

The potentials ϕ and ψ are then known, except for an arbitrary scaling that K will represent. Substitution back into the relationships (2.12) and (2.22) give the full field equations for symmetric Lamb waves

$$\phi^S = K\cos(\gamma_p y) \tag{2.38a}$$
$$\psi^S = iKR_{\mathrm{S}}\sin(\gamma_s y) \tag{2.38b}$$
$$v_x^S = i\omega K[\beta\cos(\gamma_p y) - \gamma_s R_{\mathrm{S}}\cos(\gamma_s y)] \tag{2.38c}$$
$$v_y^S = \omega K[\gamma_p\sin(\gamma_p y) + \beta R_{\mathrm{S}}\sin(\gamma_s y)] \tag{2.38d}$$
$$\sigma_{xx}^S = iKG[(2\gamma_p^2 - \beta^2 - \gamma_s^2)\cos(\gamma_p y) + 2\gamma_s\beta R_{\mathrm{S}}\cos(\gamma_s y)] \tag{2.38e}$$
$$\sigma_{xy}^S = -KG[2\beta\gamma_p\sin(\gamma_p y) + (\beta^2 - \gamma_s^2)R_{\mathrm{S}}\sin(\gamma_s y)] \tag{2.38f}$$
$$\sigma_{yy}^S = iKG[(\beta^2 - \gamma_s^2)\cos(\gamma_p y) - 2\gamma_s\beta R_{\mathrm{S}}\cos(\gamma_s y)] \tag{2.38g}$$

Note that the displacements have been converted to velocities by multiplication with $i\omega$. The common phasor $e^{i(\omega t - \beta x)}$ is also omitted from all quantities.

The notion of symmetric waves comes from the field equations. The x-velocities v_x are symmetric around the mid-plane of the plate if described by cosines as seen in Eq. (2.38c), whereas the y-velocity v_y, is symmetric if described by sines as seen in Eq. (2.38d). For antisymmetric modes, the sines and cosines are swapped. The displacement field of an S_0 symmetric Lamb wave at 250 kHz in a 1 cm thick steel plate is shown in Fig. 2.5. Note that the S_1 wave does not exist at this frequency, as it is below its cut-off frequency. The cut-off frequencies for symmetric modes can be calculated by setting $\beta = 0$ in the characteristic equation

$$fd = \frac{Nc_p}{2} \quad (N = 1, 3, 5, \ldots), \tag{2.39a}$$
$$\text{or} \quad fd = Nc_s \quad (N = 0, 1, 2, \ldots)\,. \tag{2.39b}$$

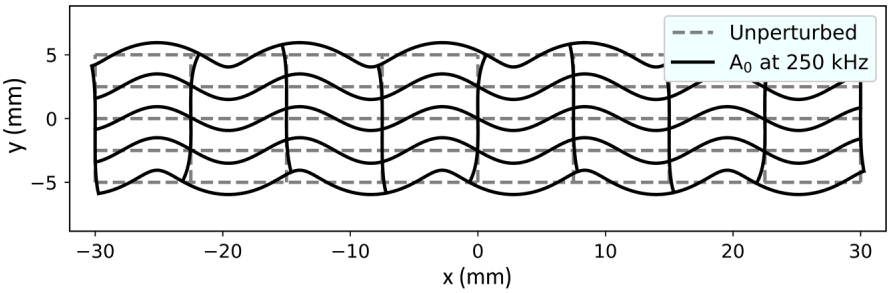

Fig. 2.6. Displacement field of the A_0 mode at 250 kHz in a 1 cm thick steel plate.

2.3.4 Antisymmetric solution

The second part of the characteristic equation (2.35) describes the antisymmetric modes, and the dispersion relation is implicit in

$$\frac{\tan(\gamma_p h)}{\tan(\gamma_s h)} + \frac{4\beta^2\gamma_s\gamma_p}{(\beta^2-\gamma_s^2)^2} = 0. \tag{2.40}$$

The same steps as for the symmetric solution are followed. When the dispersion relation holds, the corresponding 2-by-2 submatrix in Eq. (2.34) has a free row since the determinant is 0. That makes it possible to express the ratio of A_1 and B_2 as

$$R_{\mathrm{A}} = \frac{B_2}{A_1} = \frac{(\beta^2-\gamma_s^2)\sin(\gamma_p h)}{2\beta\gamma_s \sin(\gamma_s h)}. \tag{2.41a}$$

With the potentials known, again except for an arbitrary scaling K, substitution back into the relationships (2.12) and (2.22) gives the field equations for antisymmetric Lamb waves:

$$\phi^A = iK\sin(\gamma_p y) \tag{2.42a}$$
$$\psi^A = KR_{\mathrm{A}}\cos(\gamma_s y) \tag{2.42b}$$
$$v_x^A = i\omega K[\beta\sin(\gamma_p y) - \gamma_s R_{\mathrm{A}}\sin(\gamma_s y)] \tag{2.42c}$$
$$v_y^A = -\omega K[\gamma_p\cos(\gamma_p y) + \beta R_{\mathrm{A}}\cos(\gamma_s y)] \tag{2.42d}$$
$$\sigma_{xx}^A = iKG[(2\gamma_p^2 - \beta^2 - \gamma_s^2)\sin(\gamma_p y) + 2R_{\mathrm{A}}\beta\gamma_s\sin(\gamma_s y)] \tag{2.42e}$$
$$\sigma_{xy}^A = KG[2\beta\gamma_p\cos(\gamma_p y) + R_{\mathrm{A}}(\beta^2-\gamma_s^2)\cos(\gamma_s y)] \tag{2.42f}$$
$$\sigma_{yy}^A = iKG[(\beta^2-\gamma_s^2)\sin(\gamma_p y) - 2R_{\mathrm{A}}\beta\gamma_s\sin(\gamma_s y)] \tag{2.42g}$$

Examples of the displacement fields of the A_0 and A_1 modes at 250 kHz are given in Fig. 2.6 and 2.7. The cut-off frequencies are given by

$$fd = \frac{Nc_s}{2} \quad (N = 1, 3, 5, \ldots), \tag{2.43a}$$
$$\text{or} \quad fd = Nc_p \quad (N = 0, 1, 2, \ldots)\,. \tag{2.43b}$$

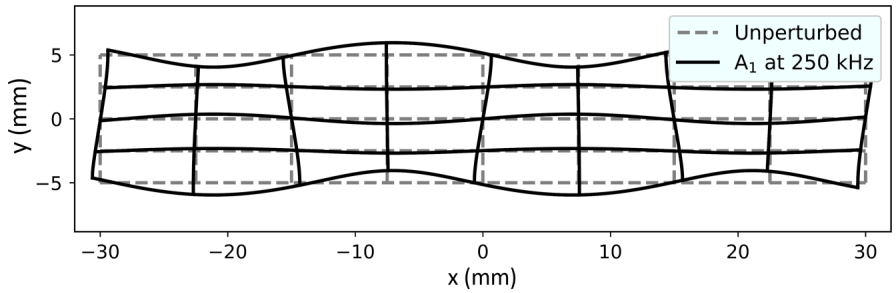

Fig. 2.7. Displacement field of the A_1 mode at 250 kHz in a 1 cm thick steel plate.

2.4 Lamb waves II: Methods for leaky waves

2.4.1 Generalized Lamb waves

The structure of free Lamb waves in the above derivation is the classical case and only truly realized for a plate with vacuum on both sides. A discussion about generalized Lamb waves can be found in the literature [31, 33], where the plate can be in contact with, e.g., a lighter solid on one side and fluid on the other. The generalized case differs from the free plate derivation by including outgoing waves in the adjacent media, and the first-order effect is that Lamb waves become "leaky" because energy is radiated away and the wave attenuated. Secondary effects include different phase speeds and the breakdown of proper symmetric and antisymmetric solutions.

The dispersion relation for generalized Lamb waves can be calculated via the matrix formulation. The condition is that there must be no incoming waves in the top layer ($D_{p1} = D_{s1} = 0$), and that below the plate we must demand the same ($U_{p3} = U_{s3} = 0$). This can be realised with Eq. (2.27). If we say that $\mathbf{N} = \mathbf{D}_{l3}^{-1}(\text{top}) \cdot \mathbf{S} \cdot \mathbf{D}_{l1}(\text{bot})$, then the determinant of the relevant sub-matrix must equal zero in both its real and imaginary part. It is worth thinking about it as a complex function $f(\mathbf{X})$, where the argument $\mathbf{X}$ is a vector of parameters, containing a complex wavenumber, frequency, plate thickness, and material parameters:

$$f(\mathbf{X}) = \begin{vmatrix} N_{22} & N_{24} \\ N_{42} & N_{44} \end{vmatrix} = 0. \tag{2.44}$$

An attempt to write out a characteristic equation will not be made here because the generality makes the matrix entries complicated and lengthy [33]. Also, the classification of modes becomes difficult. An exception from literature is for a plate submerged in a fluid that is equal on both sides of the plate, for which it can be shown, as first demonstrated by Schoch in 1952 [34, 35], that the characteristic equation for symmetric modes is

$$\frac{\tan(\gamma_s h)}{\tan(\gamma_p h)} + \frac{4\beta^2 \gamma_s \gamma_p}{(\beta^2 - \gamma_s^2)^2} = i \frac{\rho_f k_s^4 \gamma_p}{\rho \sqrt{k_f^2 - \beta^2} (\beta^2 - \gamma_s^2)^2} \cdot \tan(\gamma_s h), \tag{2.45}$$

where ρ is the density of the plate, ρ_f the fluid density, k_s the shear wavenumber, and k_f the fluid wavenumber. For antisymmetric modes it is

$$\frac{\tan(\gamma_p h)}{\tan(\gamma_s h)} + \frac{4\beta^2 \gamma_s \gamma_p}{(\beta^2 - \gamma_s^2)^2} = -i \frac{\rho_f k_s^4 \gamma_p}{\rho \sqrt{k_f^2 - \beta^2} (\beta^2 - \gamma_s^2)^2} \cdot \frac{1}{\tan(\gamma_s h)}. \tag{2.46}$$

As with Eq. (2.44), finding the solution requires searching for complex roots, which is considerably more challenging to do than in the free plate case. In this particular case, the fluid loading leads to additional modes that are not present in the free plate [36, 37], such as the quasi-Scholte modes that are interface waves. The quasi-Scholte modes cause a splitting of the A_0 mode, and the physics shows interesting anomalies depending on which materials are in contact [38, 39, 40].

The modified Newton's secant method can be used to find the complex roots of a function and was a part of the strategy of Dayal and Kinra to solve the dispersion relation of anisotropic plates [41]. The method is available in Python as `scipy.optimize.newton`. While the roots are complex, and additional modes are present, it seems possible to obtain the curves with a simplified scheme: The root-finding can be performed multiple times using the dispersion relation of a free plate mode as an initial guess. To ensure convergence, the density of the fluids or solids adjacent to the plate is gradually increased with each search. The search is applied to the A_0 and S_0 modes, solving Eq. (2.45) and (2.46), and are shown in Fig. 2.9. However, Lowe [17] discusses a more tried and tested searching method for the general case.

2.4.2 Attenuation of Lamb waves in light fluids

As discussed, the Lamb wave derivation presented assumes a free plate, and the interaction with a surrounding fluid would need to be included already in the boundary conditions in Eq. (2.31). However, in situations where the plate is much denser than the surrounding fluid, as with a steel plate in water, the Lamb wave structure can be assumed to be unperturbed except for adding an imaginary attenuation term to the wavenumber. In this section, we will see how to calculate attenuation in such cases.

When waves are attenuated, here in the x-direction, it is common to include the attenuation as an imaginary part of the wavenumber

$$k_x = \mathrm{Re}(k_x) + i\,\mathrm{Im}(k_x) = \beta - i\alpha, \tag{2.47}$$

where α is another often-used symbol for attenuation. For a wave of amplitude A, this translates to a wave that decays exponentially as

$$Ae^{i(\omega t - kx)} = Ae^{-\alpha x} \cdot e^{i(\omega t - \beta x)}, \tag{2.48}$$

with α often measured in neper per meter (Np/m), or in decibel $8.686 \cdot \alpha$ (dB/m). The propagation direction may not be parallel to the attenuation direction, in which case the wave is inhomogeneous [24].

Several perturbation techniques can be used to calculate approximate attenuation curves. Merkulov [35] used Schoch's characteristic equations to come to an approximation of the attenuation by doing a first-order perturbation and assuming the density of the fluid to be small. Auld presents another perturbation method [31], starting from a complex reciprocity relation. The same numerical attenuation values are obtained with both methods through different equations. Here we will look at a more intuitive method presented in 1982 by Watkins et al. [42] that leads to the same equations as Auld's method.

The main assumption is that the wave retains the same structure as in the free plate, although power is lost. Consider a differential element of the plate of unit depth,

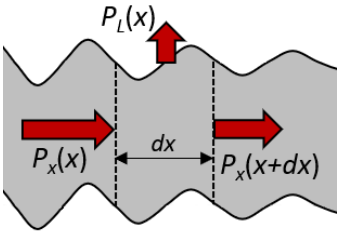

Fig. 2.8. Balance of energy flow into a small element of a plate.

as illustrated in Fig. 2.8. In the steady-state, a time-averaged power $P_x(x)$ is incident from the left, and a power $P_x(x+dx)$ leaves from the right. On the top of the plate, a total time-averaged power $P_L(x) = I_L(x) \cdot dx$ is lost to the medium through radiation. Note that I_L is the y-component of the intensity vector. Conservation of energy requires that

$$P_x(x+dx) - P_x(x) = -I_L(x) \cdot dx \quad \longrightarrow \quad \frac{dP_x(x)}{dx} = -I_L(x). \tag{2.49}$$

The time-averaged power flow along the plate can be calculated, with tilde denoting the complex conjugate, as

$$P_x = -\frac{1}{2}\int_{-h}^{h} (v_x \tilde{\sigma}_{xx} + v_y \tilde{\sigma}_{xy}) dy, \tag{2.50}$$

The next step is to calculate the radiated intensity I_L. Here the plate is in contact with only a fluid, so it is enough to consider that the normal velocity is continuous on the interface and related to the pressure through Euler's equation (see Eq. (2.78) on page 31). The radiated intensity on one side of the plate is [43]

$$I_L = \frac{Z_f |v_y(h)|^2}{2\sqrt{1 - \left(\frac{c_f}{c_{ph}}\right)^2}}, \tag{2.51}$$

where $|v_y(h)|$ is the amplitude of the normal velocity at the surface of the plate in contact with the fluid. c_f is the speed of sound in the fluid, and $Z_f = \rho_f c_f$ is the specific acoustic impedance, for water $Z_f = 1.48\,\text{MRayl}$.

The intensity and power flow both scales with the square of the amplitude. Hence, $I_L \propto P_x$, and the power flow and radiated intensity exponentially damped as

$$P_x(x) = P_x(0) e^{-2\alpha x}. \tag{2.52}$$

That can be inserted into Eq. (2.49), which can then be re-expressed as

$$\alpha = \frac{I_L}{2P_x} = \frac{\text{Power lost per metre into medium}}{2 \times \text{Power flow along the plate}}. \tag{2.53}$$

By knowing the dispersion relation of free Lamb waves, Eq. (2.50) can be integrated numerically with arbitrary scaling K, and Eq. (2.51) can be evaluated with the value of K. The result for a steel plate in water is shown in Fig. 2.9. The curves are identical to Merkulov's first-order approximation, but the power flow method benefits by being

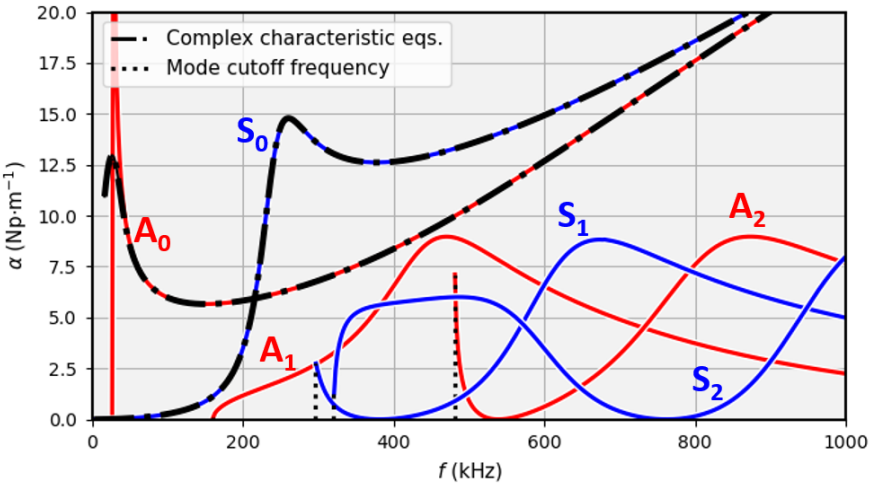

Fig. 2.9. Perturbation approximation of attenuation for Lamb waves in a 1 cm thick steel plate in contact with water on both sides. Only the first three S- and A-modes are shown. The cutoff frequencies ($\beta = 0$) are indicated. The solutions to Eq. (2.45) and (2.46) for the A_0 and S_0 are also given for comparison. The material parameters are given in table 3.1 on page 41.

easier to understand and more flexible; it can approximate radiation into solids as will be shown, and preliminary findings [25] suggest that using inhomogeneous waves can partially correct for the singularity at coincidence (the spike in the A_0 mode), and the absence of subsonic radiation. The singularity happens where the real wavenumber also changes appreciably [25]. Note that the attenuation curves also deviate from the perturbation solution at higher frequencies if the plate is in contact with water on only one side [37, 44], or if the fluids have different impedances.

2.4.3 Attenuation of Lamb waves in contact with light solids

The power flow method can also be used to get a first approximation to the attenuation of Lamb modes when the plate is in contact with solid media, but the cross-coupling of the imposed surface velocities $v_x(h)$ and $v_y(h)$ of the plate with the outgoing P- and S-waves requires some analysis to get right.

The boundary conditions require the surface velocity of the plate to be matched by the outgoing waves. From Eq. (2.23), one can get expressions for the amplitude potentials from the surface

$$\begin{bmatrix} U_p \\ U_s \end{bmatrix} = \frac{1}{\omega(\beta^2 + \gamma_s\gamma_p)} \begin{bmatrix} \gamma_s & \beta \\ -\beta & \gamma_p \end{bmatrix} \begin{bmatrix} v_y(h) \\ v_x(h) \end{bmatrix}. \tag{2.54}$$

From Eq. (2.12) and (2.20), it is quite straightforward to get expressions for the velocity amplitude of the outgoing waves

$$|v_p| = \omega k_p |U_p| \tag{2.55a}$$
$$|v_s| = \omega k_s |U_s|, \tag{2.55b}$$

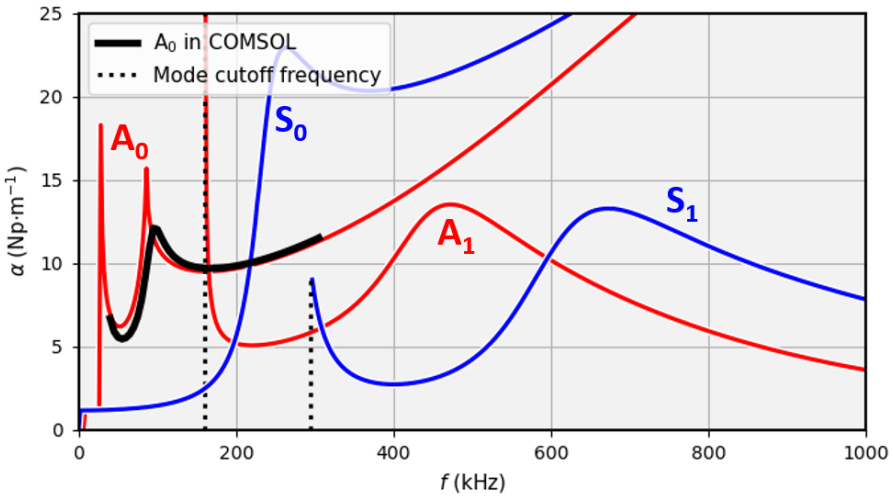

Fig. 2.10. Attenuation curves for Lamb waves in a 1 cm thick steel plate in contact with water and light cement, calculated with the power-flow method. Only the first two S- and A-modes are shown.

and by substituting in values for the potential amplitudes U_p and U_s, one gets

$$|v_p| = k_p \frac{|\gamma_s v_y(h) + \beta v_x(h)|}{|\beta^2 + \gamma_p \gamma_s|}, \tag{2.56a}$$

$$|v_s| = k_s \frac{|\gamma_p v_x(h) - \beta v_y(h)|}{|\beta^2 + \gamma_p \gamma_s|}. \tag{2.56b}$$

The power lost per metre into the medium, I_L is $I_{L,p} + I_{L,s}$. Only the intensity vector pointing away from the plate contributes. The radiation angle from the plate normal of each wave is given by the wavenumbers, so that $\cos\phi_{p,s} = \gamma_{p,s}/k_{p,s} = \sqrt{1 - \frac{\beta^2}{k_{p,s}^2}}$. Therefore

$$I_L = Z_p \frac{|v_p|^2}{2} \sqrt{1 - \frac{\beta^2}{k_p^2}} + Z_s \frac{|v_s|^2}{2} \sqrt{1 - \frac{\beta^2}{k_s^2}}, \tag{2.57}$$

and Eq. (2.53) can be used again be used to calculate α. Examples of attenuation for a plate in contact with water on one side, and one of two types of cement is shown in Fig. 2.10 and 2.11. The material parameters are given in table 3.1 on page 41, but the main difference is that the P-wave velocity in heavy cement is always supersonic for the A_0 wave mode. A comparison with COMSOL is also shown for a narrow frequency range, where the A_0 fields have been imposed on one end of the plate, and an exponential best-fit adapted to the enveloped profile of $v_y(x, y = h)$, where possible, to extract α. Neither the COMSOL measurements nor the perturbation method is exact, but their agreement strongly indicates that the correct physics is captured. Separate simulations not shown here have confirmed that the agreement improves further when the cement and water density decrease.

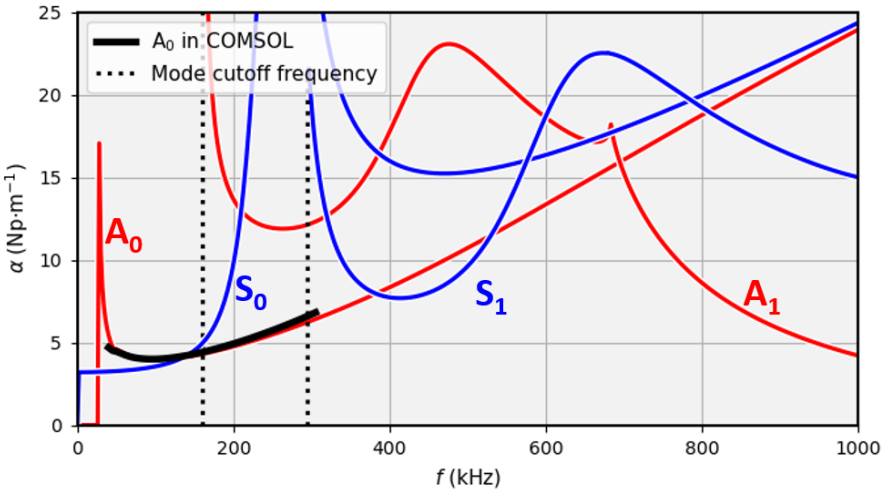

Fig. 2.11. Attenuation curves for Lamb waves in a 1 cm thick steel plate in contact with water and heavy cement, calculated with the power-flow method. Only the first two S- and A-modes are shown.

2.4.4 Normal mode expansion

Normal mode expansion (NME) is a method to evaluate waveguide excitation and works by expressing the total field as a superposition of all propagating modes supported by the structure. The contribution of each mode to the total is determined from the associated power flow using an orthogonality condition of the modes. NME is also a very useful tool because it leads to the interpretable concepts of *mode excitabily*, i.e., how easily a mode is excited by shear or normal forces at a particular frequency, and *source influence*, i.e., how the source geometry affect the excitation, as discussed in more detail in the book by Rose [29]. For waveguide excitation, it is not the only method, as an integral transform technique [28, 45, 46] can be used as well, which is more general but provides less in terms of intuition. Comparing the two methods is out of scope for this work, so only NME is discussed from here on.

For NME, it is assumed, and may recently have been proved [47], that the set of modes is complete, meaning that any thinkable excitation can be written as a weighted sum of normal modes. In addition, it has to be shown that the modes are, in fact, orthogonal, in the same sense that sines of different frequencies are orthogonal in Fourier analysis. Auld [31] proved the orthogonality of guided modes in lossless waveguides through a complex reciprocity relation for piezoelectric media. A real reciprocity relation also exists, more suitable for scattering problems. The two are derived from transmission line equations, but we will simply use it as a starting point and follow the derivation of [48] with some extensions from [29] and [49]. Because piezoelectric effects are ignored here, the modified Auld's complex reciprocity relation reads

$$\nabla(\tilde{\mathbf{v}}^{(2)} \cdot \boldsymbol{\sigma}^{(1)} + \mathbf{v}^{(1)} \cdot \tilde{\boldsymbol{\sigma}}^{(2)}) = -(\tilde{\mathbf{v}}^{(2)} \cdot \mathbf{F}^{(1)} + \mathbf{v}^{(1)} \cdot \tilde{\mathbf{F}}^{(2)}). \tag{2.58}$$

As the name implies, the complex reciprocity relation establishes a relation between two acoustic states, numbered by superscripts (1) and (2), that could occur in the same

spatial domain. $\mathbf{v}$ is a velocity field, $\boldsymbol{\sigma}$ a stress field, and $\mathbf{F}$ represents force. The sources, the medium parameters, and the wave fields may differ in each of the states. Because Lamb waves are z-invariant when the propagation is along the x-axis, writing out the tensor products give the reciprocity relation on the form

$$\begin{aligned}&\frac{\partial}{\partial x}\big(\tilde{v}_x^{(2)}\sigma_{xx}^{(1)}+\tilde{v}_y^{(2)}\sigma_{xy}^{(1)}+v_x^{(1)}\tilde{\sigma}_{xx}^{(2)}+v_y^{(1)}\tilde{\sigma}_{xy}^{(2)}\big)\\+&\frac{\partial}{\partial y}\big(\tilde{v}_x^{(2)}\sigma_{xy}^{(1)}+\tilde{v}_y^{(1)}\sigma_{yy}^{(1)}+v_x^{(1)}\tilde{\sigma}_{xy}^{(2)}+v_y^{(1)}\tilde{\sigma}_{yy}^{(2)}\big)\\=&-\tilde{v}_x^{(2)}F_x^{(1)}-\tilde{v}_y^{(2)}F_y^{(1)}-v_x^{(1)}\tilde{F}_x^{(2)}-v_y^{(1)}\tilde{F}_y^{(2)}.\end{aligned}\tag{2.59}$$

We now consider that the two solutions can represent either two different modes, or the same mode. Solution (1) gets its mode index denoted with m, and (2) by n on the form

$$\mathbf{v}^{(1)}(x,y,z,t)=\big(v_x^{(m)}(y)\hat{\mathbf{x}}+v_y^{(m)}(y)\hat{\mathbf{y}}\big)e^{i(\omega t-\beta_m x)}\tag{2.60a}$$

$$\tilde{\mathbf{v}}^{(2)}(x,y,z,t)=\big(\tilde{v}_x^{(n)}(y)\hat{\mathbf{x}}+\tilde{v}_y^{(n)}(y)\hat{\mathbf{y}}\big)e^{-i(\omega t-\tilde{\beta}_n x)}\tag{2.60b}$$

and similarly for the stress tensors components that are not shown here. Substitution into the reciprocity relation with $F_x=F_y=0$ and integrating over plate thickness yields

$$\begin{aligned}-i(\beta_m-\tilde{\beta}_n)\int_{-h}^{+h}&\big(\tilde{v}_x^{(n)}\sigma_{xx}^{(m)}+\tilde{v}_y^{(n)}\sigma_{xy}^{(m)}+v_x^{(m)}\tilde{\sigma}_{xx}^{(n)}+v_y^{(m)}\tilde{\sigma}_{xy}^{(n)}\big)dy\\&=-\big(\tilde{v}_x^{(n)}\sigma_{xy}^{(m)}+\tilde{v}_y^{(n)}\sigma_{yy}^{(m)}+v_x^{(m)}\tilde{\sigma}_{xy}^{(n)}+v_y^{(m)}\tilde{\sigma}_{yy}^{(n)}\big)|_{-h}^{+h}\end{aligned}\tag{2.61}$$

Now we assume traction-free boundary conditions, $\sigma_{yy}=\sigma_{xy}=0$, at the top and bottom of the plate. That is indeed true for classical Lamb waves, but not when the plate is in contact with a fluid, which is why NME is considered a perturbation method. Hence, $\tilde{\beta}_m=\beta_m$ because it is real, which is also a requirement [31]. One then gets

$$i(\beta_n-\beta_m)4P_{mn}=0,\tag{2.62}$$

where P_{mn} equals the power flow P_x in Eq. (2.50) if $m=n$, and 0 otherwise

$$P_{mn}=-\frac{1}{4}\int_{-h}^{+h}\big(\tilde{v}_x^{(n)}\sigma_{xx}^{(m)}+\tilde{v}_y^{(n)}\sigma_{xy}^{(m)}+v_x^{(m)}\tilde{\sigma}_{xx}^{(n)}+v_y^{(m)}\tilde{\sigma}_{xy}^{(n)}\big)dy=\begin{cases}0, & \text{if } m\neq n\\ P_x, & \text{if } m=n\end{cases}.\tag{2.63}$$

Equation (2.62) is a statement of orthogonality, limited to real wavenumbers (although sometimes used as a first approximation to lossy waves). If the wavenumbers are equal and the mode amplitude is non-zero, then there must be a power flow. If the wavenumbers do not match, the power flow is 0. In other words, the velocity field of, e.g., the A_0 mode, cannot transport power together with the stress field of the A_1 mode, or vice versa.

In the next step, we give new meanings to solutions (1) and (2). Solution (1) represents the source excitation, while solution (2) represents a single normal mode. Due to the completeness and orthogonality of the normal modes, the excitation source can be expressed as a normal mode summation

$$\mathbf{v}^{(1)}=\sum_m a_m(x)\mathbf{v}^{(m)}(y),\tag{2.64}$$

where $a_m(x)$ is a modal participation factor for mode number m, giving a position-dependent mode amplitude. The normal mode n is written as

$$\mathbf{v}^{(2)} = \mathbf{v}^{(n)}(y)e^{-i\beta_n x}. \tag{2.65}$$

Substitution into the complex reciprocity relation and integration over the plate thickness, again in the absence of a volume force $\mathbf{F}$, yields

$$\frac{\partial}{\partial x}e^{i\beta_n x}\sum_m 4a_m(x)P_{mn} = \left(\tilde{\mathbf{v}}^{(n)} \cdot \boldsymbol{\sigma}^{(m)} + \mathbf{v}^{(m)} \cdot \tilde{\boldsymbol{\sigma}}^{(n)}\right) \cdot \hat{\mathbf{y}}|_{-h}^{+h} e^{i\beta_n x}. \tag{2.66}$$

The modes are orthogonal, meaning the summation will be non-zero only when $m = n$. Also, because of the free Lamb wave assumption, only the excitation stress $\sigma^{(m)}$ is non-zero. For excitation from a fluid, the shear stress is zero, and the pressure acts against the surface normal, so normal stress is given by $\sigma_{yy}(h) = -p$. Algebraic manipulation gives

$$4P_{nn}\left(\frac{\partial}{\partial x} + i\beta_n\right)a_n(x) = -\tilde{v}_y^{(n)}(h)p, \tag{2.67}$$

which is an ODE on the form $y' + k \cdot y = p(x)$ that must be solved for $a_n(x)$, and the method of integrating factors can be used. To describing transient loading, the angular frequency ω of the loading is also included

$$a_n(\omega, x) = \left[\frac{-\tilde{v}_y^{(n)}(h)}{4P_{nn}}\int_0^x e^{i\beta_n x'}p(\omega, x')dx'\right]e^{-i\beta_n x}. \tag{2.68}$$

Intuitively it can be understood as a cumulative excitation of mode n, for example, the A_0 mode, on the plate by a time-harmonic pressure distribution. The sign of β determines which direction the wave travels. For transient loading, any quantity such as v_y can thus be expressed as a sum over all relevant modes n

$$v_y(t, x, y) = \sum_n \int a_n(\omega, x)v_y^{(n)}(y)e^{i\omega t}d\omega. \tag{2.69}$$

The above derivation misses one crucial point: the excitation force from the pressure acting on the plate depends not only upon the incident wave but also on the reflected one. Jia [49] gave an insightful derivation of how to include the reflected wave. As can be expected for a perturbation method, the total effective pressure will be twice the incoming, as if the plate is a fixed boundary, but the derivation also clearly demonstrates how attenuation should be included as an imaginary part of the wavenumber. A quick summary of the main points follows, using quantities more consistent with this thesis. First, the particle velocity must be continuous across the interface between the fluid and the plate

$$(-v_{in} + v_r)\cos(\phi) = a_n v_y^{(n)}(h), \tag{2.70}$$

where v_{in} is the particle velocity due to the incident wavefield, and v_r the reflected, while ϕ is the incidence angle. The same must be demanded for normal stress $\sigma_{yy} = -p(x)$

$$p = Z_f(v_{in} + v_r), \tag{2.71}$$

recalling that impedance have different signs for different propagation directions, and Z_f being the specific acoustic impedance of the fluid. Now we can try to express the total pressure p from the incoming pressure $p_{in} = Z_f v_{in}$. From Eq. (2.70) one can see that $v_r = \frac{a_n v_y^{(n)}(h)}{\cos(\phi)} + v_{in}$, so substitution into Eq. (2.71) gives

$$p = 2 \cdot p_{in} + \frac{Z_f a_n v_y^{(n)}(h)}{\cos(\phi)}, \tag{2.72}$$

which is equal to twice the incoming pressure (from fixed boundary condition) plus radiation from propagating wavemodes (only one mode is excited under Jia's assumptions). To see the effect on the solution, it can be substituted in on the right-hand side of Eq. (2.67). Simplifying the expression according to the power-flow methodology gives a correction to Eq. (2.67):

$$4P_{nn}\left(\frac{\partial}{\partial x} + i(\beta_n - i\alpha_n)\right)a_n x = -2p_{in}\tilde{v}_y^{(n)}(h), \tag{2.73}$$

where α_n is the attenuation of mode n, given by the same expression as the pertubation method derived by Auld [31], and essentially in Sec. 2.4.2. This goes to to show NME can be used for calculating transient loading for leaky Lamb waves, but also that it not exact, in part limited by the perturbation method assumptions.

2.5 The angular spectrum method

2.5.1 Parallel plane propagation

The angular spectrum is a superposition method for modeling the propagation of a wave field when the solution is supplied on the plane $y = y'$ [43, 50]. It is based on the fact that $e^{i(\omega t - \boldsymbol{k}\cdot\boldsymbol{r})}$ is a solution of the Helmholtz equation

$$\nabla^2 p + k^2 p = 0, \tag{2.74}$$

when the wave vector components satisfy

$$k^2 = k_x^2 + k_y^2 + k_z^2 = \beta^2 + k_y^2 = \frac{\omega^2}{c_f^2}. \tag{2.75}$$

Recall that the wavenumber associated with a wave vector along an arbitrary propagation direction in the waveguide is given by $\beta^2 = k_x^2 + k_z^2$. Since k is constant for each frequency, the three wavenumbers are not independent. Choosing k_y as dependent, one has that $k_y = \pm\sqrt{k^2 - k_x^2 - k_z^2}$, where the appropriate root must be chosen. When a vibrating steel plate is in contact with air, the wavefield in the x-z plane is given because it is imposed by the velocity field of the steel plate. The traces of the wavefronts in the air must match the wavefronts on the steel. The component k_y can thus be real or imaginary as a consequence. The latter implies a non-propagating evanescent wave into the air, as the phase velocity in the plate is subsonic for the surrounding air, giving a hydrodynamic short-circuit.

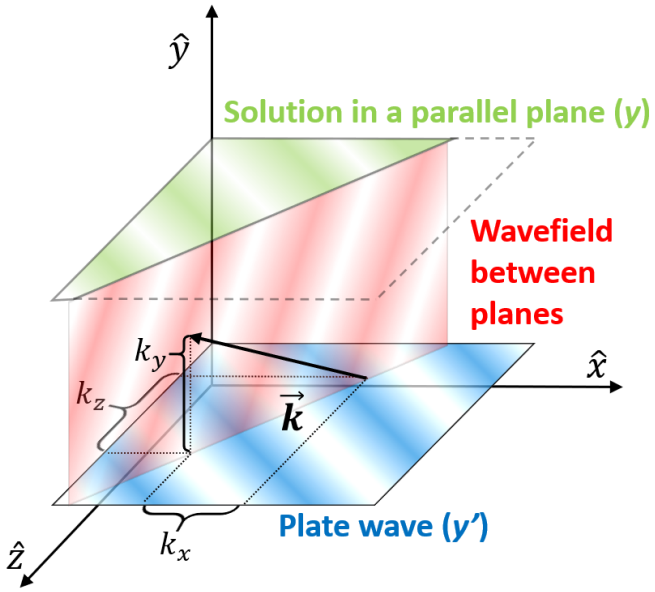

Fig. 2.12. Propagation of a monochromatic wavefield from a plate (●) into a parallel plane (●). The colored gradients represents wavefronts. The wave vector components k_x and k_z are imposed by the plate at $y = y'$. The wavefield between the planes, here shown as a cross section (●), can be calculated as different solution planes.

The basic idea is to decompose a complex wavefield p on a plane $y = y'$ into a sum of plane waves through the Fourier transform

$$P(\omega, k_x, k_z) = \mathcal{F}_t \mathcal{F}_x \mathcal{F}_z \{p(t, x, y = y', z)\}, \tag{2.76}$$

where $P(\omega, k_x, k_z)$ is often called the angular spectrum of plane waves. Since k_y is given for free by knowing k_x and k_z, one can propagate the wavefield between parallel planes as shown in Fig. 2.12, simply by adjusting the phase of each component. The general expression is

$$p(x, y, z, t) = \mathcal{F}_t^{-1} \mathcal{F}_x^{-1} \mathcal{F}_z^{-1} \{P(\omega, k_x, k_z) \cdot \underbrace{e^{ik_y(y'-y)}}_{\substack{\text{Propagator to} \\ \text{parallel planes}}} \}. \tag{2.77}$$

Depending on the method, such as NME, one might not have access to the fluid pressure directly. Euler's equation in the frequency domain can then be used to relate the normal velocity $\boldsymbol{V}$ in one plane to the pressure

$$i\omega\rho \boldsymbol{V} = -\nabla P. \tag{2.78}$$

2.5.2 A fast method for diffraction on tilted planes

The angular spectrum method can be adapted to calculate diffraction onto tilted planes, which was described by Matsushima et al. [51] for optical diffraction. The method has,

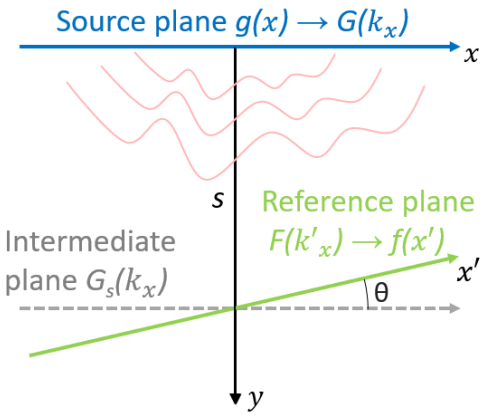

Fig. 2.13. Depiction of how a wavefield (●) is propagated a over a separation distance s from a source plane (●) to a reference plane (●) with tilt θ. A conversion to the wavenumber domain with a consecutive tilting of an intermediate plane is needed.

to our knowledge, never been applied in the field of acoustics, but it is suitable for calculating multiple reflections between tilted plates.

The tilt can be arbitrarily defined along two axes. For practical inversion in well logging, that may be necessary for most general situations because casing eccentricity gives a tilt along a different axis than non-parallel casings will. However, the casings are usually nearly parallel, and the eccentricity is more important to model. Therefore, in this section, we will focus on single-axis rotation, which also avoids non-commuting rotation matrices and keeps the equations shorter.

Two coordinate systems are used, shown in Fig. 2.13. The source plane (●) carries a complex wave $g(x)$, and a distance s away the reference plane (●) captures the propagated wavefield as $f(x')$. The method works in two main steps; first, the pressure from the source field $G(k_x)$ is propagated to an intermediate plane parallel to the source plane, giving $G_s(k_x)$. That can be performed using conventional techniques such as the standard angular spectrum method. Next, the plane waves are reassembled in the tilted reference system with a shared origin, giving $F(k'_x)$, and combined using the inverse Fourier transform. The essential part is to perform a coordinate rotation in the Fourier domain, followed by an interpolation that conserves energy.

To understand the coordinate rotation, it helps to think of wave vectors in the two coordinate systems are fundamentally the same object, but related by a coordinate rotation, here around the z-axis (as opposed to the y-axis in Matsushima's work):

$$\boldsymbol{k} = \begin{bmatrix} \cos\theta & -\sin\theta & 0 \\ \sin\theta & \cos\theta & 0 \\ 0 & 0 & 1 \end{bmatrix} \cdot \boldsymbol{k'}. \tag{2.79}$$

By interpolating $G_s(k_x)$, one can find the equivalent wave vector components in the tilted reference system, using uniformly spaced samples in k'_x

$$F(k'_x) = G_s(k'_x \cos\theta - k'_y \sin\theta). \tag{2.80}$$

The rotational transformation introduces a non-linearity, so the total energy in the field

is not conserved without including the Jacobian

$$J(k'_x) = \cos\theta + \frac{k'_x}{k'_y}\sin\theta. \tag{2.81}$$

The wavefield on the tilted reference plane can thus be written as

$$\mathcal{F}_{x'}\{f(x')\} = G_s(k'_x\cos\theta - k'_y\sin\theta)\cdot\left|\cos\theta + \frac{k'_x}{k'_y}\sin\theta\right|. \tag{2.82}$$

2.6 Response methods: Reflection and transmission

2.6.1 A single plate

Lamb waves, or the modal solutions of wave propagation in plates, were derived under the condition that the waves must exist without forcing. The other alternative approach is called response methods, where reflected or transmitted wavefields are calculated as a response to plane wave excitation. The reflection and transmission coefficients include contributions from all modes. While the method is powerful, it is difficult to understand the results without thinking about the modal solutions.

In this work, the reflection and transmission coefficients are needed for a plate in contact with cement and water, but no attempts will be made to write out expressions analytically because the equations get lengthy. In the introductory courses in acoustics, one learns to derive reflection coefficients for a liquid interface [23]. If the bottom half-space is elastic, one gets from textbooks on elastic wave propagation [18] a more complicated expression. From specialized literature [52] one can find elaborate expressions for the reflection coefficients for a plate in fluid, where the insights have been used to analyze the influence of fluid density on the leaky modes [53].

Response coefficients can also be derived from Eq. (2.27), and solved numerically with more generality. Since the excitation is from a fluid, the incoming P-wave amplitude on the top of the plate is set to unity, $D_{p1} = 1$, while the remaining incoming waves (evaluated at the top and bottom interfaces) are set to zero, $D_{s1} = U_{p3} = U_{s3} = 0$. In the implementation, a fluid like water is achieved by setting c_s very close to zero. The reflection coefficient for P-waves is defined as $R_p = U_{p1}/D_{p1}$, for S-waves $R_s = U_{s1}/D_{p1}$, and similarly the transmission coefficient for P-waves is $T_p = D_{p3}/D_{p1}$, and for S-waves $T_s = D_{p3}/D_{p1}$. Again, defining $\mathbf{N} = \mathbf{D}_{l3}^{-1}(\text{top})\cdot\mathbf{S}\cdot\mathbf{D}_{l1}(\text{bot})$, one can after some matrix algebra get

$$\begin{bmatrix} T_p \\ T_s \\ R_p \\ R_s \end{bmatrix} = \begin{bmatrix} 1 & 0 & -N_{12} & -N_{14} \\ 0 & 0 & -N_{22} & -N_{24} \\ 0 & 1 & -N_{32} & -N_{34} \\ 0 & 0 & -N_{42} & -N_{44} \end{bmatrix}^{-1} \begin{bmatrix} N_{11} \\ N_{21} \\ N_{31} \\ N_{41} \end{bmatrix}. \tag{2.83}$$

The matrix entries have to be calculated as a function of β and ω, and the obtained coefficients are complex-valued. Taking the example of a 1 cm thick steel plate, with water above the plate, and different materials below (see Fig. 2.1), solving for the reflection coefficients R_p at 250 kHz give curves as shown in Fig. 2.14. The curve labeled with "steel" is frequency independent and corresponds to a water-steel interface, and is for clarity therefore *not* a plate. However, with other materials, the reflection coefficient

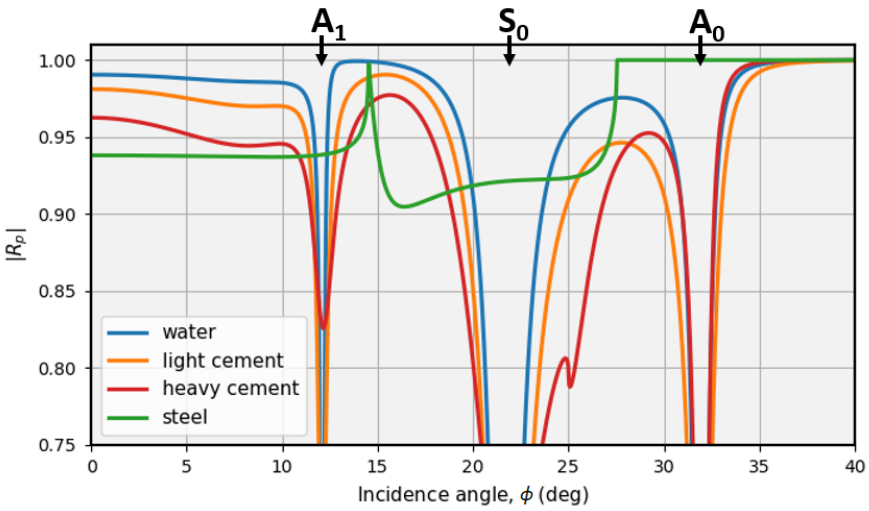

Fig. 2.14. Reflection coefficient at 250 kHz for an incoming plane wave in water above a 1 cm thick steel plate with different materials below. The steel-labeled curve corresponds to a half-space of steel. The optimal angles for exciting different Lamb modes are marked.

is frequency-dependent because the steel plate of finite thickness introduces a sense of spatial scale to the problem.

The reflection coefficient for a plate in water, R_w, is plotted for all β and ω combinations in Fig. 2.15. One can see that the reflection is greatly reduced where a Lamb mode is expected (see Fig. 3.5). This observation is explained in [52] and [53], where the characteristic equations for leaky Lamb waves, Eq. (2.45) and (2.46), turn up as zeroes in the reflection coefficients for a plate in fluid.

The "dips" seen in Fig. 2.14 therefore correspond to Lamb modes, and for each frequency, the theoretical optimum angle for exciting each mode can be calculated. That is done by matching the horizontal wavenumber and frequency of the incident pressure wave with the targeted mode. From Snell's law, one finds that the optimal incidence angle is given by

$$\phi_c = \sin^{-1}\left(\frac{c_f}{c_{ph}}\right). \tag{2.84}$$

The c-subscript indicates that this is only valid for plane wave excitation, meaning the center frequency and wavenumber of any transient pulse. For the A_0 mode at 250 kHz in a 1 cm thick steel plate, $\phi_c = 32$ degrees.

If the plate is on top of heavy cement, the reflection coefficients R_c will naturally be different from R_w. The difference is shown in Fig. 2.16, and the two most notable features are that the dispersion curves line up quite well and that the coefficients around the modes are narrower and deeper for R_w.

The discrete Fourier transform is used to implement response methods in practice. Considering a two-dimensional example, which is straightforward to expand upon, the incoming pressure signal on top of the surface depends on t and x, such as $p(t, x)$. A

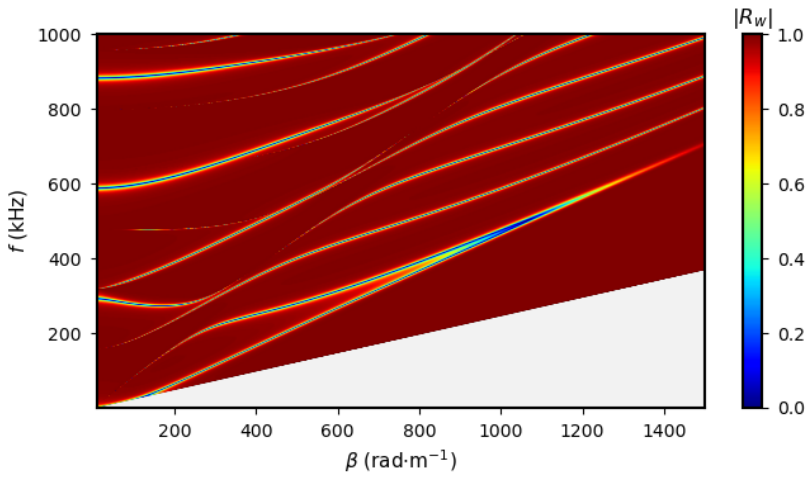

Fig. 2.15. Absolute value of reflection coefficients for a 1 cm thick steel plate in water. The gray area represents evanescent waves in water.

two-dimensional FFT can be used to get to the frequency-wavenumber domain

$$P_{in}(\omega, k_x) = \mathcal{F}_t \mathcal{F}_x \{p(t, x)\}. \tag{2.85}$$

The reflected wave is then given by

$$P_r(\omega, k_x) = P_{in}(\omega, k_x) \cdot R_p(\omega, k_x), \tag{2.86}$$

and the transmitted pressure wave can be computed by using T_p. Taking the IFFT gets the result back to the time-spatial domain.

The sampling theorem states that one must sample the highest temporal and spatial frequencies so that [18]

$$\frac{1}{\Delta t} > 2 f_{max}, \tag{2.87a}$$

$$\text{and} \quad \frac{1}{\Delta f} > t_{max}, \tag{2.87b}$$

to avoid aliasing. Additionally, using this method, the solution will be periodic in x as well, and the waves will wrap around from x_{max} back to $x = 0$. Hence, both t_{max} and x_{max} must be large enough to give negligible aliasing effects. The physics is useful to have in mind: While the incident pressure pulse might be short in time and space, in the limit an impulse, the reflected pressure will be a longer signal, at the very least because the plate must "ring down". That is especially the case for coupled plates, where two effects contribute to the longer duration of the impulse response. The first is that modes travel along with the plate, and the second that the reverberation of waves bouncing between the plates may be slowly attenuated in time. Therefore, sufficient zero-padding is critical.

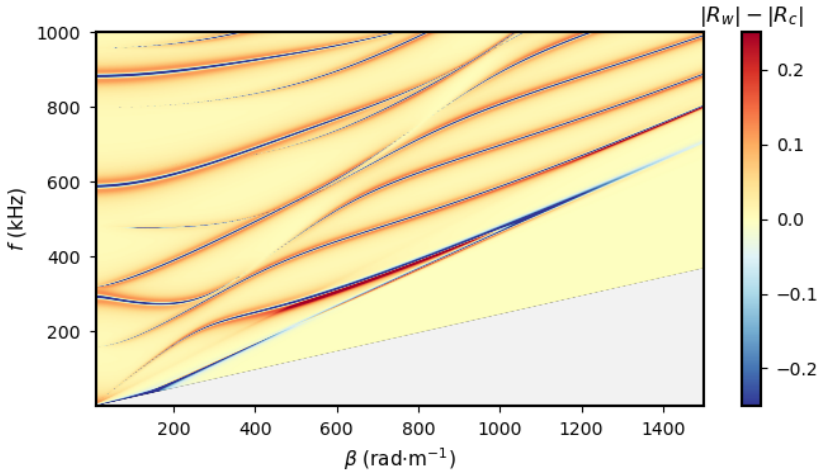

Fig. 2.16. Difference in absolute values of reflection coefficients for a 1 cm thick steel plate, either in contact with water on both sides (R_w), or water and heavy cement (R_c). The gray area represents evanescent waves in water.

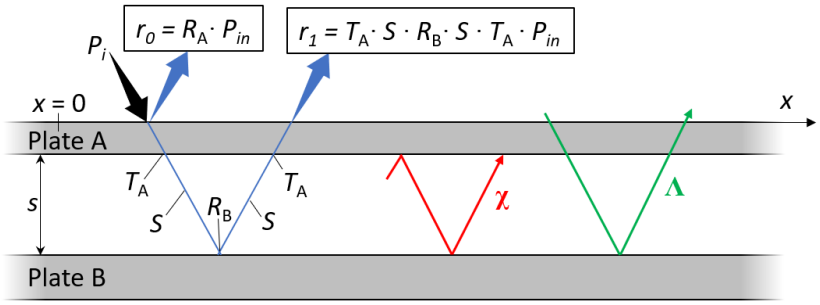

Fig. 2.17. Multiple reflections from an incident plane wave P_{in}. Later reflections are composed as a geometric series depending upon χ and Λ.

2.6.2 Two coupled plates

Response methods are well suited for modeling two coupled plates, and one of the reasons is the natural fit with the angular spectrum method for tilted planes. The tilting method is needed because while the global matrix method mentioned in Sec. 2.2.3 can already model two plates separated with a fluid, it only works if they are parallel. Modal methods could, in principle, be used as well, but it is shown in 4.1 that it is less accurate for a plate in contact with cement, not to mention the vastly increased complexity in implementing it. Therefore, the case with two plates is only described for response methods.

We start the analysis with two parallel plates labeled A and B, separated by a distance s, as seen in Fig. 2.17. An incoming wavefield $p_{in}(t, x)$ is incident onto the top plate A, which is immersed, with the same fluid on both sides. The response from the two plates will be composed of multiple reflections. In the frequency domain, the incoming wave is described by $P_{in}(\omega, k_x)$. The first reflected sound pressure r_0 is from

the interface to plate A:

$$r_0 = R_A \cdot P_{in}. \tag{2.88}$$

The following reflection component, r_1, is transmitted through the first plate A, propagated the distance s, then reflected from the second plate B, propagated the distance s again, before being transmitted through plate A:

$$r_1 = T_A \cdot S \cdot R_B \cdot S \cdot T_A \cdot P_{in}, \tag{2.89}$$

where S is the phase factor that incorporates the angular spectrum propagation between two planes. Note that T_A is equal in the first and second transmission because the same fluid is assumed on both sides of the plate. The next contribution, r_2 reveals a pattern:

$$r_2 = T_A \cdot \underbrace{S \cdot R_B \cdot S \cdot R_A}_{\chi} \cdot S \cdot R_B \cdot S \cdot T_A \cdot P_{in}, \tag{2.90}$$

where χ represents a round-trip between the two plates. It is clear that r_3 will be reflected one more time between the two plates, and each contribution will have another factor of χ. If one introduces the common factor

$$\Lambda = T_A \cdot S \cdot R_B \cdot S \cdot T_A, \tag{2.91}$$

the total reflection r_{tot} can be expressed as a geometric series

$$r_{tot} = r_0 + r_1 + r_2 + \ldots = P_{in}\Lambda(1 + \chi + \chi^2 + \ldots) = P_{in}\frac{\Lambda}{1-\chi}. \tag{2.92}$$

The effective reflection coefficient is $R_{tot} = \frac{\Lambda}{1-\chi}$. While such a method is effective from a computational standpoint, it is more likely to show wrap-around effects in the spatial domain. It may therefore be better only to compute the first few reflections that are of interest.

If one plate is tilted, an approach using Eq. (2.92) will not work. Instead one has to repeatedly apply a tilting operation $\measuredangle_\theta$, Eq. (2.82), between each reflection. The separation distance s is now taken to defined as in Fig. 2.13. There are at least two ways to go about this, but the simplest is to tilt the coordinate system before and after reflecting from the bottom plate

$$r_0 = R_A \cdot P_{in} \tag{2.93a}$$

$$r_1 = T_A \cdot S \cdot \measuredangle_\theta(R_B \cdot \measuredangle_\theta(S \cdot T_A \cdot P_{in})) \tag{2.93b}$$

$$r_2 = T_A \cdot S \cdot \measuredangle_\theta(R_B \cdot \measuredangle_\theta(S \cdot R_A \cdot S \cdot \measuredangle_\theta(R_B \cdot \measuredangle_\theta(S \cdot T_A \cdot P_{in})))) \tag{2.93c}$$

In the case of r_1, the incident sound field is transmitted through the first plate A, then propagated to the next plate B. Because plate B is tilted, a tilting operation by θ degrees is performed. In the new coordinate system, it is straightforward to calculate the reflected wavefield from plate B. Reversing the tilting operation is then performed with $-\theta$, but the wave vector components k_y are reversed as well, so the two cancels and the same sign of the tilting angle is used. The wavefield can then be propagated back to plate A and then be transmitted. For r_2, r_3, etc., more round-trips χ are included, where a tilt is applied before and after reflection factor R_B. It is clear that most of the

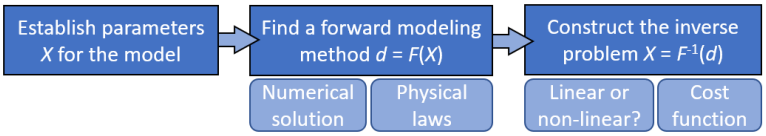

Fig. 2.18. Construction an inverse problem. The cost function is a way to quantify the misfit, and involves thinking about regularization.

intermittent results from Eq. (2.93b) can be reused in Eq. (2.93c), so computing, e.g., r_5 will not be as computationally demanding as one might first think.

The second method is here described for completeness, although it is unnecessarily complicated. It has been verified that it is possible to express, e.g., r_1 differently as

$$r_1 = S_s \cdot T_A \cdot \measuredangle_\theta(S_u \cdot R_B \cdot \measuredangle_\theta(S_d \cdot T_A \cdot P_{in})). \tag{2.94}$$

Here the propagation term is put between two tilting operations. The propagation down and up is along two non-parallel axes of different lengths, making it necessary to differentiate S as S_d and S_u. In addition, for each reflection, the coordinate systems of the two plates are shifted with respect to each other. A specifically chosen shifting must be introduced to re-align the origins, e.g., with a phase factor S_s.

The two plates are connected with fluid in our discussion, but the method could be extended to cover two tilted plates coupled by a solid instead. However, one must then consider that P-waves may be reflected and transmitted as S-waves and vice versa. Therefore, the tilting operation must also be applied to P- and S-waves separately. For visualization of wave propagation with parallel plates coupled by a solid, see [54].

2.7 The inverse problem

2.7.1 What is non-linear inversion?

Inversion is the process of finding underlying parameters $\boldsymbol{X}$ from a set of observation or reference data d_{ref} and requires solving an inverse problem. That is opposed to the forward problem F where one calculates data d_{mod} from the model given the underlying parameters

$$d_{mod} = F(\boldsymbol{X}). \tag{2.95}$$

An example of a linear forward problem is to blur an image with a Gaussian function (convolution). The inverse problem is to sharpen the blurred image, in other words recovering $\boldsymbol{X}$, using a mathematical model of the function that describes the blurring process (deconvolution), such as $\boldsymbol{X} = F^{-1}(d_{ref})$. Other examples of inverse problems include tomography and calculating the mass distributions in the earth given gravity measurements on the surface.

It turns out that inverse problems are more difficult than the forward problem, even if the exact mathematical model describing the forward problem is known. The reasons come down to [55]:

- **Existence:** The problem must have a solution, and in practice, there may be no model that exactly fits the data. That can occur because the mathematical model of the system is approximate or because the data are noisy.

- **Uniqueness:** There must be only one solution to the problem. However, two very different systems may be indistinguishable from their measurements.
- **Stability:** The solution must depend continuously on the data, but often tiny changes in the measurement lead to enormous changes in the estimated model parameters. Regularization is often employed (introducing a bias, e.g., penalizing large and rapid variations).

Many inverse wave propagation problems are non-linear and cannot be expressed with linear algebra and inverted directly. The problem is then one of global optimization: what parameters can be fed into the mathematical forward model to minimize the mismatch between the observed data and the model data? The mismatch is often quantified with a cost function (also seen under the names misfit, merit, objective, loss, or error function), and when the mismatch is at a minimum, the best estimate of the parameters $\boldsymbol{X}_{est}$ are assumed to have been captured

$$\boldsymbol{X}_{est} = \min_{\boldsymbol{X}} \text{Cost}\{\ F(\boldsymbol{X}), d_{ref}\ \}. \tag{2.96}$$

The cost function can take many forms, and popular alternatives in machine learning include the MSE (mean square error). Other examples can be found in, e.g., geoacoustics; Lindsay and Chapman used a Bartlett beamformer [56], while Collins et al. [57] have defined different cost functions in the frequency domain for measurements where the phase is reliable and not. The latter point is essential, as a phase shift of especially half a wavelength (cycle-skipping) will give significant errors when using an MSE cost function naively.

Good reasons exist for expecting a slight phase shift in practice: In the through-tubing well logging situation, some relevant parameters, like the inner casing thickness, are given from, e.g., pulse-echo measurements or existing well logs. If the inner casing diameter is off by a few percentages, the dispersion will not be precisely modeled, and then the error may be compensated for in the inverse problem by wrongly estimating other parameters. An "inverse crime" [58] is to use the same model to generate test data and perform the inversion. Because real data is noisy and the model potentially even slightly wrong, the inversion and cost function should not be overly sensitive and break from minor expected errors.

2.7.2 Inversion strategies: Brute force and simulated annealing

Some of the main difficulties with non-linear inversion arise because the cost function can have a chaotic behavior. The most straightforward method of gradient descent, implemented by simply following the negative gradient of the cost function, starting from an initial guess of the parameters $\boldsymbol{X}_0$, is very likely to end up in a local minimum and get stuck there, completely missing the global minimum of interest. That brings up the need for a global optimization method.

The safest approach for global optimization is to test every possible combination of parameters and pick the one with the lowest cost. That is to brute force the problem, but the downside is that it may be extremely time-consuming. If the parameters need to be tested with fine increments, or there are many parameters, the number of permutations will reach astronomical numbers.

Simulated annealing (SA) is a strategy that intuitively is based on metallurgical annealing. A control parameter T, analogous to temperature, is introduced, and by reducing the T gradually, the system will settle into its lowest energy or cost state. Starting at a high temperature allows the algorithm to search the cost landscape more extensively, as it will often accept a worse solution and behave like a random walker. As the temperature decreases, the algorithm gradually tends toward only accepting better solutions with a lower cost, becoming more like a gradient-based method.

Starting from an initial guess $\boldsymbol{X}_0$, most variations of SA usually consist of the following steps:

- A perturbation to the parameters to get a new proposed solution $\boldsymbol{X}_{i+1}$.
- Evaluating the cost associated with $\boldsymbol{X}_{i+1}$.
- A decision to accept or reject the proposed solution, based on the cost of $\boldsymbol{X}_i$ and $\boldsymbol{X}_{i+1}$.
- A schedule to reduce the temperature T.

How each step should be implemented depends largely on the problem at hand, and many options are available. In any case, there are no guarantees of finding the global minimum within a reasonable time, so it is still essential to reduce the problem size if possible and use as much a priori information as available.

Chapter 3

Setup, simulation methods, and implementation

With the theory as a backdrop, this chapter will describe how the developed numerical models can be implemented and verified. Two test systems are defined for validation and inversion purposes, and the results are compared with reference simulations in COMSOL. The test systems are described in detail in **Sec. 3.1**, along with the COMSOL models. Both single and double plate setups are considered.

To model each plate, one can either take a modal or response approach. The modal methods are covered in **Sec. 3.2**, beginning with a technique to solve and trace the dispersion relation. A small section is then devoted to transient NME simulations for the single plate case.

In **Sec. 3.3** the response approach is described for two non-parallel and coupled plates. The two-dimensional case is prioritized, with some of the most central code given in Appendix A. The section also hosts a brief discussion about some aspects of three-dimensional simulations. Finally, **Sec. 3.4** covers the choice of cost function and describes a simple brute force inversion method.

3.1 System setup in simulations

3.1.1 Materials and geometry

Table 3.1: Material parameters used throughout the thesis.

Material	ρ (kg·m^{-3})	c_p (m·s^{-1})	c_s (m·s^{-1})
Steel	7850	5900	3200
Water	1000	1480	-
Light cement	1330	2250	770
Heavy cement	1800	3500	1850

The simulation methods presented in this thesis will be implemented using the Python programming language. For verification and inversion, each Python simulation

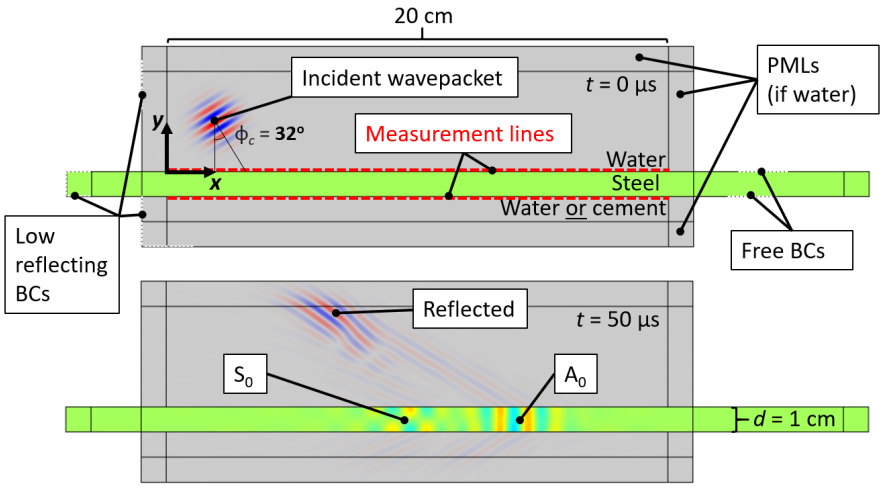

Fig. 3.1. COMSOL model with one plate. Snapshots of two time steps. The fluid domain shows pressure, and the steel shows the y-component of velocity.

has a corresponding COMSOL simulation, and the setups are explained with figures from the latter. Also, the same four materials are used throughout all chapters in this thesis, with their parameters given in table 3.1. The two types of cement are adaptations of class G cement and foam cement in [4].

The COMSOL model for single plate wave propagation is shown in Fig. 3.1, and the critical element is the steel plate, whereas the PMLs and BCs are specific to COMSOL. The plate has a thickness of 1 cm in all situations, but the length, here 20 cm, can vary. Above the plate is water, and below the plate, one might have either water or a type of cement. In the first frame, a Gaussian wavepacket is incident on the plate from the water, which is described in more detail in Sec. 3.1.2. As the wavepacket excites the steel plate, it reflects, and one can see in the second frame that an S_0 and A_0 wave propagates along with the steel plate. The pressure is sampled on the "measurement lines" indicated in the figure, with sampling above the Nyquist rate to capture the waveform development.

The double plate setup is shown in Fig. 3.2. The upper plate, labeled A, is still 1 cm thick. The bottom plate B can vary between 0.7 and 1.3 cm in this work and is backed by either water or cement. Plate B may be tilted relative to plate A, and the spacing distance between the plates s is defined for the center of the plate. The pressure is, for this situation, only measured above plate A. The tilt corresponds to non-parallel casings, which normally is less interesting than casing eccentricity in through-tubing well logging. However, simulating casing eccentricity requires tilting around an axis that does not exist in two dimension.

3.1.2 Excitation source in simulations

A simplified excitation source is used to compare the different methods. The principle in the pitch-catch technique is to target a particular mode, which can be done using Eq. (2.84). Because the excitation is always from a fluid, and in practice from a transducer, the strategy has been to initialize a complex Gaussian wavepacket as seen in, e.g.,

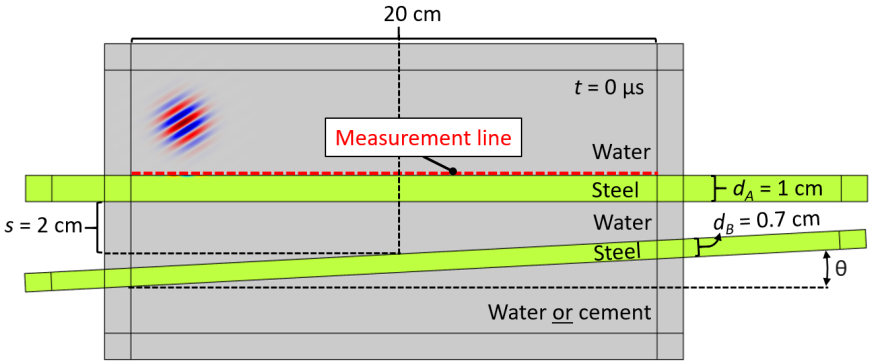

Fig. 3.2. COMSOL model with two plates. The bottom plate is tilted by 3°.

Fig. 3.1. The wavepacket is the product of a Gaussian window, and a complex plane wave, scaled by some initial amplitude p_0, which from here on is always set to 1 mPa:

$$p(t=0,x,y) = p_0 \cdot \text{Gaussian window} \cdot \text{Plane wave}, \tag{3.1}$$

where the complex plane wave is given by

$$\text{Plane wave} = e^{-ik_c[\sin(\phi_c)(x-x_0)-\cos(\phi_c)(y-y_0)]}, \tag{3.2}$$

where x_0 and y_0 determines the center of the wavepacket. As a reminder, $k_c = \frac{\omega_c}{c_f}$. The Gaussian window is given by

$$\text{Gaussian Window} = e^{-\frac{(x-x_0)^2+(y-y_0)^2}{2\sigma^2}}, \tag{3.3}$$

and the wavepacket will be circular with a fixed FWHM of twice the wavelength at the center frequency, or $\sigma = 4\pi c_f/(2.355\omega_c)$. Alternatively, if necessary, oval-shaped Gaussians could be defined if the wavepacket was desired wider (along wavefronts) or longer (along propagation direction). The location of the wavepacket is $x_0 = y_0 = 2$ cm in all simulations.

The pressure on the plate surface as a function of time, $p_{in}(t,x)$, is obtained by propagating the wave packet using an angular spectrum approach based on Eq. (2.2). Simply put, the method works by adjusting the phase of each complex plane wave component according to the dispersion relation and then sampling the pressure along the wanted plane. To speed up computations, which is needed in three-dimensions, the simulated domain $p(t,x,y,z)$ is small, and then zero-padded after sampling $p_{in}(t,x,z)$.

Mode excitation depends on both the geometry of the incoming wave packet and its frequency content. Rose [29] uses NME as a tool to analyze this with two concepts called *wave mode excitability* and *source influence*. Here we will instead look at the surface vibrational energy E (in the signal processing sense) in each mode m excited by the simplified excitation source, defined as

$$E_m = \int [v_y^{(m)}(x, y=h)]^2 dx. \tag{3.4}$$

It is not a physical energy, but is tightly connected with the radiated intensity of the modes, see Eq. (2.51), and therefore gives a practical measure for mode amplitudes. The

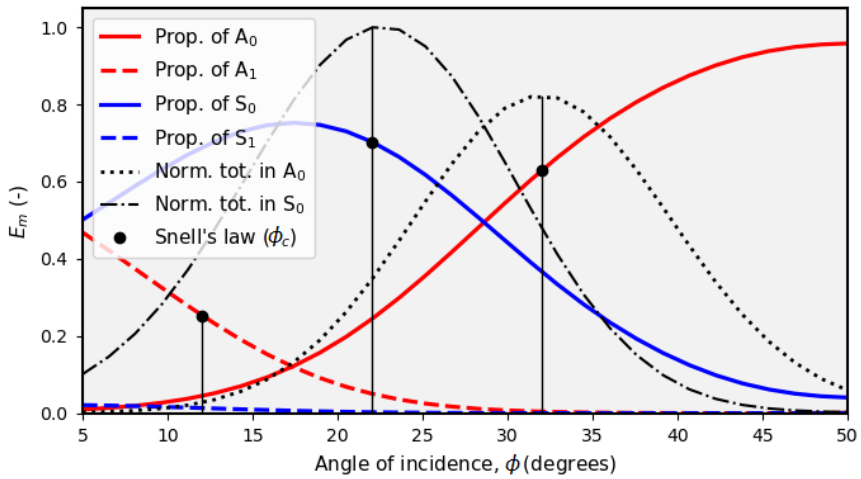

Fig. 3.3. Vibrational energy proportion in each mode as a function of incidence angle. The optimal angle for excitation given by Snell's law, Eq. (2.84), is marked for each mode where it is defined. The plate is 1 cm thick and in contact with water on both sides. The wave packet has a center frequency of 250 kHz, and a FWHM of twice the wavelength at the center frequency.

mode excitation is computed with NME (see Sec. 3.2.2), and the energy is measured 50 µs into the simulation, which is a short time after the incident wavepacket has been reflected, as seen in Fig. 3.1. The attenuation from the water on both sides of the plate is included.

Fig. 3.3 shows the proportion of energy in each mode, as well as the total normalized energy in the S_0 and A_0 modes. The optimal incidence angles from Eq. (2.84) is shown as well for the modes where it can be defined at 250 kHz. As can be seen, an incidence angle of 32 degrees obtained with Snell's law gives the maximum amount of energy in the A_0 mode. At the same time, the S_0 mode is also excited with roughly 35% of the energy, so, depending on the application, it may be worth increasing the incidence angle to target the A_0 mode more specifically at the cost of its total energy. It is also worth having in mind that the S_0 mode is significantly more dispersive than the A_0 around the chosen frequency, so it smears out and gets a relatively low peak amplitude.

3.1.3 COMSOL simulation

The COMSOL models have already been shown in Figs. 3.1 and 3.2. The simulations are set up as time-dependent studies, using the *Acoustic-Solid Interaction, Transient* physics that include the Solid Mechanics and Pressure Acoustics modules.

Referring to Fig. 3.1, the plates are extended out of the fluid domain to avoid early reflections from the ends of the plate. Therefore, free boundary conditions are imposed on large parts of the plate outside the water domain to allow continued Lamb wave propagation. Because perfectly matched layers (PMLs) are only supported for the pressure acoustics module, the plates are terminated with small squares at each end with low-reflecting boundaries. It is, however, not a perfect termination, as the low-reflecting

condition assumes normal incidence.

The edges around the water domain are covered with PMLs, backed with an impedance boundary condition, giving excellent absorption of outgoing waves. If the material below the plate is cement instead, the PMLs do not work, and the impedance boundary condition is swapped for a low-reflecting boundary.

The lowest speed of sound in the problem is used to define the maximum element size. Typically, that is the speed of sound in water, of $1480\,\mathrm{m\,s^{-1}}$. The center frequency is 250 kHz, but the highest frequency of significance is well within 500 kHz for the chosen wavepacket. The element size is set so that 6 elements fit into the smallest wavelength at 500 kHz, calculated as $1480/(500000 \cdot 6)$. Tests have verified that finer meshes, using 8 or 10 elements per wavelength, gave practically the same results. The time step is chosen automatically by the solver based upon the smallest element size in the mesh.

The plate is excited with an incident wavepacket from the water, defined in the initial values of the pressure acoustics domain. Following the previous section, it is described as a plane wave enveloped with a Gaussian. The time derivative is also given, as required by COMSOL, to make it propagate in the wanted direction. Unfortunately, properly defining the wavepacket is not trivial, as explained in the following paragraph.

By spatially enveloping the plane wave with a Gaussian, the spectrum of wavenumbers is broadened. Using the phasor notation, it is natural to express the time derivative of plane waves by multiplying with $i\omega_c$. Unfortunately, the dispersion relation in water $\omega_c/k = 1480\ \mathrm{m\,s^{-1}}$ will then, by definition, only be valid for the central wavenumber. As a result, a small spurious wavepacket can be seen to separate from the main one and propagates in the opposite direction due to this improper initialization (see the upper left corner, second frame in Fig. 4.6). A few methods, such as considering the broadening of the wavenumber spectrum when defining the time derivative, have been attempted to fix this. However, simply creating two wavepackets, where the second goes in the opposite direction from the first, gave the best result. The effect is that a spurious one accompanies the main wavepacket, and the PMLs absorb the unwanted wavepacket going in the opposite direction. An analysis of the error reveals that, compared to the Python implementation which should be exact, the COMSOL excitation signal, $p_{in}(t, x)$, has some inherent phase problems and 2.5% less energy. The two signals look similar to the eye, as seen in Fig. 3.4, but the slight offset contributes more to the deviation. The difference has an RMSE (root mean square error) of 6.9%, using the COMSOL signal as normalization. From a practical standpoint, the agreement seen is sufficient for comparing COMSOL and the presented methods, but it is nevertheless unfortunate that phase-aware metrics, such as the RMSE, are limited already by the calculation of $p_{in}(t, x)$.

3.2 Modal method implementation

3.2.1 Numerical solution of the Lamb dispersion relation

Equations (2.36) and (2.40) implicitly relate the frequency ω to a wavenumber β along the propagation direction. For any frequency, there are a finite number of purely propagating modes (A_0, S_0, A_1, S_1, etc.), as shown in Fig. 2.3. Tracing out the dispersion curves is necessary, and this section describes a procedure to do so.

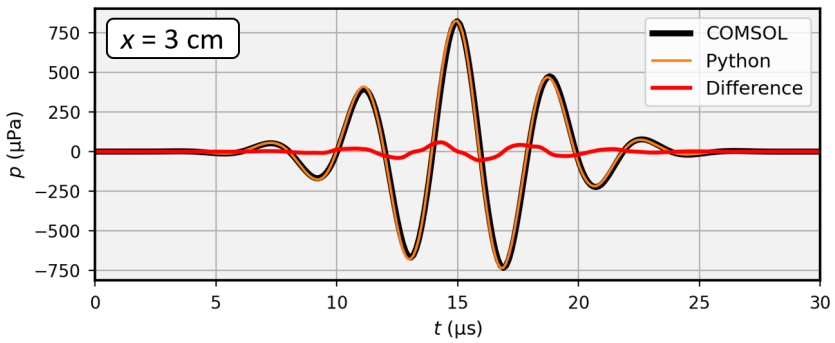

Fig. 3.4. Comparison of the excitation signal between COMSOL and Python at the position where the maximum difference is greatest, $x = 3$ cm.

The first step is to recognize that γ_s and γ_p will change from being real to imaginary depending on β and ω. This causes (2.36) and (2.40) to switch between having real and imaginary roots. As an example of a special case, it is known that the phase velocity for the A_0 mode is bounded between 0 and the Rayleigh wave velocity $c_R < c_s$, making the vertical wavenumbers γ_s and γ_p imaginary. For other modes, one or both of the vertical wavenumbers may become real at some point. Therefore, it is useful to rewrite the characteristic equations to simplify the analysis, so they take on only real values for real values of β. The result is given by Rose [29],

$$\frac{\tan(\gamma_s h)}{\gamma_s} + \frac{4\beta^2\gamma_p \tan(\gamma_p h)}{(\gamma_s^2 - \beta^2)^2} = 0 \quad \text{for symmetric modes,} \tag{3.5a}$$

$$\gamma_s \tan(\gamma_s h) + \frac{(\gamma_s^2 - \beta^2)^2 \tan(\gamma_p h)}{4\beta^2\gamma_p} = 0 \quad \text{for antisymmetric modes.} \tag{3.5b}$$

The curves change signs when crossing 0, so a root-finding algorithm can be used. However, one should take caution as the equations also change signs when crossing a pole. Depending on the algorithm used, one should test that the obtained root is, in fact, fairly close to 0. The curves are traced out as $\omega(\beta)$, as seen in Fig. 3.5 for two reasons. Firstly, these curves are two-to-one, meaning we can capture the back-propagating modes (negative group velocity, e.g., S_1 mode at low frequencies). Secondly, as Lowe points out [17], they are more easily traced out than say $c_{ph}(\omega)$, which perhaps is the most natural choice.

Tracing out the modes is a bit involved, in particular due to the possibility of having holes in the curves. The holes are regions where no roots are found for a mode, and the consequences are potentially that a mode is missed, or that one reaches a dead end when following a curve. In brief, the algorithm used here works as follows:

1. Choose either Eq. (3.5a) or (3.5b).
2. Make a list of β values: $(\beta_0, \ldots, \beta_i, \beta_{i+1} \ldots \beta_n)$ for a fine search for roots/modes along the ω axis.
3. For each β_i, trace out the modes found as follows:

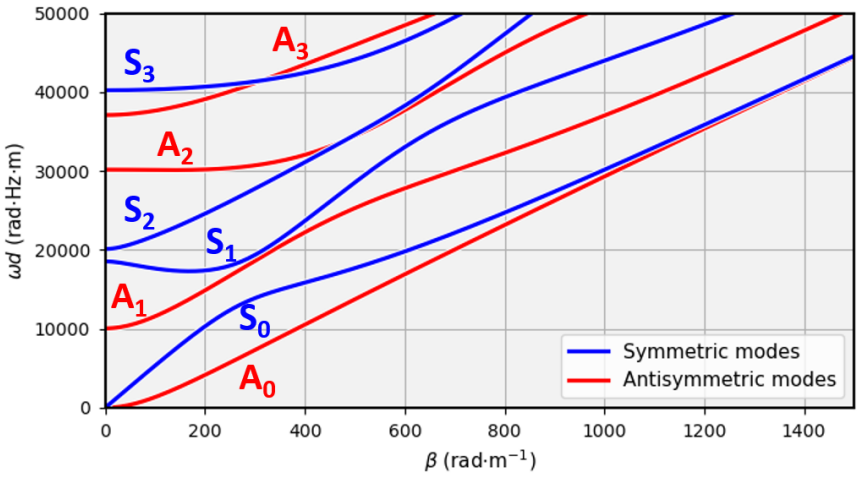

Fig. 3.5. Dispersion curves as they are traced out. Notice that the curves are not one-to-one, and more predictable than, e.g., the phase velocity Fig. 2.3.

i Store the values of each root as the intersection with a mode.

ii Do a similar search nearby $(\beta_i + \delta\beta)$ to estimate the derivative $\partial\omega/\partial\beta$.

iii Trace the modes (as far as possible) down to β_{i-1} and up to β_{i+1}, taking small steps of, e.g., $\Delta\beta = 5$, and store the result as a piece of a mode curve for the index i.

4. Starting from $i = 0$, go through each curve piece, and splice with the best matching curve piece in $i = 1$ (if any), then for $i = 2$, and so on:

   i Splice two curve pieces if they overlap at some point with a similar angle (< 5 degrees).

   ii If any curve pieces remain, they are attempted to be matched based on how well linear extrapolation finds the midpoint between the unconnected ends. An upper tolerable error threshold is defined from the derivatives $\partial\omega/\partial\beta$, and length of the gap.

   iii Unmatched curve pieces are at this point considered as new modes.

5. The fully traced modes are then labeled A_0, A_1, etc. based on their lowest frequency, in line with how higher modes have higher cut-off frequencies [28].

6. The mode curves are finally fitted with a spline function to get $\omega(\beta)$. For the inverse function $\beta(\omega)$ the fit ignores the back-propagating modes by only selecting the part of the curve with positive gradient $\partial\omega/\partial\beta$, so it is a one-to-one function.

When a spline function is obtained, it is easy and fast to work with, and the mode tracing is then isolated from where the dispersion relation is used. The method above has worked very well for steel plates and similar materials up to at least 1 MHz·mm, but no assessment has been conducted of general robustness for very different material parameters. Therefore, using the above method will require inspection and maybe

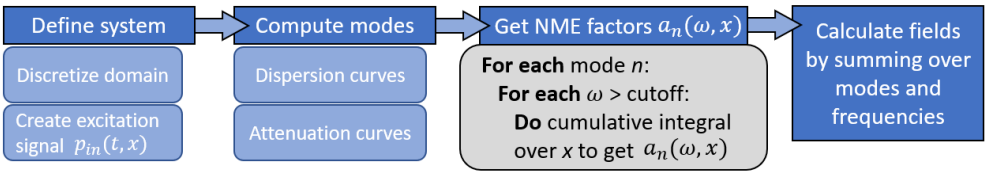

Fig. 3.6. Flowchart for calculating plate excitation via NME.

tweaking of hyperparameters, such as the step length $\Delta\beta$. Another point is that at very low frequencies, the A_0 and S_0 modes may be difficult to trace due to issues relating to the numerical range and precision of floats or doubles in the characteristic equations. In those situations, the low-frequency approximations given in [28] can be used. Finally, in cases where one is interested in general leaky Lamb dispersion relations, the wavenumber is complex, and the search for roots is significantly more difficult but still possible as described by Lowe [17].

3.2.2 Single plate excitation using NME

The NME technique is more challenging to implement than response methods and relies heavily on solving and tracing the Lamb dispersion curves. Because it essentially is a perturbation method by assuming the free plate solution, it is also not so accurate when the plate is in contact with cement, so the calculation is only exemplified for single plates. The propagation direction is assumed to be towards positive values of x. The flowchart for how NME is implemented is given in Fig. 3.6, using theory described in Sec. 2.3 and Sec. 2.4.

The first step is to define the system, consisting of a plate and two adjacent materials. The extent of the simulated domain (x_{max}) must be decided, as well as the simulation time (t_{max}). Because NME gives control over each mode individually, one can, in many cases, decide upon the right amount of zero-padding to avoid wrap-around effects in the solution by "killing off" the modes that enter an extended part of the domain [8]. Secondly, according to the sampling theorem, the dimensions must be discretized to resolve the shortest wavelength and highest frequency. For the excitation signal p_{in} chosen, 4-5 samples for each center wavelength in water and frequency have been enough, giving sufficient resolution of frequencies and relevant wavenumbers up to 500 kHz.

The next step is to compute the dispersion curves, which is explained in the previous section. The corresponding attenuation curves are also calculated here using the perturbation method. It has been helpful to employ object-oriented code, in order not to lose track of how different structures and modes are connected.

The NME factors can then be integrated, which has to be done for each mode and frequency. The system is defined so that only the S_0, S_1, A_0, and A_1 modes need to be considered. The excitation signal is converted from the (t,x) to (ω,x) domain, and the modal participation factors a_n can be integrated for each mode and frequency. The integration is cumulative because each mode is cumulatively excited by the source, and the Scipy method `integrate.cumtrapz` can be used. However, when the excitation zone is known, there is no need to integrate beyond that.

The last step is to calculate the wanted fields. This involves using Eq. (2.69). If the

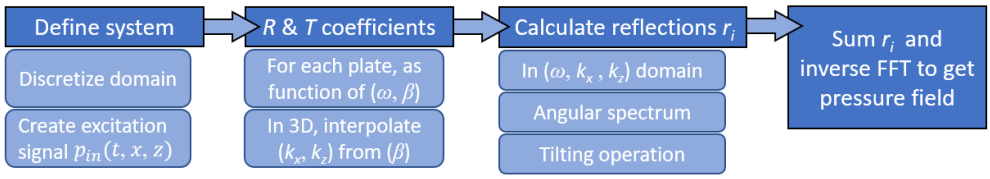

Fig. 3.7. Flowchart for calculating plate response.

pressure above or below the plate is desired, that would require applying a conversion factor from Euler's equation to the field of $v_y(h)$.

3.3 Response method implementation

Implementing the response method is a bit more straightforward than with NME. It is also the only method used in this thesis for coupled plates and full three-dimensional simulations. The flowchart is shown in Fig. 3.7, using theory described in Sec. 2.5 and Sec. 2.6. The code for calculating the two-dimensional case is given in Appendix A.

The first step is to define the system, which consists of one or two plates, their thicknesses, tilts, separation distance, and adjacent materials. The extent of the simulated domain (x_{max}, and also z_{max} for the three-dimensional problem) must be decided, as well as the simulation time (t_{max}). As opposed to NME, we have no control over each mode, and everything that happens in the simulation is directly tied to the sampling and length of the excitation p_{in}. To avoid wrap-around effects, one must define large domains to allow the waves to fade out. Luckily, one does not have to compute every reflection component r_i, and in the wast number of applications, some wrap-around effects are acceptable. As before, 4-5 samples for each center wavelength and frequency in water have been sufficient. If the array dimensions are re-adjusted to be in powers of two (128, 256, etc.) to give faster FFTs, it has been found better to use the extra samples to increase the domain size (i.e., increasing x_{max}), rather than sampling the original domain more densely.

The next step is to compute the reflection and transmission coefficients, R_A, T_A, R_B. Because this step involves double for-loops and computing and inverting many matrices, it is a good place to optimize the code, as has been done using the Numba just-in-time compiler. Another great speed-up can be achieved by exploiting symmetry; $R(\pm\omega, \pm\beta) = R(\omega, \beta)$.

For three-dimensional simulations, the coefficients must be known for wavenumbers in the z-direction as well, such as $R(\omega, k_x, k_z)$. Because $\beta = \sqrt{k_x^2 + k_z^2}$, it is faster to interpolate $R(\beta)$ for each frequency as shown in Fig. 3.8. The sampling of the coefficients of β must be fine enough to give accurate interpolation, and it seems necessary to use a finer resolution of β than given by the Fourier frequencies of the domain sampling in x, i.e., k_x. Ten times finer resolution has been used in this work, but the number was chosen arbitrarily to be well within safe limits. Thus, a coarser resolution may also be able to give sufficiently accurate results.

The excitation signal must be transformed to the frequency domain to calculate the reflection contributions, r_i. With the problem formulated in the (ω, k_x, k_z) domain,

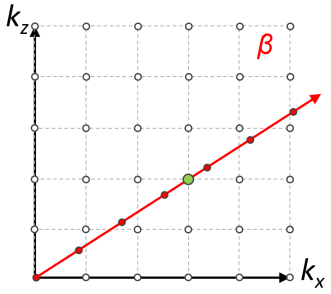

Fig. 3.8. For each frequency, the reflection coefficient can be interpolated (●) at any combination of k_x, k_z from β (●).

the corresponding phase factors for angular spectrum propagation are defined as $S = e^{-ik_y s}$, with k_y being a multi-dimensional array calculated from ω, k_x, and k_z. The reflections are then calculated by multiplying together the multi-dimensional arrays, and the pressure can be obtained by taking the real part of the inverse Fourier-transformed result.

The tilting operation is used before and after multiplication with R_B. Naturally, the interpolation must be called for every non-evanescent combination of frequency and wavenumber in the rotated system to fill in the reconstructed signal. The interpolation method can be chosen freely, and tests indicated linear interpolation to be sufficient and cheaper to compute than quadratic or cubic. An efficient algorithm is used that calculates the array indices to interpolate between directly, instead of, for instance, constructing spline objects first. For this to work straightforwardly, the spectra should be stored in multi-dimensional arrays where the wavenumbers are strictly increasing, which is done by applying a `fft.fftshift` before interpolation. Negative frequencies can be ignored because they do not contribute to the result, and to speed up the triple for-loops, Numba was used.

There is a detail to mention about *where* on the plate the tilt axis is located. The tilt is by default applied around the first sample, such as `x[0] = 0`. Therefore, it is necessary to use a method like `fft.fftshift` to align the central position of the plate with the tilt axis. A second consideration arises if the simulated domain is longer than the plate (i.e., zero-padding), in which case one must re-adjust the alignment using for instance `np.roll`.

3.4 Strategy for the inverse problem

3.4.1 Choice of cost function

To de-emphasize the importance of phase but keep the timing information, the Hilbert envelope of the measured pressure time-domain signals is taken, denoted as $\text{env}\{p\}$. In this context, the index i indicates a receiver transducer with n in total. The cost is calculated as the **m**ean of the **r**oot **N**oise-to-**S**ignal **R**atio, mrNSR for short. The "noise" is understood as the mismatch between the model and the reference. The "signal" is the reference, which itself is a signal from a simulation or measurement. The mathematical

expression is

$$\text{Cost} = \text{mrNSR} = \frac{1}{n}\sum_{i}^{n}\sqrt{\frac{\int(\text{env}\{p_{ref,i}\} - \text{env}\{p_{mod,i}\})^2 dt}{\int \text{env}\{p_{ref,i}\}^2 dt}}, \tag{3.6}$$

and should return values between 0 and 1 in most situations of interest. The cost function gives equal weighting to any receiver i, which is a crucial point. An alternative to a general cost function as described here, in the sense that no assumptions are made about the measured signal, is to create a cost function based on feature engineering as in Viggen et al. [3]. In that work, the inversion relies on a mathematical model where measuring the peak value of individual A_0 wave packets, a feature of the signal, is necessary.

3.4.2 Inversion method

The primary goal of inversion in this thesis is to demonstrate that it is possible in principle. It will be shown in the next chapter that the cost function is most sensitive to the geometry parameters, like the tilt angle, and that very little information is usually available in the gradient unless the parameters are close to the true value. Performing inversion with no prior knowledge then becomes a challenging task, but in a practical setting, one should know much of the geometry already; either from drilling and installment, inversion of a previous part of the casing, or other methods such as pulse-echo.

The inversion is usually less sensitive to material parameters ρ, c_p, and c_s, but the main task in well logging is to separate between classes of materials. Because there should be a limited number of possible materials outside the second casing, the inversion will look for the best material from the selection of heavy cement, light cement, and water.

When performing the inversion, the receivers are approximated as point hydrophones on the surface of the plate. Two points are measured, and for the actual inversion of a COMSOL simulation, like that illustrated in Fig. 2.17, the points are located 10 and 17 cm from the left end of the measurement line.

In the complementary parameter sensitivity analysis, which is not limited by running COMSOL simulations, the simulated system is made longer with a plate length of 0.8 m. The receiver configuration is also quite different and more similar to what is discussed in the literature [3, 4]. The first receiver is then located 30 cm away from the left end of the measurement line. The next are placed at 10 cm intervals, depending on the number of receivers n, which will be clearly stated.

After attempting to use simulated annealing, it was found that brute-forcing the problem would be more reasonable. The casing thicknesses d_A and d_B are assumed known, whereas the spacing s and tilt angle θ are known to be within some narrow range. The ranges are discretized, here in 11 steps, and for each permutation and material candidate, the cost is calculated against the reference measurement from COMSOL. The material associated with the lowest cost obtained is taken to be the material behind the second plate.

Chapter 4

Results and discussion

The results are presented in three parts. In **Sec. 4.1** the computational methods developed are validated against COMSOL. Both modal and response methods are shown for the single plate case, whereas only modal methods are used for two coupled plates.

Sec. 4.2 considers inversion. First, the possibilities to perform inversion are discussed, with a study on the sensitivity to different parameters. Focus is then directed to detecting heavy cement, a "difficult" material, behind two tilted plates. A mechanism is explained for how the detection is possible. Inversion is then carried out on the results from a smaller COMSOL simulation, verifying the forward model and the principal possibilities of performing inversion.

The last important topics are included in **Sec. 4.3**. A qualitative demonstration of three-dimensional propagation is given, which has been difficult to verify due to the computational requirements of COMSOL. Finally, the execution time of the code used is quantified.

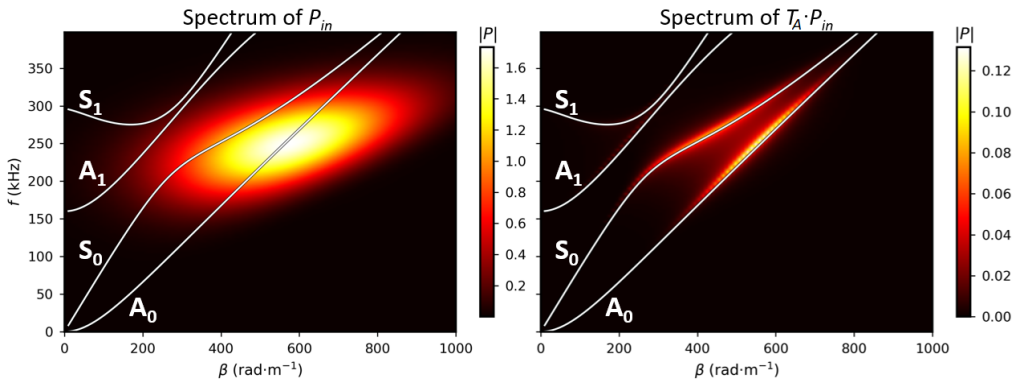

Fig. 4.1. f-k plot of the excitation P_{in} to the left. The transmitted spectrum through a 1 cm thick steel plate is shown to the right.

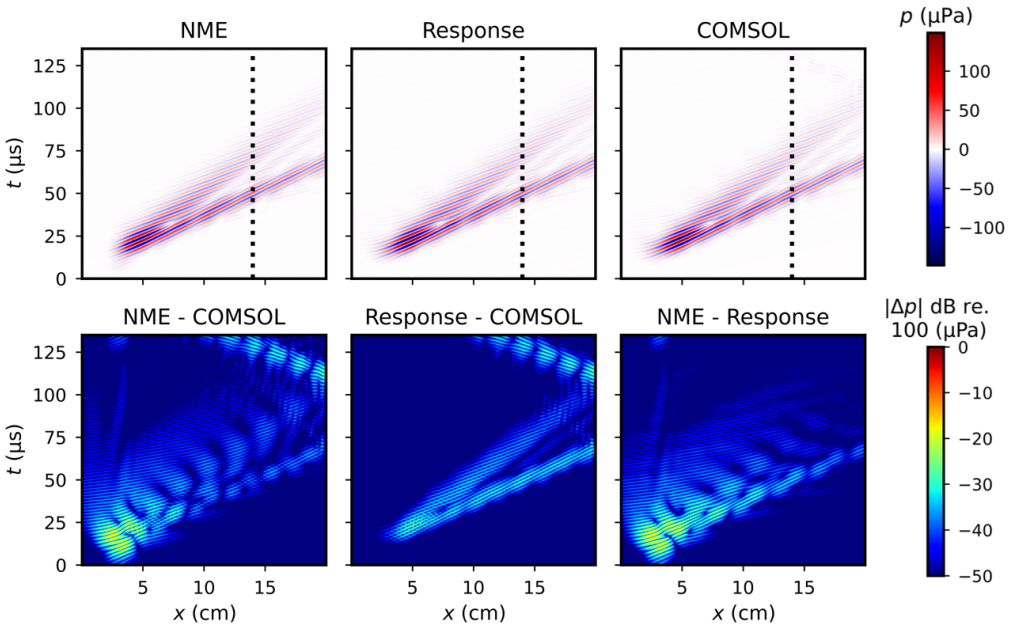

Fig. 4.2. A comparison of different methods for the pressure transmitted through a steel plate. The top row shows the pressure on a linear scale, while the bottom row shows the difference between each method on a decibel scale. The black line refers to Fig. 4.3.

4.1 Verification of the forward model

4.1.1 Transmission through a plate in water

Using the simplified excitation source described in Sec. 3.1.2, Fig. 4.1 shows the spectrum of plane waves in the incident wave P_{in} in an f-k plot. The wave targets the A_0 mode in the 1 cm thick steel plate, as intended. The second plot shows the transmitted spectrum using the response method, and it is clear that S_0 waves are excited. The attenuation of modes contributes to making the spectrum less sharp around the mode lines.

Fig. 4.2 shows the transmitted sound pressure in the t-x domain, using different techniques of computations. The pressure is recorded just below the plate at 600 different time intervals and sampled on a grid of 500 points.

Concentrating on the first row, it is not easy to see any apparent differences between NME integration, the response method, and COMSOL. To get a better impression of the agreement between the methods, the waveform on the black dotted line, at 14 cm, is plotted in Fig. 4.3. NME is used to calculate the contribution from each mode, as seen in the upper plot of Fig. 4.3. It is evident that only the A_0 and S_0 modes contribute significantly and that the S_0 mode is very dispersive as can be expected from its steep gradient at 250 kHz in the group speed plot, Fig. 2.4. The total waveforms are plotted in the second window, and the three curves are to the eye superimposed, with good agreement in both phase and amplitude.

In the second row of Fig. 4.2, the differences between the methods are plotted on the decibel scale. The reference level is set at 100 µPa, which is one-tenth of the amplitude

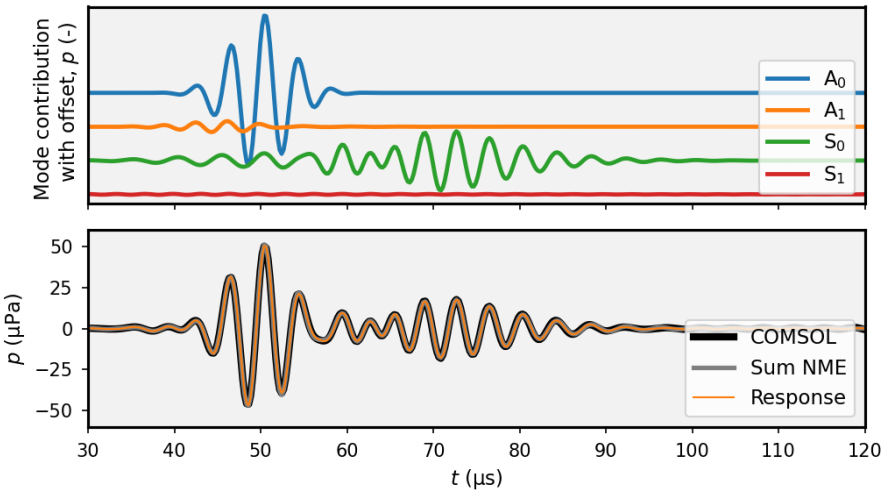

Fig. 4.3. The waveforms sampled on the black lines in Fig. 4.2. The upper window shows the mode contribution given by NME, and the bottom window compares the waveform from the different methods.

in the incident wave. A difference of $|\Delta p| = 1\,\mu\text{Pa}$ translates to roughly -40 dB, or 2% of the peak pressure at the 14 cm line. The best overall agreement is between the response method and COMSOL, where the visible error is in the two modes A_0 and S_0. Given that the magnitude of the error is similar of about 2%, it is likely largely due to the slight imperfections when re-creating the same excitation p_{in} in COMSOL and Python, as discussed towards the end of Sec. 3.1.2. A reflection from the imperfect non-reflective boundaries can also be seen in the COMSOL implementation after around 100 µs.

NME may seem to have better agreement with COMSOL when it comes to the propagating A_0 and S_0 and modes, but it does not capture the initial dynamics from the excitation well. Considering that the wavefield locally around the excitation zone may not be expressed from only propagating modes, that is an expected result and must be taken as a feature of the method.

The remaining error in NME, particularly seen as a smudged-out color above the excitation zone, seem to have a mode-like behavior. That hints toward a problem with the dispersion relation used. The suspected main reasons can be seen in Fig. 3.5 in the S_1 mode. First, and most importantly, the cut-off frequency, defined as the intersection with the ω-axis, is not the lowest frequency of the mode, and the code implementation ignores frequencies below the cut-off. Second, the modes may be difficult to trace near cut-off, and in those cases, the curves are extrapolated using splines, which may impact the near-zero group velocities of some modes.

4.1.2 Reflection from a plate on a cement half-space

The reflection is measured as the pressure on the upper plate surface. Transmission can be calculated for P- and S- waves, but is not interesting for the purposes of this thesis. Fig. 4.4 shows the pressure on the upper plate surface with time. As opposed to the

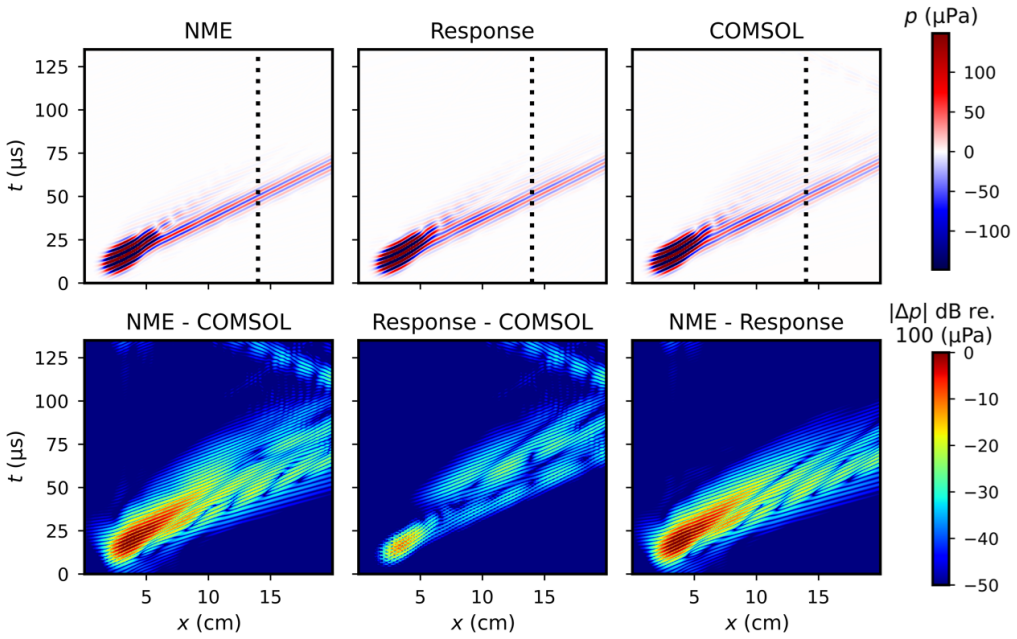

Fig. 4.4. A comparison of different methods for the pressure reflected from a steel plate on a half-space of heavy cement. The top row shows the pressure from each method on a linear scale, while the bottom row shows the differences on a decibel scale. The black line refers to Fig. 4.5.

case with a plate in water, the S_0 mode is barely visible. That is especially evident in the waveforms of each mode, as seen in Fig. 4.5, and the reason is that the mode couples very strongly to heavy cement and gives an attenuation α of more than 30 Neper (Fig. 2.11), as opposed to roughly 13 Neper for the water (Fig. 2.9).

In this situation, NME is performing much worse, shown in Fig. 4.5. Firstly it looks as if the wavepacket arrives earlier, which hints toward a slight inaccuracy in the dispersion relation. Secondly, the attenuation is somewhat underestimated by the perturbation method. Recalling that both Lamb waves and the perturbation methods used for NME are only exact for a free plate, the assumptions are stretched when the cement has 23% the density of the plate. Hence, and because of the increased complexity in implementing the technique, NME is not suitable for building a general forward model. It is, however, still a very valuable tool for understanding the problem and seems to give at least a reasonable estimate.

The differences between the methods are plotted in the second row of Fig. 4.4. Note again that the incident pressure has an amplitude of 1000 μPa, as opposed to the reference pressure at 100 μPa. The maximal $|\Delta p|$ in the Response-COMSOL plot, of -15 dB or so, is therefore consistent with the 2% relative error in the excitation wave packet p_{in}.

4.1.3 Reflection from coupled tilted plates

The attention is now directed towards coupled plates, where the transmission and reflection of single plates are used together with the angular spectrum propagation and

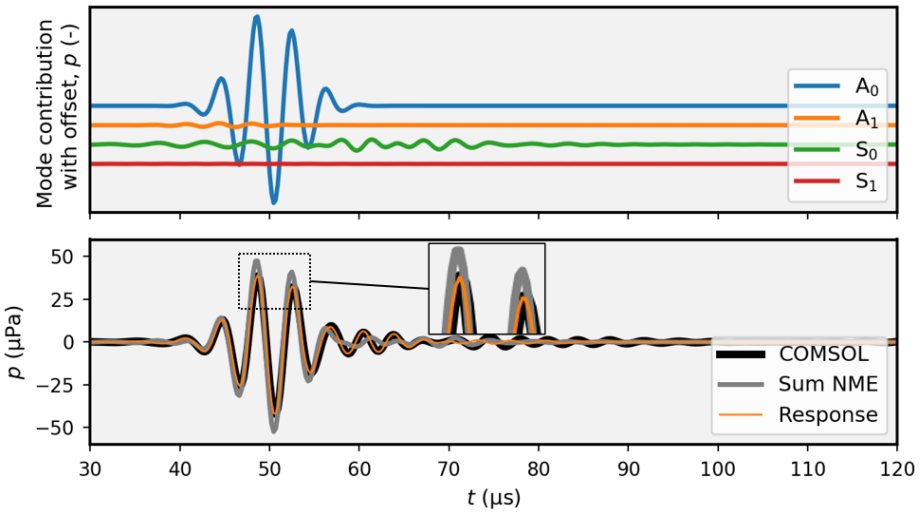

Fig. 4.5. The waveforms sampled on the black lines in Fig. 4.4. The upper window shows the mode contribution given by NME, and the bottom window compares the waveform from the different methods.

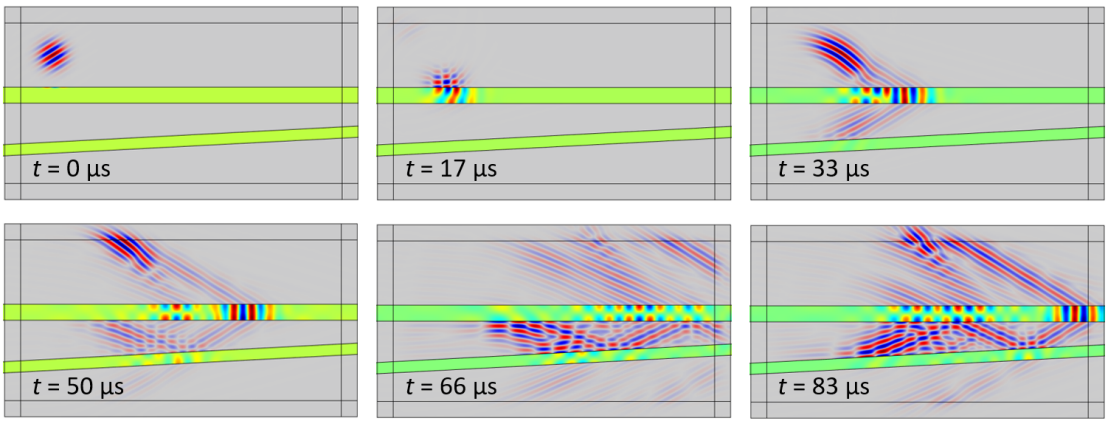

Fig. 4.6. Snapshots from COMSOL showing two coupled steel plates in water. The color ranges of pressure p in the fluid and velocity component v_y in the steel are readjusted between each frame.

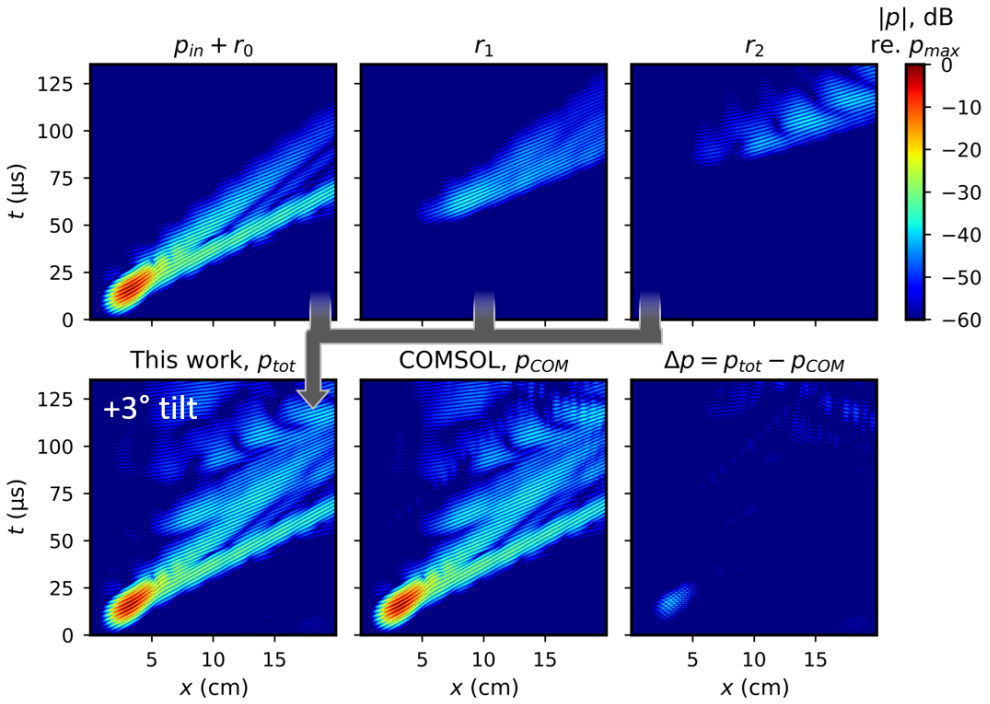

Fig. 4.7. Reflected pressures from a stack of two tilted plates with a 3° tilt. Different components of the reflected pressure is shown in the upper row, and the total is shown in the bottom row. $d_A = 1.0\,\text{cm}$, $d_B = 0.7\,\text{cm}$, $s = 2.0\,\text{cm}$, and the bottom plate is above a half-space of heavy cement.

the tilting operation. A series of snapshots from a COMSOL simulation is shown in Fig. 4.6, to illustrate the wave propagation. The pressure signal used for comparison is measured on the upper side of the top plate. The top and bottom plates are referred to as plates A and B, respectively.

The first verification is made using an upper plate of thickness $d_A = 1.0\,\text{cm}$, a bottom plate of thickness $d_B = 0.7\,\text{cm}$, a tilt of $\theta = 3°$, a separation $s = 2.0\,\text{cm}$, and the backing a half-space of heavy cement. The result is shown in Fig. 4.7, using the peak pressure as the reference throughout. The upper row show the different contributions to the total pressure, where the $p_{in} + r_0$ is identical to the pressure reflected from a single plate in water. The sum of the reflections up to r_4 is shown side-by-side with the equivalent COMSOL model.

Similar simulations have been performed with different tilting angles as shown in Fig. 4.8. A clear agreement exists between the developed computational method and COMSOL, confirming that the tilting operation in the wavenumber domain is working as intended. In the upper right plot, the errors are labeled, although they may be difficult to see: **a)** is the error in the incident wave p_{in}. **b)** is a wrap-around/aliasing effect in the presented method. The plate considered is 0.2 m in length, but the simulation runs with a length of 0.5 m. The wrap-around happens along spatial and temporal axes, illustrating that a bigger domain could have been defined. This error is most visible in the 0° tilt case because parallel plates are more "resonant", meaning waves more

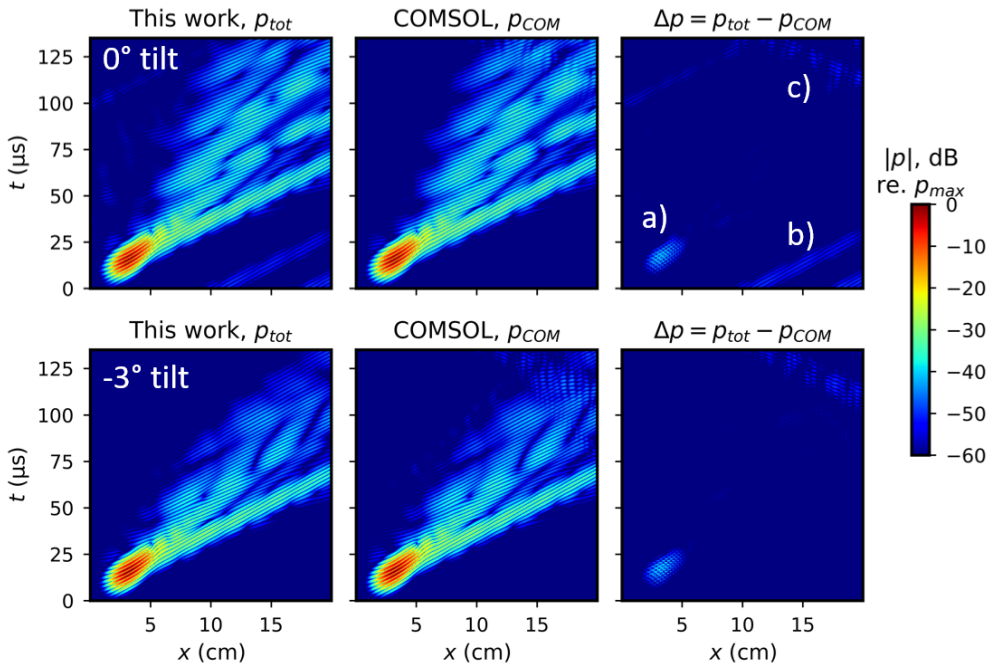

Fig. 4.8. Reflected pressures from a stack of two plates and tilt angles of 0° and −3°. Otherwise similar to Fig. 4.7. Errors labeled **a)** to **c)** are explained in the text.

easily couple to plate A after multiple reflections between the plates, and also to plate B if the thicknesses of the two plates match. **c)** marks the reflection from an imperfect non-reflective boundary condition in COMSOL.

Lastly, the waveforms are inspected at the 14 cm mark on the plate. Fig. 4.9 shows the contribution from each reflection in the 3° degree tilt configuration to the total pressure. As seen, the waveforms from the presented work and COMSOL are very similar. The difference Δp is plotted with an offset to get an idea of the deviation, and a part of it seems to come from a slight phase shift, as the last reflection in the 3° degrees case could indicate. Wrap-around effects and other discussed errors are likely to be main contributors to the difference. The influence of introducing a tilt is clear, and the agreement between COMSOL and the presented method is well within the requirements of creating a working forward model.

4.2 Inversion of the two-dimensional problem

4.2.1 Parameter sensitivity and limits to inversion

Successfully solving the inverse problem requires that the cost function is sensitive to the parameters of interest and displays a global minimum at the correct set of parameters. Table 4.1 lists the parameters that are tweaked in the model and their ranges in the sensitivity analysis from X_{low} to X_{high}. Three cases have been defined that differ by the thickness of the bottom plate d_B and the tilt angle θ. The thickness of the inner plate A, d_A, is not included in the study.

A simplified setup of the pitch-catch logging system is simulated, using the point

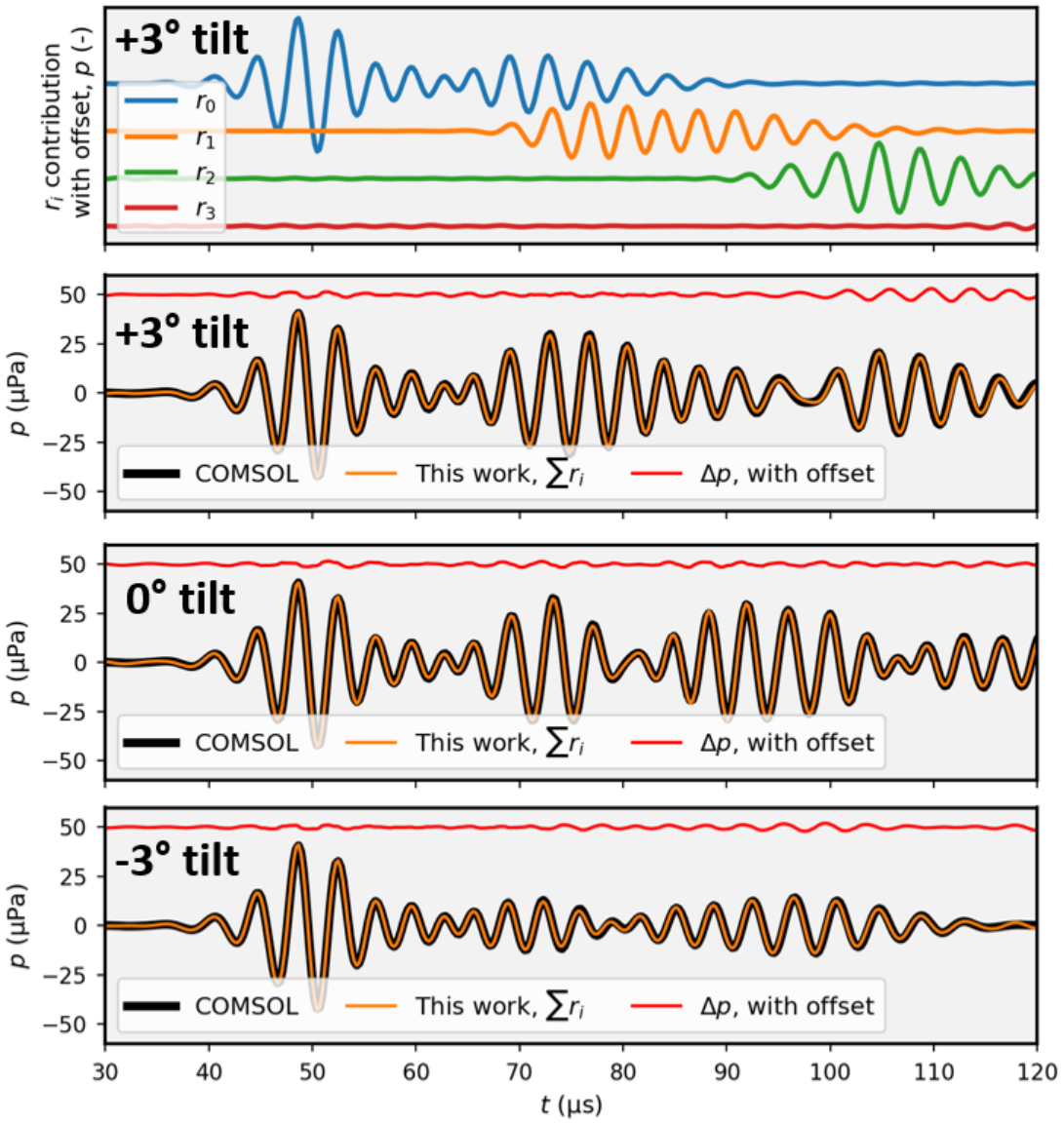

Fig. 4.9. Waveforms at the 14 cm position for three different tilting angles.

hydrophone approximation for the receivers. 30 cm from the excitation, and then in steps of 10 cm, the pressure is recorded as a function of time on the plate surface. Two receiver configurations are considered, one with two such "receivers" at 30 and 40 cm, and one with five receivers at 30, 40, 50, 60, and 70 cm. Each parameter X is varied between X_{low} to X_{high}, keeping the other constant, and the cost function is calculated with the true parameters as reference. The effect on the cost is shown in Fig. 4.10.

Table 4.1: Parameters used in the sensitivity analysis.

Parameter	X_{low}	X_{mid}	X_{high}	Case A	Case B	Case C
d_A (cm)	0.7	1.0	1.3	1.0	1.0	1.0
d_B (cm)	0.7	1.0	1.3	1.0	0.8	1.2
s (cm)	1.0	2.0	3.0	2.0	2.0	2.0
θ (deg)	-3.0	0.0	3.0	0.0	2.0	2.0
ρ (kg·m^{-3})	500	1500	2500	1500	1500	1500
c_p (m·s^{-1})	1300	2400	3500	2400	2400	2400
c_s (m·s^{-1})	0	925	1850	925	925	925

From Fig. 4.10, it seems as if the cost function is sensitive to every parameter and that using five receivers is at least marginally better than 2 in most situations. Typical for all three cases is the sharp notch for the θ and s parameters. Further research is needed to make a conclusive statement, but it seems likely that inversion of the geometry parameters θ, s, and d_B is usually possible, at least when some of the parameters are known.

The sensitivity to the material parameters is strong in case A with parallel plates of equal thickness. However, the sensitivity is reduced when a tilt is applied, as in cases B and C. Case C has a thicker bottom plate, which seems to partially compensate for the tilting, compared to a thinner plate as in case B.

The observed differences in the material parameter sensitivities are explained by the waves' need to couple into the second plate to interact with and probe the material. In case A, that occurs, as waves emitted from the upper plate match the optimal angle for modes in the bottom plate. On the other hand, if most of the energy is reflected from the bottom plate, such as in case B, the sensitivity to the material parameters is so low that it is not immediately clear if inversion is even possible in practice.

Luckily, the inversion should primarily distinguish between cement and water, and therefore the material parameters are not independent of each other. The type of cement used in a borehole will be known from the time of drilling, and the question is how sensitive the system is when there is water or drilling fluid behind the casing instead. Different thicknesses d_B and tilt angles θ are swept, and using either heavy or light cement as a material reference, Fig. 4.11 shows the effect on the cost function if the material is replaced with water. It is immediately apparent that light cement is easier to detect than heavy cement and that d_B should be larger than or equal to d_A, which is true in practical situations.

It is worth restating that the tilt along the casing direction will typically be small. However, as it, in fact, is a real effect and the only way to test the method for tilted plates in two dimensions, it is useful to pursue the example of tilted plates further.

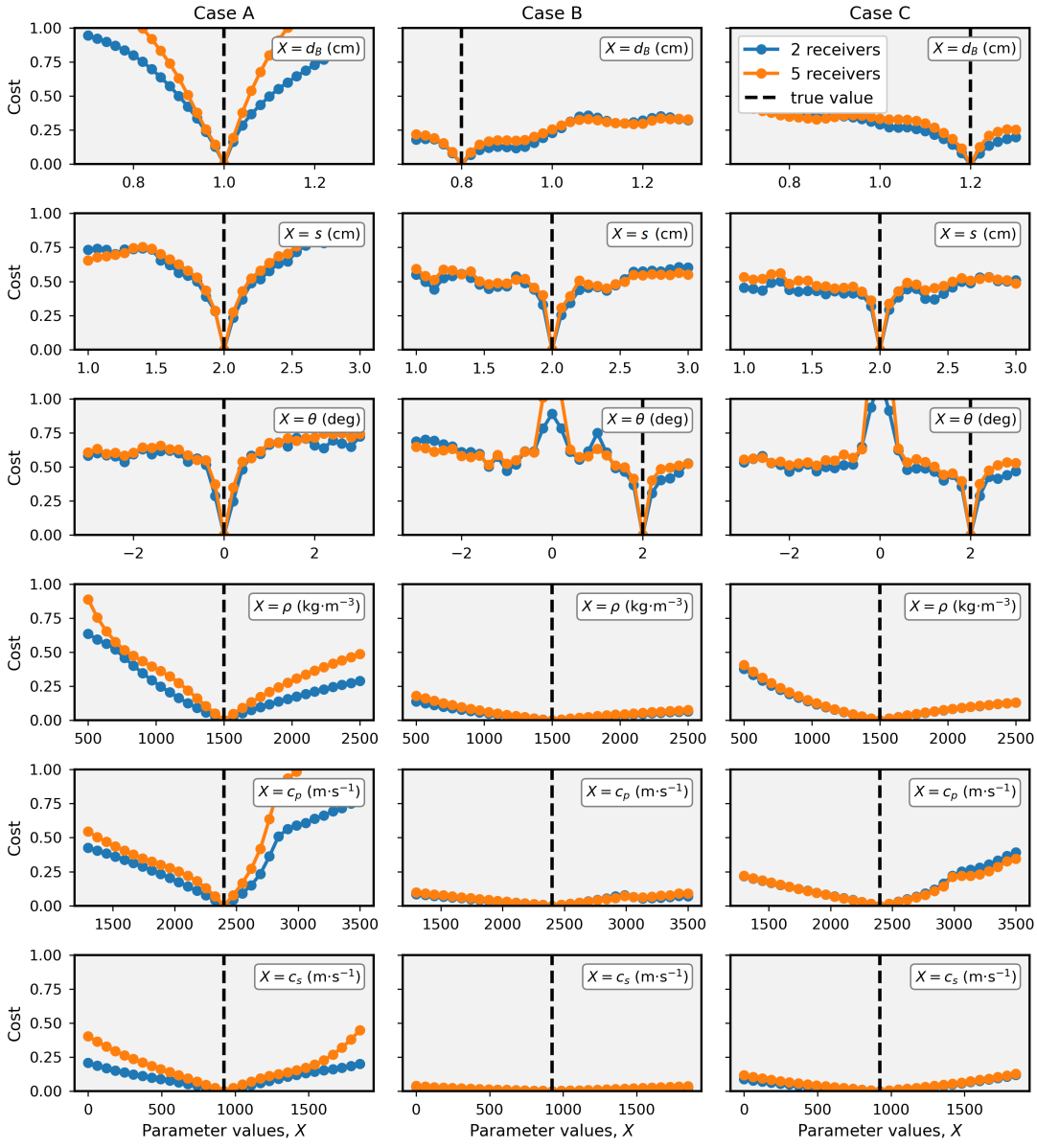

Fig. 4.10. Sensitivity of cost function by sweeping through parameter values in different cases listed in Table 4.1.

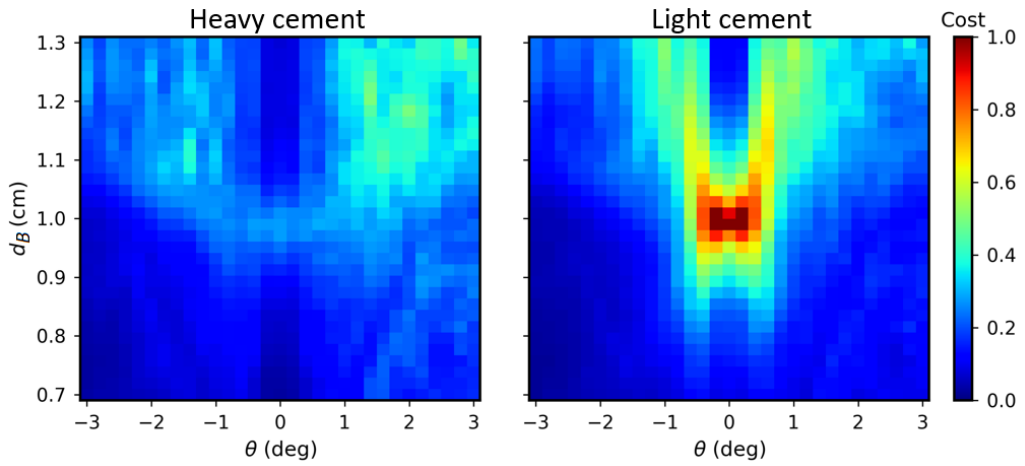

Fig. 4.11. Sensitivity to water behind the second plate using 5 receivers, initially assuming it be be one of two types of cement.

4.2.2 The mechanism for cement detection with tilted plates

Figure 4.11 showed the detailed relationship between cement detectability and the tilt and thickness of the bottom plate B. Notice from the upper right quadrant for heavy cement that it is easier to detect when the tilt is positive and the second casing somewhat thicker. To explain this takes a somewhat convoluted argument, so we start by reviewing the three requirements for cement detection:

1. The leaky wavefront from plate A must couple into plate B with the correct angle.
2. The Lamb wave modes in plate B must be attenuated differently by cement than by water.
3. The waves must be re-emitted from plate B in a way that allows for transmission through plate A and detection by one or multiple receivers.

This can also be understood as a filter chain. Taking inspiration from Fig. 4.1, the interaction of the incident spectrum P_{in} with each plate can be understood as applying an f-k filter that, for transmission, only lets through the modes supported by the plate. Coupling between plates A and B is stronger when modes overlap in the f-k spectra between the two plates. However, more than one factor can change the characteristics of the f-k filters. **1)** Varying the plate thickness is the direct method, as the dispersion relations are modified. **2)** The second method is to tilt the plate. The f-k filter is unaffected, but the input spectrum is shifted. This could happen multiple times if the wave is "trapped" between the two plates, changing its incidence angle every time it bounces back and forth, until it eventually couples to a mode of one plate. **3)** Increased mode attenuation is a third option, as it broadens the "acceptance bands" of the plate mode.

One shorter example is given before tackling the heavy cement case: Why is light cement easy to detect when the plates are parallel and equally thick? When plate A is excited by p_{in}, wave packets of primarily A_0 and S_0 modes start propagating, both

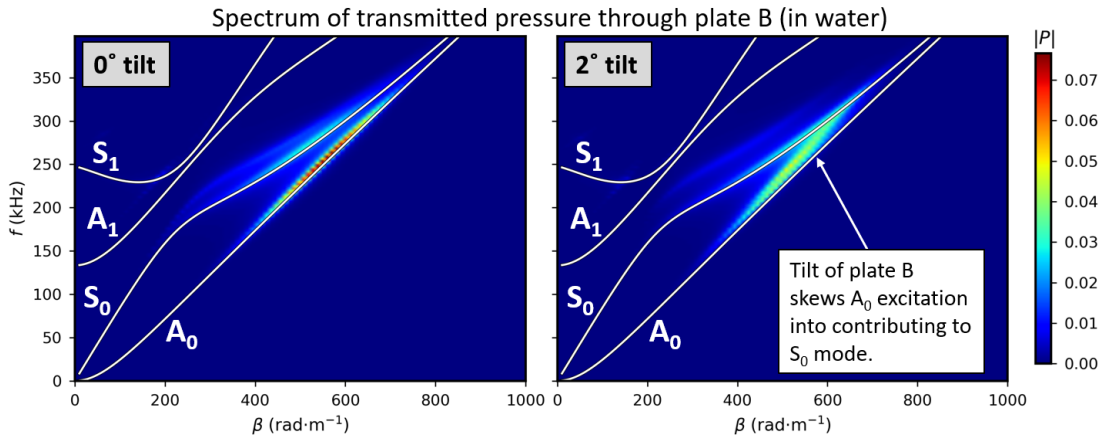

Fig. 4.12. The spectrum of transmitted pressure through plate B, $T_B \cdot \measuredangle_\theta(S \cdot T_A \cdot P_{in})$, for two different tilt angles of plate B, having a thickness of 1.2 cm. The pressure incident on plate B comes from propagating modes in plate A, which has a thickness of 1 cm. The modal lines are given for plate B.

containing a spectrum of frequencies. If the plates are equally thick and parallel, the wavefronts emitted from plate A have the same optimal angle as the modes in plate B, giving an efficient coupling, and new wavepackets are set up in plate B. Looking at the attenuation curves for a plate in water at around 250 kHz, Fig. 2.9, and compare with a plate in contact with light cement on one side, Fig. 2.10, we see that the attenuation is roughly twice as strong in the light cement case. Therefore, the re-emitted wavefronts from plate B will be much more attenuated in the cement case, and the difference will be quite easily detected.

However, if the second material is heavy cement, the A_0 attenuation is from Fig. 2.11 roughly 5 Np/m, which is comparable to that of water. The S_0 attenuation is, on the other hand, significantly higher. So what happens when plate B is thicker and the tilt angle is positive?

The optimal angle from Snell's law of the S_0 mode increases as the plate thickness goes up (approximately as $\phi_c \approx 2 + 30d_B$ around $d_B = 1\,\text{cm}$), whereas the angle for A_0 goes down ($\phi_c \approx 37.5 - 5d_B$). On the other hand, the positive tilt makes the emitted wavefront from plate A hit plate B at a reduced angle and vice versa. Taking a look at Fig. 3.3 is advised in order to follow the reasoning in the next paragraph.

From plate A, the A_0 wavefront is emitted at roughly 32 degrees, keeping in mind there is, in fact, a spectrum of plane waves around that angle. When the second plate B is tilted by 2 degrees, the wavefront hits plate B with an incidence angle of about 30 degrees. Now, because plate B is thicker than plate A, the optimal angle for S_0 is increased from about 22 degrees to 26 degrees. Therefore, the tilt and increased thickness cooperate to increase the coupling and mode conversion between A_0 in plate A to S_0 in plate B. This is shown in Fig. 4.12. The excited modes in plate B, indicated by the transmitted spectrum, are largely determined by the excitation spectrum. When plate B is tilted, the excitation spectrum from an A_0 mode in plate A is skewed toward the S_0 mode in plate B.

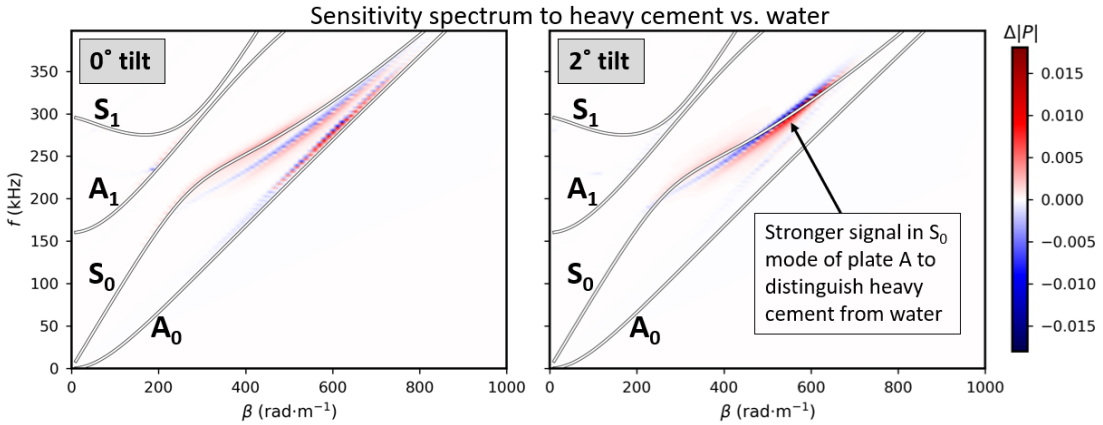

Fig. 4.13. The effect of tilt angle on the difference in the spectrum of the first reflection component, $r_1 = T_A \cdot S \cdot \measuredangle_\theta(R_B \cdot \measuredangle_\theta(S \cdot T_A \cdot P_{in}))$, from having different materials behind plate B, and therefore different R_B. $\Delta|P| = |r_1^{\text{water}}| - |r_1^{\text{h.cem.}}|$. The modal lines are given for plate A.

The S_0 mode experiences significantly increased attenuation if the plate is connected to cement instead of water, which hints to Fig. 2.14. The dip at 22 degrees, corresponding to the S_0 mode, is wider for heavy cement than water, showing that heavy cement broadens the capability of the plate to "accept" plane waves around the S_0 mode. This behavior is similar to how damping in mass-spring systems broadens the resonance peak and is confirmed by the fact that the A_0 mode dip, at 32 degrees, is equally wide for the curves associated with water and heavy cement, which is expected, because the A_0 mode attenuation is the same for the two materials.

Therefore, if plate B is above heavy cement, the S_0 mode is effectively absorbed. However, if the material behind plate B is water, the excited S_0 mode can propagate longer. The emitted wavefront of the propagated S_0 mode in plate B hits plate A with an incidence angle of about 24 degrees, close to the optimal angle for S_0 transmission, allowing for detection. Fig. 4.13 shows the difference in spectrum between heavy cement and water for two different tilts of plate B. If there is a tilt, the detected difference is clearly in the S_0 mode, in line with the explained mechanism.

Therefore, in the pitch-catch technique for double casings, tuning for specific modes other than A_0 may open up new possibilities to detecting the material behind the second casing.

4.2.3 Inversion results

Inversion is attempted on a COMSOL simulation of the same example discussed in the previous section, with two slightly tilted plates and the aim of detecting the presence or absence of heavy cement. The purpose is to show that inversion can work in principle for non-parallel plates and verify the forward model developed. The setup is *not* identical to the setup in the sensitivity analysis because the need to run a COMSOL simulation made the domain smaller.

The plate thicknesses d_A and d_B are assumed to be known, and the ranges of spacing

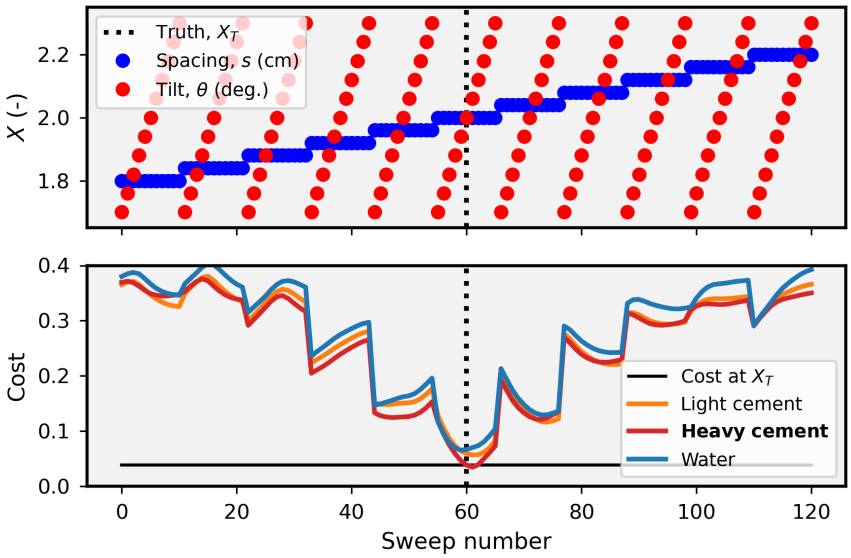

Fig. 4.14. Brute force inversion to find heavy cement behind plate B. The ranges of possible tilt and spacing are discretized in 11 steps. $d_A = 1$ cm, $d_B = 1.15$ cm.

s and tilt θ are discretized in 11 steps. The three predefined materials heavy cement, light cement, and water are calculated for each combination of s and θ, giving 363 permutations to compare. The mrNSR cost function is used together with the method of simplified point receivers at 10 cm and 17 cm along with the plate.

The first result is shown in Fig. 4.14, where the true material behind the second plate is heavy cement. The lowest cost is associated with heavy cement, meaning that the inversion is successful. The true parameters X_T consists of the tilt of 2° and the separation distance of 2 cm, both alternatives in the discretized range of parameters. The cost does not quite reach 0, but rather 0.038 at the X_T because of slight differences between COMSOL and the forward model. The differences are shown in Fig. 4.15 along with the signals at the two simplified receivers in COMSOL. That shows that a cost of 0.038 already indicates a good match.

The cost is slightly higher when comparing COMSOL measurements with a forward model calculated with water as the material behind the second plate. In that case the cost is 0.067, also shown in Fig. 4.15. The second receiver at $x = 17$ cm seems to contribute more to the cost than the receiver at $x = 10$ cm, which suggests that the domain of 20 cm is smaller than ideal. The same is suggested in Fig. 4.11, which shows the difference in cost to be higher when using more receivers at distances of 30 cm and further away from the source.

The problem indicated by Fig. 4.14 is that the cost is very sensitive to, e.g., the wrong spacing s. While the cost is low when $s = 2$ cm, it increases by almost 0.1 by altering s from 2 cm to 2 ± 0.04 cm. One could always increase the resolution of the inversion parameters adaptively, but if, for instance, d_B is not exactly given, the effect on the cost should be known.

Therefore, the inversion is rerun with water as the actual material. The relevant

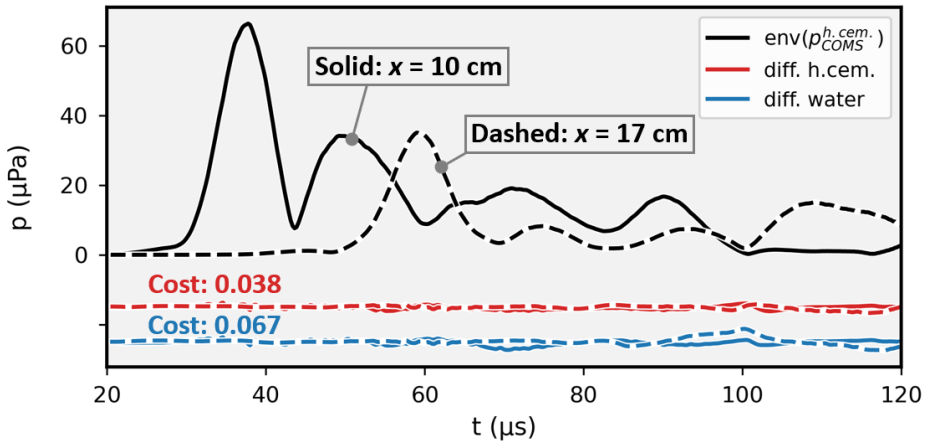

Fig. 4.15. The black curves, env($p^{h.cem}_{COMS}$) shows the receiver envelopes in COMSOL with heavy cement as the material. The receiver positions at $x = 10$ cm and 17 cm are plotted with solid and dashed lines respectively. The forward model is computed with heavy cement or water as the material, and the difference from COMSOL in the envelopes is shown in the red and blue curves. The differences are used to generate the mrNSR cost.

parts of the cost curves are shown in Fig. 4.16. Again, if the d_A and d_B are given precisely, there is unambiguously water that gives the best match. However, if a 1% error is introduced into both parameters, the lowest cost is found at a somewhat smaller spacing s, and the cost difference between water and heavy cement is reduced. Water is still indicated as the correct material but by a very narrow margin. It has been verified that the 1% error in d_A contributes significantly more to the cost than the 1% error in d_B, which is natural since most of the energy is localized in the r_0 reflection component that only depends on plate A. On the other hand, plate A can be measured directly and controlled with pulse-echo [15].

4.2.4 The case for and against practical inversion

The case against inversion

1. If the inversion includes parameters like the distance s between the plates or the tilt angle θ, the search is like finding the needle in a haystack. Fig. 4.10 shows quite clearly that, at least when using mrNSR, the cost has a notch-like minimum that is hard to find, and unless one is close to the true value, there seem to be very little information in the gradient to guide the search.

2. The material behind the outer plate B, which is the most interesting to know, is also the hardest to find in the search. Fig. 4.11 even suggests that there are configurations where it is impossible to find the material from inversion, at least around frequencies that only excite the A_0 and S_0 modes.

3. In actual wells, there are physical features that have not been implemented in the model. That includes potential roughness of some surfaces, the curvature of the

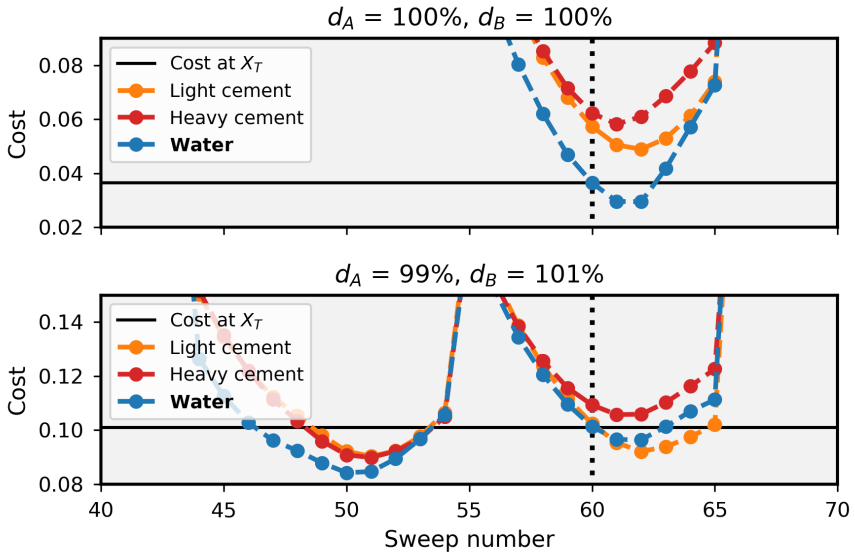

Fig. 4.16. Brute force inversion to find water behind plate B. The ranges of possible tilt and spacing are discretized in 11 steps. $d_A = 1$ cm, $d_B = 1.15$ cm, but an error of 1% is introduced to both parameters in the forward model.

casings, and local cement defects [59].

The case for inversion

1. The geometrical parameters such as casing thicknesses d_A and d_B, spacing s, and eccentricity may be found more easily from other methods such as pulse-echo, or are already known from the time of drilling and installment. Inversion also runs in series, and when the inversion has already been run on one segment of the well, it will most likely give much information about the next segment. Therefore, it may be possible to converge more rapidly to the near-exact geometry and reach cost levels where one expects to get at least somewhat reliable information about the material.

2. There are great opportunities to make the computations run faster and do the computations in parallel. However, a technique to consider in combination is pre-computing many possible combinations of parameters and storing them as a lookup table (LUT). The amount of data to store for each receiver and simulation is relatively tiny.

3. Normally, only a few classes of material are of interest. Because the inversion is not very sensitive to variations in the material parameters, separating between water and a known type of cement may be enough in many situations.

4. There are reasonable indications that the system's geometry can be found from existing logs or inversion. Then, even if the materials cannot be decided from inversion in all geometrical configurations of the system, those cases can be identified

with the technique used to generate Fig. 4.11.

5. The inversion was tested with two receivers within a 17 cm distance from the excitation. More receivers and longer distances may improve the inversion capabilities and robustness. Also, optimizing the excitation to exploit more modes than A_0 may open up new possibilities, as discussed.

6. Other cost functions than the proposed mrNSR may be attempted. mrNSR ignores some of the phase information and also displays a notch-like behavior in the parameters associated with geometry. Experimenting with, for instance, cost functions feature-engineered for the problem may give better inversion capabilities, but it is not immediately clear how such a cost function should be defined.

4.3 Additional topics

4.3.1 Three-dimensional simulations

The code for two-dimensional propagation has been modified to cover the three spatial dimensions plus time. The intention is to show the qualitative behavior of wave propagation. Verification against COMSOL has not been possible because the computational requirements for a basic FEM simulation of the problem exceeded the capacity of the hardware available.

The result of the three-dimensional simulation is shown in Fig. 4.17, with a tilt of plate B of 5° as if the two casings are eccentric but parallel along the main propagation axis. Notice that the y-axis is stretched, and the similarity with the two-dimensional COMSOL simulation in Fig. 4.6.

The tilt of 5° can be seen to send the later wavepackets drifting towards one side, which is more easily seen in Fig. 4.18. Therefore, it might make sense to place additional transducers off-axis if casing eccentricity is a parameter in the inversion.

4.3.2 Comments on execution time

The code is written entirely in Python 3.6.5, leveraging Numpy 1.19.2 and Scipy 1.3.1. The hardware available for all computations, including COMSOL, was 8 GB of RAM, and an Intel i5-7200U processor, clocking at 2.50 GHz. While vectorization and broadcasting have been used where possible, the code has not been profiled or optimized at large. The exception is for the tilting function and calculation of T and R coefficients, where Numba 0.46.0 has been used for compiling code with the `@numba.njit` decorator in some functions, marked in Appendix A.

COMSOL execution time

The COMSOL simulation of the two-plate setup displayed in Fig. 3.2 was timed, taking 1 hour and 53 minutes. The plates simulated have a length of 20 cm, and the maximum time in the simulation is 134 µs.

The execution time of a full three-dimensional simulation could not be assessed. However, a simulation of a single plate in three dimensions in a vacuum was performed in relation to [8], which can be seen in Fig. 15 in Appendix B. Because only antisymmetric

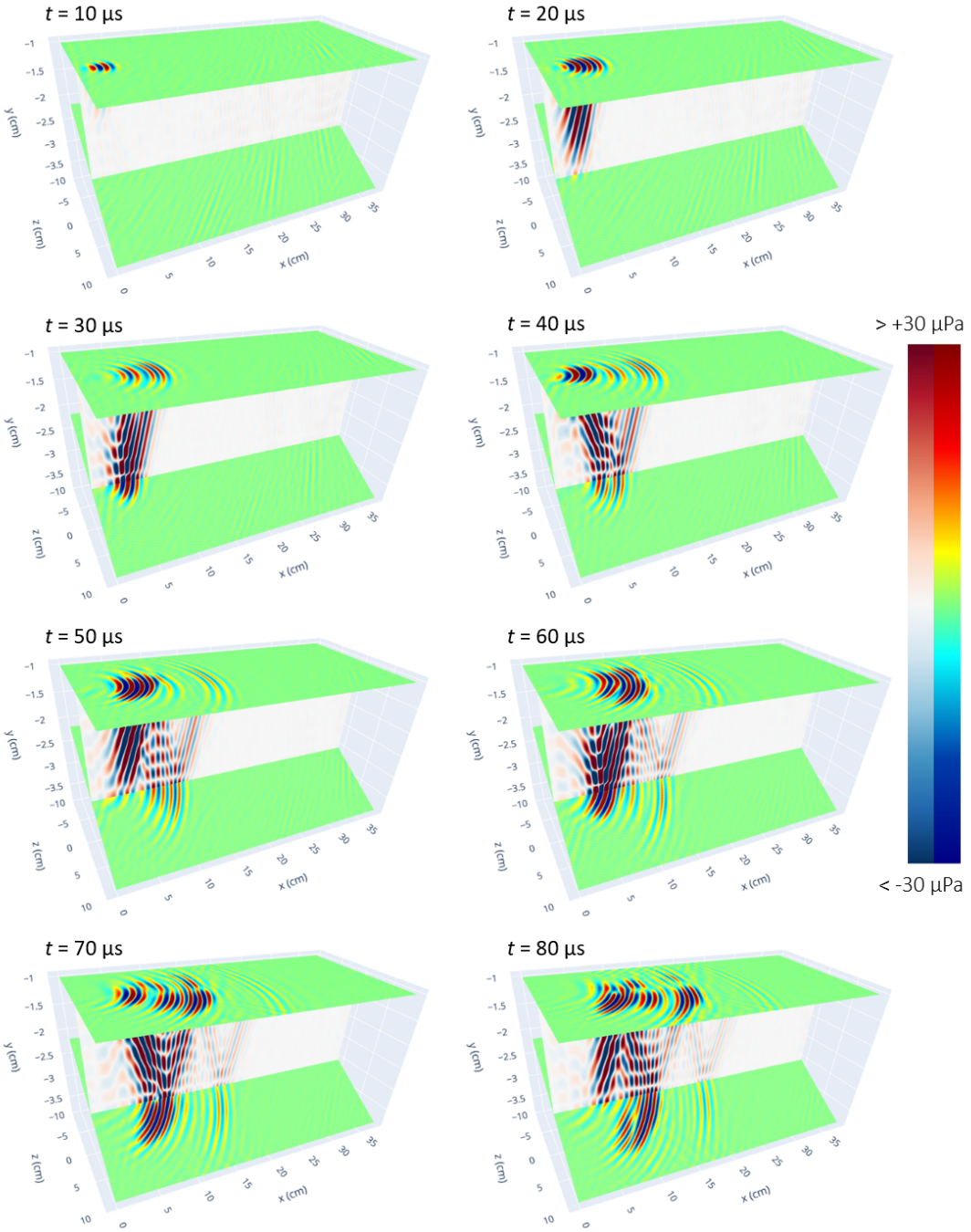

Fig. 4.17. Snapshots of three-dimensional propagation of Lamb waves between coupled and tilted plates. The upper surface represents the pressure on the underside of plate A. Note that especially the y-axis is significantly scaled up and that the tilt angle is, in reality, 5 degrees. The full simulation domains are shown, so the periodic boundaries in the z-direction become evident.

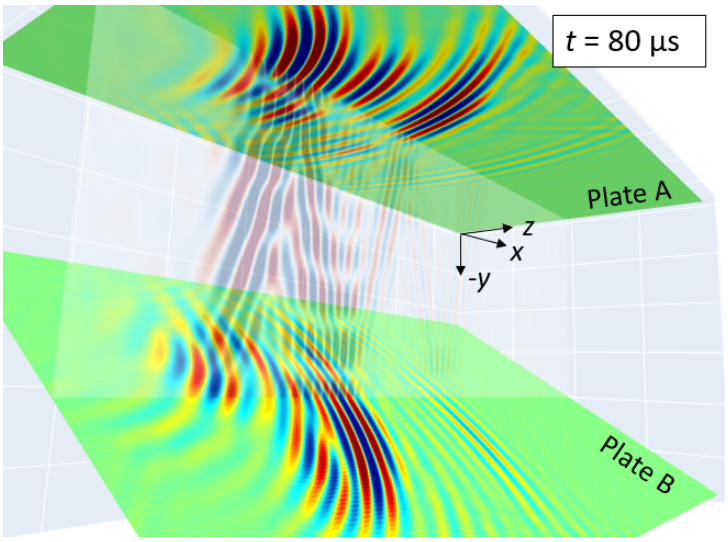

Fig. 4.18. A closer view of the last snapshot in Fig. 4.17.

Lamb waves were of interest, two planes of symmetry were used, together with an increased mesh size, and the simulation took roughly 12 hours to finish on a more powerful computer. For general three-dimensional simulations, including two plates, thick fluid layers, and no planes of symmetry, the simulation would probably require weeks to run.

Two-dimensional execution time

Because the simulation method developed in this work is implemented in the frequency domain, aliasing effects must be addressed. Therefore, the simulation domains must, at least for smaller domains where the aliasing is noticeable, be somewhat larger than the domain of interest to make a fair comparison with COMSOL. Also, the algorithm's execution time depends on the number of reflection components computed (excluding r_0). For the applications in mind, 2-5 components are reasonable.

Using what has been the standard domain size with x_{max} of roughly 60 cm, and t_{max} 400 µs, the shape of the multi-dimensional array is (512×512). As a reminder, the method inherently computes the solution at all time-steps and positions. Four reflection components are chosen (r_0 to r_4), and the execution time was averaged over seven attempts and found to be 602 ms, which is about 11,300 times faster than COMSOL. With two reflections, also sufficient in some applications, it took 547 ms.

For twice the domain size, x_{max} of about 120 cm, and t_{max} 800 µs, the shape is (1024×1024), and computing four reflections took 2.48 s. For comparison, using the same domain as in COMSOL, x_{max} of roughly 20 cm and t_{max} of 134 µs, the shape of the multi-dimensional array is (168×168), and 4 reflections took 59.2 ms to compute, but suffers from aliasing.

Three-dimensional execution time

Various parts of the three-dimensional simulation has been timed as well. Here, t_{max} is 256 µs, x_{max} is 37 cm, and z runs from −9 to 9 cm, giving an effective z_{max} of 18 cm. The multi-dimensional array has the shape (256×256×128).

Computing the multidimensional FFT took roughly 450 ms. In total, computing all R and T coefficients took 5.5 seconds: Supersampling β by 10 times (which is likely more than needed) was timed to 2.3 s, plus interpolation into the (256×256×128) block taking about 3.2 s. Each multiplication of multi-dimensional arrays was timed to 70 ms.

The biggest bottleneck was initially the tilting operation, and two tilts are needed for each reflection component. After rewriting the interpolation method, the code was sped up from 4.2 s per tilt, to 125 ms per tilt. Computing 4 reflection components was finally timed to 4.3 s, with the final IFFT and array-shifting taking about 700 ms. In total, the example takes about 12 s to compute from start to finish.

Suggestions for further speedups

As usual for optimizing code, the best strategy is to profile and optimize the slowest parts. That was only done to speed up the computation of R and T coefficients using Numba and the tilting operation by tweaking the algorithm and using Numba. With only small efforts put into optimization so far, there are likely to be more low-hanging fruits to speed up the code further.

For the specific case of simulating a pitch-catch setup, only positive frequencies and wavenumbers in the x-direction contribute to the result, and one could tailor the algorithm, for instance, by ignoring the negative frequencies. Also, because the excitation is band-limited, one could skip any calculation related to frequencies that carry little energy.

Using faster Fourier transforms is also possible, e.g., by employing the pyFFTW library that plans the best way to perform FFTs in advance. Parallelization is also a viable option, either on CPUs or GPUs. The ease of implementation may vary, but most of the code, and the inversion, seem to be so-called “embarrassingly parallelizable”. The option of using better hardware should not be necessary to address, but since all simulations have been run on a laptop with a low-power CPU from 2016, the performance should improve substantially by switching to dedicated hardware.

Chapter 5

Conclusion

5.1 Extended summary

A fast and accurate method has been developed for simulating ultrasonic wave propagation in coupled, non-parallel plates. The method is based on response methods, where reflection and transmission coefficients for each plane wave component of an ultrasonic pulse are calculated for the individual plates, which allows the plates to be in contact with any layered structure of materials. The propagation between the plates, and their relative tilt, is made possible using an angular spectrum approach combined with a coordinate rotation method in the wave vector domain. The coordinate rotation method, initially developed for optical diffraction, has to our knowledge not been applied in the field of acoustics before.

The method's deviation from equivalent COMSOL simulations is dominated by the deviation in the excitation pressure on the plates, created by the simplified transducer model, with a relative amplitude difference of about 2%. The other most significant source of error comes from aliasing, or wrap-around effects, which can be made negligible by increasing the simulation domain size. Numerical dispersion in COMSOL may also contribute to the measured deviation.

The execution time of the method is significantly faster than equivalent COMSOL simulations. Depending on choices related to the domain size and the number of reflection components, the two-dimensional simulations run roughly 11,000 times faster than in COMSOL, taking a few seconds in most cases. The three-dimensional simulations could not be compared with COMSOL, but an example featuring two 37×18 cm^2 plates took about 12 seconds to compute, and computational times within a couple of minutes seem reasonable in most scenarios.

The method was employed as a forward model in through-tubing well logging, where the material behind the outer plate was to be found from inversion. First, a parametric sweep study was performed to identify the sensitivity to different materials in the inversion under different setup geometries. From the results, an argument based on modal theory has been given, arguing that some materials are easier to detect by tuning for other modes than the A_0 Lamb mode, which is standard in pitch-catch setups for single plates. The mechanism discussed is in part based on mode conversion between tilted plates, from A_0 to S_0 Lamb waves, and the fact that specific modes, such as the S_0 Lamb wave, is more attenuated by "faster" materials, such as heavy cement, behind the

second plate, in turn giving better contrast from a fluid.

A simplified inversion procedure was then used to retrieve the material and geometry from a COMSOL reference simulation. The aim was to demonstrate the principle and possibility to perform inversion with tilted plates and heavy cement, and the inversion successfully identified the material behind the outer plate. As expected, the cost function was susceptible to errors in the parameters related to the geometry, such as plate thickness, and less sensitive to the material. The observation may have been made worse by performing the inversion on a miniaturized plate setup of 20 cm, but it nonetheless hints towards some challenges that must be investigated for practical inversion.

5.2 Suggestions for further work

The results presented give hope that the simulation method can serve as a forward model for inversion in practical well logging. Further investigation into the challenges and possibilities that arise in practical well logging has been outside the scope of this thesis but is needed to address the next steps. A question to look into is what kind of data is available from other techniques and existing logs, and at what level of accuracy, as that will influence what inversion strategy is reasonable to pursue.

The mrNSR cost function may also be addressed. While it has worked, it displays a notch-like behavior in some variables, making gradient-based searches in the cost space difficult. The mrNSR is, however, entirely general and assumes nothing about the underlying physics. Thus, a possibility for further work is to look for more feature-engineered and physics-motivated cost functions or techniques. That may open up for extracting some parameters, like the tilt angle, more directly than by blindly performing inversion on it.

A realistic pitch-catch setup is somewhat different from the idealized model presented. The receivers were modeled as point-like hydrophones on the top of the plate. Because real transducers have a size and orientation, they may act as a filter on some plane wave components due to the transducer directivity function. That is something to have in mind when investigating how, and if, mode conversion between tilted plates, from, e.g., A_0 to S_0 modes, may be exploited to increase detection capability and contrast between certain materials.

Other differences that have not been included in the computational model include the curvature of real casings and how small local defects can be modeled. However, the effect of casing eccentricity in three dimensions is the most important to investigate, as it is thought to be more commonly occurring than non-parallel casings. It is not known how it behaves as an inversion parameter and should therefore be studied further. As shown in Fig. 4.17, the later wavepackets tend to drift towards the tilt direction, suggesting that placing receiver transducers off the propagation axis may open up new possibilities in performing inversion, which would suggest developing a new tool geometry.

Depending on the needs in practical inversion, the need to effectively test many sets of candidate model parameters may be huge. Ways of speeding up the code further have been suggested, and using lookup tables is also promising. Perhaps of more academic interest, a third candidate option is to develop a filter against the wrap-around effect. Because the excitation zone is known, the modes that propagate may be estimated and eventually removed when they wrap around and re-emerge at a space or time incom-

patible with the known excitation. The modal characteristics may be pre-computed or estimated, but the filter may not be computationally feasible, as it needs to estimate the contribution of the modes quite accurately.

5.3 List of achieved results

In this thesis, and work leading up to it, the following has been achieved:

- An efficient method for simulating wave propagation between coupled, non-parallel plates in two and three dimensions. The method features a novel application for the coordinate rotation method by Matsushima et al. [51].
- A proof of concept that the computational model may, at least some in scenarios, serve as a forward model in through-tubing well logging. The forward model may otherwise be used to identify the situations where inversion is not possible and alternative techniques for making inversion more robust.
- An understanding that tilted plates give rise to a mechanism for Lamb mode conversion and that this conversion may help detect certain kinds of materials behind the second plate.
- A direct comparison between modal methods (NME) and response methods for simulating transient wave propagation in single plates.
- The first implementation and detailed description, to our knowledge, of the power flow method used to calculate the attenuation of leaky Lamb waves due to contact with solid media.
- A fast method for propagating the leaky wavefields of initialized Lamb waves (Appendix B).
- An extended abstract (Appendix C), providing a better understanding of how subsonic radiation is possible, with particular relevance for the A_0 Lamb mode.
- Code that will be made available for those with interest in simulating Lamb waves.

Bibliography

[1] Standard Norge, "NORSOK D-010 well integrity in drilling and well operations rev. 4," 2013.

[2] L. Sørum, "Tiden er inne for et nytt eventyr på norsk sokkel." `www.sintef.no/siste-nytt/tiden-er-inne-for-et-nytt-eventyr-pa-norsk-sokkel/`, 22.04.2020. Online; accessed 12.12.2020. Norwegian.

[3] E. M. Viggen, T. F. Johansen, and I.-A. Merciu, "Simulation and modeling of ultrasonic pitch-catch through-tubing logging," *Geophysics*, vol. 81, no. 4, pp. D383–D393, 2016.

[4] E. M. Viggen, T. F. Johansen, and I.-A. Merciu, "Simulation and inversion of ultrasonic pitch-catch through-tubing well logging with an array of receivers," *NDT & E International*, vol. 85, pp. 72 – 75, 2017.

[5] S. Zeroug and B. Froelich, "Ultrasonic leaky-lamb wave imaging through a highly contrasting layer," in *IEEE Symposium on Ultrasonics, 2003*, vol. 1, pp. 794–798 Vol.1, 2003.

[6] A. Talberg, "Experimental evaluation of broadband wave propagation in plates," Master's thesis, Norwegian University of Science and Technology, 2016.

[7] P. Wilcox, *Lamb Wave Inspection of Large Structures Using Lamb Wave Inspection of Large Structures Using Permanently Attached Transducers*. PhD thesis, 1998. Examining body: Department of Mechanical Engineering, Imperial College.

[8] H. K. Arnestad and E. M. Viggen, "A fast semi-analytical method for propagating leaky Lamb wavefields," in *Proceedings of the 44th Scandinavian Symposium on Physical Acoustics*, p. 22, Norwegian Physical Society, 2021.

[9] P. Kauffmann, M.-A. Ploix, J.-F. Chaix, C. Potel, C. Gueudre, G. Corneloup, and F. Baque, "Multi-modal leaky Lamb waves in two parallel and immersed plates: Theoretical considerations, simulations, and measurements," *The Journal of the Acoustical Society of America*, vol. 145, no. 2, pp. 1018–1030, 2019.

[10] P. Kauffmann, M.-A. Ploix, J.-F. Chaix, C. Gueudré, G. Corneloup, and F. Baqué, "Non-destructive testing of nuclear structures behind screen using leaky lamb waves," *AIP Conference Proceedings*, vol. 2102, no. 1, 2019.

[11] S. Zeroug, S. Bose, B. Sinha, M. Skataric, Y. Liu, and R. D'Angelo, "Sonic and ultrasonic measurement applications for cased oil wells," *Insight - Non-Destructive Testing and Condition Monitoring*, vol. 58, pp. 423–430, 2016.

[12] G. H. Pardue and R. Morris, "Cement bond log - a study of cement and casing variables," *Journal of Petroleum Technology*, vol. 15, pp. 545–555, 1963.

[13] H. Wang, G. Tao, and X. Shang, "Understanding acoustic methods for cement bond logging," *The Journal of the Acoustical Society of America*, vol. 139, no. 5, pp. 2407–2416, 2016.

[14] *Making Sense of Why Sometimes Logs Do Not See Cement in the Annulus*, vol. April 26, 2017 of *SPE Western Regional Meeting*, 04 2017.

[15] A. J. Hayman, R. Hutin, and P. Wright, "High-resolution cementation and corrosion imaging by ultrasound," Presented at the SPWLA 32nd Annual Logging Symposium, 1991.

[16] R. van Kuijk, S. Zeroug, B. Froelich, M. Allouche, S. Bose, D. Miller, J.-L. le Calvez, V. Schoepf, and A. Pagnin, "A novel ultrasonic cased-hole imager for enhanced cement evaluation," Presented at the International Petroleum Technology Conference, 2005.

[17] M. J. S. Lowe, "Matrix techniques for modeling ultrasonic waves in multilayered media," *IEEE Transactions on Ultrasonics, Ferroelectrics, and Frequency Control*, vol. 42, no. 4, pp. 525–542, 1995.

[18] J. Hovem, *Marine Acoustics: The Physics of Sound in Underwater Environments*. Peninsula Publishing, 2012.

[19] S. Zeroug, "Forward modeling for ultrasonic leaky Lamb-wave based imaging through a highly contrasting steel cylindrical layer," in *IEEE Ultrasonics Symposium, 2004*, vol. 1, pp. 672–675 Vol.1, 2004.

[20] E. W. Weisstein, "Gaussian Function, From MathWorld – A Wolfram Web Resource." `mathworld.wolfram.com/GaussianFunction.html`. Online; accessed 10.06.2021.

[21] M. Schwartz, "The physics of waves, lecture 11: Wavepackets and dispersion." Physics 15c, lecture notes, Harvard University, 2016.

[22] A. Bernard, M. J. S. Lowe, and M. Deschamps, "Guided waves energy velocity in absorbing and non-absorbing plates," *The Journal of the Acoustical Society of America*, vol. 110, pp. 186–196, July 2001.

[23] S. Garrett, *Understanding Acoustics: An Experimentalists View of Acoustics and Vibration*. Graduate Texts in Physics, Springer International Publishing, 2017.

[24] N. Declercq, R. Briers, J. Degrieck, and O. Leroy, "The history and properties of ultrasonic inhomogeneous waves," *IEEE transactions on ultrasonics, ferroelectrics, and frequency control*, vol. 52, pp. 776–91, 2005.

[25] E. M. Viggen and H. K. Arnestad, "Understanding sound radiation from surface vibrations moving at subsonic speeds," in *Proceedings of the 44th Scandinavian Symposium on Physical Acoustics*, p. 4, Norwegian Physical Society, 2021. Extended abstract.

[26] L. E. Kinsler, A. R. Frey, A. B. Coppens, and J. Sanders, *Fundamentals of Acoustics*. Wiley, 2000.

[27] H. Lamb, "On waves in an elastic plate," *Proc. R. Soc. Lond. A*, vol. 93, no. 648, pp. 114–128, 1917.

[28] I. A. Viktorov, *Rayleigh and Lamb Waves*. Plenum Press, 1967.

[29] J. L. Rose, *Ultrasonic Guided Waves in Solid Media*. Cambridge University Press, 2014.

[30] B. A. Auld, *Acoustic Fields and Waves in Solids*, vol. I of *Acoustic Fields and Waves in Solids*. R.E. Krieger, 2nd ed., 1990.

[31] B. A. Auld, *Acoustic Fields and Waves in Solids*, vol. II of *Acoustic Fields and Waves in Solids*. Krieger Publishing Company, 2nd ed., 1990.

[32] W. Ostachowicz, P. Kudela, M. Krawczuk, and A. Zak, *Guided Waves in Structures for SHM: The Time-domain Spectral Element Method*. Wiley, 2012.

[33] K. Luangvilai, *Attenuation of ultrasonic Lamb waves with applications to material characterization and condition monitoring*. PhD thesis, Georgia Institute of Technology, 2007.

[34] A. Schoch, "Der schalldurchgang durch platten," *Acustica*, vol. 2, pp. 1–17, 1952.

[35] L. G. Merkulov, "Damping of normal modes in a plate immersed in a liquid," *Soviet Physics-Acoustics*, vol. 10, no. 2, pp. 169–173, 1964.

[36] D. A. Kiefer, M. Ponschab, S. J. Rupitsch, and M. Mayle, "Calculating the full leaky Lamb wave spectrum with exact fluid interaction," *The Journal of the Acoustical Society of America*, vol. 145, no. 6, pp. 3341–3350, 2019.

[37] D. Kiefer, M. Ponschab, and S. Rupitsch, "From Lamb waves to quasi-guided waves: On the wave field and radiation of elastic and viscoelastic plates." preprint, doi: 10.13140/RG.2.2.32631.44968, 2020.

[38] A. Freedman, "Anomalies of the A_0 leaky Lamb mode of a fluid-loaded, elastic plate," *Journal of Sound and Vibration*, vol. 183, no. 4, pp. 719 – 737, 1995.

[39] X. L. Bao, H. Franklin, P. K. Raju, and H. Überall, "The splitting of dispersion curves for plates fluid-loaded on both sides," *The Journal of the Acoustical Society of America*, vol. 102, no. 2, pp. 1246–1248, 1997.

[40] H. Dabirikhah and C. W. Turner, "The coupling of the A_0 and interface Scholte modes in fluidloaded plates," *The Journal of the Acoustical Society of America*, vol. 100, no. 5, pp. 3442–3445, 1996.

[41] V. Dayal and V. K. Kinra, "Leaky Lamb waves in an anisotropic plate. I: An exact solution and experiments," *The Journal of the Acoustical Society of America*, vol. 85, no. 6, pp. 2268–2276, 1989.

[42] R. D. Watkins, W. H. B. Cooper, A. B. Gillespie, and R. B. Pike, "The attenuation of Lamb waves in the presence of a fluid," *Ultrasonics*, vol. 20, no. 6, pp. 257 – 264, 1982.

[43] G. Williams, *Fourier Acoustics: Sound Radiation and Nearfield Acoustical Holography*. Elsevier Science, 1999.

[44] L. Yu and Z. Tian, "Case study of guided wave propagation in a one-side water-immersed steel plate," *Case Studies in Nondestructive Testing and Evaluation*, vol. 3, pp. 1–8, 2015.

[45] J. Achenbach, *Wave Propagation in Elastic Solids*. ISSN, Elsevier Science, 2012.

[46] J. Miklowitz, *The Theory of Elastic Waves and Waveguides*. Applied mathematics and mechanics, North Holland Publishing Company, 1978.

[47] J.-L. Akian, "A proof of the completeness of Lamb modes." preprint, doi: 10.22541/au.161771284.45509849/v1, 03 2021.

[48] A. M. Kamal, B. Lin, and V. Giurgiutiu, "Exact analytical modeling of power and energy for multimode Lamb waves excited by piezoelectric wafer active sensors," *Journal of Intelligent Material Systems and Structures*, vol. 25, no. 4, pp. 452–471, 2014.

[49] X. Jia, "Modal analysis of Lamb wave generation in elastic plates by liquid wedge transducers," *The Journal of the Acoustical Society of America*, vol. 101, pp. 834–842, Feb. 1997.

[50] A. Zangwill, *Modern Electrodynamics*. Cambridge University Press, 2012.

[51] K. Matsushima, H. Schimmel, and F. Wyrowski, "Fast calculation method for optical diffraction on tilted planes by use of the angular spectrum of plane waves," *J. Opt. Soc. Am. A*, vol. 20, p. 1755, Sept. 2003.

[52] A. Nayfeh and D. E. Chimenti, "Ultrasonic wave reflection from liquid-coupled orthotropic plates with application to fibrous composites," *Journal of Applied Mechanics*, vol. 55, pp. 863–870, 1988.

[53] D. E. Chimenti and S. I. Rokhlin, "Relationship between leaky Lamb modes and reflection coefficient zeroes for a fluidcoupled elastic layer," *The Journal of the Acoustical Society of America*, vol. 88, no. 3, pp. 1603–1611, 1990.

[54] C. Klieber, T. Brill, S. Catheline, Y. Vincensini, and F. Mege, "Visualization of Leaky Ultrasonic Lamb Wave Experiments in Multilayer Structures," *Physics Procedia*, vol. 70, pp. 314–317, 2015.

[55] R. Aster, B. Borchers, and C. Thurber, *Parameter Estimation and Inverse Problems*. Elsevier Science, 2013.

[56] N. Chapman and C. Lindsay, "Matched-field inversion for geoacoustic model parameters in shallow water," *IEEE Journal of Oceanic Engineering*, vol. 21, no. 4, pp. 347–354, 1996.

[57] M. D. Collins, W. A. Kuperman, and H. Schmidt, "Nonlinear inversion for oceanbottom properties," *The Journal of the Acoustical Society of America*, vol. 92, no. 5, pp. 2770–2783, 1992.

[58] P. Hansen, *Discrete Inverse Problems: Insight and Algorithms*. Society for Industrial and Applied Mathematics (SIAM), 2010.

[59] R. Song, H. Dong, and X. Bao, "Numerical study of the effect of cement defects on flexural-wave logging," *Geophysics*, vol. 84, pp. D171–D177, 06 2019.

Appendix A

Code for simulating tilted plates in two dimensions

The following code can be used to simulate two tilted plates in the two-dimensional case using response methods. Numba has been used to speed up certain parts of the code. Questions can be directed to: havard.arnestad@gmail.com

```
import matplotlib.pyplot as plt
import numpy as np
import numba
from numpy.linalg import inv, det
from numpy import fft
from functools import partial
pi, nax = np.pi, np.newaxis


"""
EXAMPLE:
"""

### System parameters
Lx = 0.6 # m - plate length of interest
th0 = 2.0 # degrees - tilt of plate B
s = 2/100 # m - space between plates
da = 1/100 # m - thickness, plate A
db = 1.2/100 # m - thickness, plate B

### Simulation related
fc = 250000 # Hz - center frequency of excitation
pAmp = 1e-3 # Pa - amplitude of initial wave packet

x_max = 0.6 # m - max length in simulation
t_max = 0.4/water.cP # s - maximum simulation time
n_per_wavelength = 5 # n is number samples
n_per_f = 5 # n is number samples


### Create excitation
# Sample domain
x,t = sample_dimensions_const_delta(fc, water.cP, x_max, t_max, samples_per_wavelength =\
                                    n_per_wavelength, samples_per_f = n_per_f, pow2 = True)
```

```
# Likely new x_max and t_max if pow2 = True in previous line.
x_max = x[-1]
t_max = t[-1]

# Create excitation. FWHM = 2, target A0 mode in 1 cm thick steel plate at 250 kHz.
p_in, p_start = make_excitation(pAmp, water, x, t, fc = fc, deg = 32,\
                                width = 2, x0 = 0.02, y0 = 0.02)

# Prepare data and arrays
p_in = fft.fftshift(p_in, axes = 1)
n = int((x_max-Lx)/(2*(x[1]-x[0]))) # samples to roll (align tilt axis)
p_in = np.roll(p_in, n, axis = 1)

### Useful for verification (uncomment):
#plt.pcolormesh(20*np.log10(np.abs(p_in/pAmp)), vmin=-60, vmax=0)

### Final domain and excitation arrays
w  = 2*pi * fft.fftfreq(len(t), t[1]-t[0])
kx = 2*pi * fft.fftfreq(len(x), x[1]-x[0])
P_in_wk = fft.fft2(p_in)

params = {
  "x"   : x,
  "t"   : t,
  "P_in": P_in_wk,
  "n"   : n,
  "w"   : w,
  "kx"  : kx}

### Reflection and transmission from plate A, usually calculated one time
Ra, Ta = R_T_plate(w, kx, water, steel, water, d = da)

### Calculate reflected pressure, array of dimensions (t,x)
p_r  = sim(params, db, s, th0, water, heavy_cement, Ra, Ta)

### Useful for verification
#p_dB = 20*np.log10(np.abs(p_r)/np.max(np.abs(p_r)))
#plt.pcolormesh(x, t, p_dB, cmap = 'jet', vmin = -60, vmax = 0, shading = 'gouraud')


"""
Functions for calculating reflection and transmission coefficients
"""

@numba.njit
def T(gp, gs, y): # Defined in Eq. (2.24)
    T = np.zeros((4,4), dtype = np.complex128)
    T[0,0] = np.exp(1j*gp*y)
    T[1,1] = np.exp(-1j*gp*y)
    T[2,2] = np.exp(1j*gs*y)
    T[3,3] = np.exp(-1j*gs*y)
    return T

@numba.njit
def M(kx, gs, gp, G): # Defined in Eq. (2.23)
    a = G*(kx**2 - gs**2)
```

```
    b = 2*G*kx*gs
    c = 2*G*kx*gp
    d = 1j*gp
    e = 1j*kx
    f = 1j*gs
    M= np.array([[ a,  a, -b,  b],
                 [ c, -c,  a,  a],
                 [ d, -d,  e,  e],
                 [-e, -e,  f, -f]], dtype = np.complex128)
    return M

@numba.njit
def D(y, kx, w, mat_G, mat_cP, mat_cS): # D = M@T
    gp = np.conj(np.sqrt((w / mat_cP)**2 - (kx)**2  + 1e-16 + 0j))
    gs = np.conj(np.sqrt((w / mat_cS)**2 - (kx)**2  + 1e-16 + 0j))
    return M(kx, gs, gp, mat_G)@T(gp, gs, y)

@numba.njit
def L(y, kx, w, mat_G, mat_cP, mat_cS): # Defined in Eq. (2.26)
    return D(-y, kx, w, mat_G, mat_cP, mat_cS) @ inv(D(y, kx, w, mat_G, mat_cP, mat_cS))

@numba.njit
def Tp_Ts_Rp_Rs(w, kx, mid_thickness, top_G, top_cP, top_cS,\
                mid_G, mid_cP, mid_cS, bot_G, bot_cP, bot_cS): # Eq. (2.83)

    N = inv(  D(0, kx, w, bot_G, bot_cP, bot_cS)) \
              @ L(mid_thickness/2, kx, w, mid_G, mid_cP, mid_cS) \
              @ D(0, kx, w, top_G, top_cP, top_cS)

    M = np.array([[1, 0, -N[0,1], -N[0,3]],
                  [0, 0, -N[1,1], -N[1,3]],
                  [0, 1, -N[2,1], -N[2,3]],
                  [0, 0, -N[3,1], -N[3,3]]])
    c =  np.array([N[0,0], N[1,0], N[2,0],N[3,0]])
    return inv(M)@c


@numba.njit
def njit_R_T(w, kx, top_G, top_cP, top_cS, plate_G, \
             plate_cP, plate_cS, bot_G, bot_cP, bot_cS, d):

    Rp = np.zeros((w.shape[0], kx.shape[0]), dtype = np.complex128)
    Tp = np.zeros((w.shape[0], kx.shape[0]), dtype = np.complex128)

    wend = len(w)//2+1
    kend = len(kx)//2+1

    for i in numba.prange(wend):
        for j in numba.prange(kend):
            if abs(w[i])/top_cP <= abs(kx[j]): continue
            if abs(w[i]) < 1000: continue
            Tp[i,j], _, Rp[i,j], _ = Tp_Ts_Rp_Rs(w[i], kx[j], d, top_G, top_cP,\
                                                  top_cS, plate_G, plate_cP, \
                                                  plate_cS, bot_G, bot_cP, bot_cS)

    if len(w)%2==0:
```

```
        Tp[wend:, :] = Tp[wend-2:0:-1, :]
        Rp[wend:, :] = Rp[wend-2:0:-1, :]
    else:
        Tp[wend:, :] = Tp[wend-1:0:-1, :]
        Rp[wend:, :] = Rp[wend-1:0:-1, :]

    if len(kx)%2==0:
        Tp[:, kend:] = Tp[:, kend-2:0:-1]
        Rp[:, kend:] = Rp[:, kend-2:0:-1]
    else:
        Tp[:, kend:] = Tp[:, kend-1:0:-1]
        Rp[:, kend:] = Rp[:, kend-1:0:-1]

    return Rp, Tp

def R_T_plate(w, kx, top, plate, bot, d = 0.01):
    """
    Function to call for calculating T and R, like in Fig. 2.15.
    """
    Rp,Tp = njit_R_T(w, kx, top.G, top.cP, top.cS, plate.G,\
                     plate.cP, plate.cS, bot.G, bot.cP, bot.cS, d)
    Tp[np.isnan(Tp)] = 0
    Rp[np.isnan(Rp)] = 0
    Tp[abs(Tp)>1] = 1
    Rp[abs(Rp)>1] = 1
    return Rp, Tp


"""
Elastic isotropic materials
"""

class ElasticMaterial:
    def __init__(self, **kwargs):
        self.rho = kwargs['rho']
        if ('cP' in kwargs) and ('cS' in kwargs):
            self.cP = kwargs['cP']
            self.cS = kwargs['cS']
            self.G = (self.cS)**2 * self.rho
            self.L = (self.cP)**2 * self.rho - 2*self.G
            self.v = (2*(self.cS/self.cP)**2 - 1) / (2*(self.cS/self.cP)**2 - 2)
            self.E = 2*(1+self.v)*self.G
        elif ('E' in kwargs) and ('v' in kwargs):
            self.E = kwargs['E']
            self.v = kwargs['v']
            self.L = (self.v*self.E)/((1+self.v)*(1-2*self.v))
            self.G = self.E / (2*(1+self.v))
            self.cP = np.sqrt((self.L + 2*self.G)/self.rho)
            self.cS = np.sqrt(self.G/self.rho)
        elif ('G' in kwargs) and ('L' in kwargs):
            self.L = kwargs['L']
            self.G = kwargs['G']
            self.cP = np.sqrt((self.L + 2*self.G)/self.rho)
            self.cS = np.sqrt(self.G/self.rho)
            self.v = (2*(self.cS/self.cP)**2 - 1) / (2*(self.cS/self.cP)**2 - 2)
            self.E = 2*(1+self.v)*self.G
        else:
```

```
            print('Need one of the following pairs: cS,cP / L,G (Lame) / E, v.')

water = ElasticMaterial(rho = 1000, cS = 0.001, cP = 1480)
steel = ElasticMaterial(rho = 7850, cS = 3200, cP = 5900)
light_cement = ElasticMaterial(rho = 1330, cS = 770, cP = 2250)
heavy_cement = ElasticMaterial(rho = 1800, cS = 1850, cP = 3500)


"""
Tilting function
"""
@numba.njit
def Tilt2Dfast(X, deg_tilt, kx, ky, w, cf): # Tilt operation, Eq. (2.82)
    sin = np.sin(deg_tilt * pi/180)
    cos = np.cos(deg_tilt * pi/180)

    max_kx = np.max(kx)
    min_kx = np.min(kx)
    dkx = kx[1]-kx[0]
    kx_bound =  min(abs(min_kx), abs(max_kx - dkx))

    F = np.zeros_like(X)
    for i, wi in enumerate(w):
        if wi < 0: continue # not contributing
        for j, kxj in enumerate(kx):

            if abs(np.real(ky[i,j])) <= 0.1: continue # near evanescent

            kx_to_interpolate = kxj*cos - np.real(ky[i,j])*sin
            index_to_interpolate = (kx_to_interpolate-min_kx)/dkx

            if abs(kx_to_interpolate) > kx_bound: continue # outside array

            index_min = int(index_to_interpolate)
            weight_max = index_to_interpolate - index_min
            weight_min = 1 - weight_max
            A_new = X[i,index_min]*weight_min + X[i,index_min + 1]*weight_max

            F[i,j] = A_new * np.abs( cos + kxj/(ky[i,j] + 1e-15)*sin)
    return F


"""
Functions to sample domain and making excitation signal
"""

def sample_dimensions_const_delta(fc, c_min, x_max, t_max, samples_per_wavelength = 5,\
                                  samples_per_f = 5, pow2 = True):
    """
    Finds dt and dx, then discretizes t and x.
    Increases t_max and x_max if number of samples (in powers of 2) allow it.
    """
    wavelength = c_min / fc
    dx = wavelength / samples_per_wavelength
    n_x = int(x_max / dx)

    if pow2 == True:
```

```
        n_x = int(2**(np.ceil(np.log2(n_x))))
        x_max = dx*n_x
    x = np.linspace(0, x_max, n_x, endpoint = False)

    dt = 1/(fc*samples_per_f)
    n_t = int(t_max/dt)

    if pow2 == True:
        n_t = int(2**(np.ceil(np.log2(n_t))))
        t_max = dt*n_t
    t = np.linspace(0, t_max, n_t, endpoint = False)

    return x, t


def make_excitation(pAmplitude, fluid, x, t, fc = 250000, deg = 32, width = 2,\
                    x0 = 0.02, y0 = 0.02, n_len = 10, n_time =2):

    # Plane wave parameters
    wc       = 2*pi*fc
    kc       = wc/fluid.cP
    lambda_c = 2*pi/kc

    pulse_width = width*lambda_c / 2.355

    th = deg*pi/180 # direction
    kc_x = +kc * np.sin(th)
    kc_y = -kc * np.cos(th)

    # Simulation domain & discretization
    dx = x[1] - x[0]
    y = np.copy(x)

    # Crop domain to **significantly** reduce computation time
    # n_len and n_time adjusts size of cropped domain
    crop_len = n_len * 2*width*lambda_c/2.355

    ix = np.where((x > (x0 - crop_len)) & (x < (x0 + crop_len)))
    xcrop = x[ix]
    ycrop = y[ (y >= 0) & (y < (y0 + crop_len)) ]

    crop_t = n_time * (abs(y0/np.cos(th)) + pulse_width )/fluid.cP
    it = np.where(t <= crop_t)
    tcrop = t[it]

    # Calculate initial vertical velocity distribution, spatial and complex Gaussian pulse
    xx,yy = np.meshgrid(xcrop, ycrop, indexing='ij')
    gauss_window = np.exp(-((xx-x0)**2 + (yy-y0)**2) /(2*pulse_width**2) )
    p0 = pAmplitude * gauss_window * np.exp(-1j*(kc_x*(xx-x0) + kc_y*(yy-y0)))

    # Calculate propagation at y=0 from frequency domain representation
    P  =  fft.fft2(p0)
    k_x = 2*pi*fft.fftfreq(len(xcrop), dx)
    k_y = 2*pi*fft.fftfreq(len(ycrop), dx)
    kxx, kyy = np.meshgrid(k_x, k_y, indexing='ij')
    k_mask = np.sqrt(kxx**2 + kyy**2)
    w_mask = k_mask * fluid.cP
```

```
    p = fft.ifftn(P[nax,:,:] * np.exp(1j*w_mask[nax,:,:]*tcrop[:,nax,nax]), axes =(1,2))
    p_line = (p[:,:, 0 ])

    # zero-pad to wanted lengths in x and t
    pad_t_top = len(t)-it[0][-1] - 1
    pad_x_left = ix[0][0]
    pad_x_right = len(x) - ix[0][-1] - 1
    p_line_pad = np.pad(p_line, ((0,pad_t_top),(pad_x_left, pad_x_right)), 'constant')

    # p_line_pad is excitation on the plate surface
    # p0 is the wavepacket in the cropped domain at t=0
    return p_line_pad, p0


"""
Functions to run the simulation
"""

def sim(params, db, s, theta, fluid, backing, Ra, Ta):
    kx = params['kx']
    w = params['w']

    Rb, Tb = R_T_plate(w, kx, fluid, steel, backing, d = db)
    ky = np.conj(np.sqrt((w[:, nax]/fluid.cP)**2 - (kx[nax, :])**2 + 0j))
    S = np.exp(-1j*ky*s)

    Vpt = partial(Tilt2Dfast, deg_tilt = theta , kx = fft.fftshift(kx),\
                  ky = fft.fftshift(ky), w = fft.fftshift(w), cf = fluid.cP)
    def V(X): # Wrapper for tilt function
        X = fft.fftshift(X)
        X = Vpt(X)
        return fft.fftshift(X)

    return compute_responses(params, Ra, Ta, Rb, S, V, n_responses = 4)

def compute_responses(params, Ra, Ta, Rb, S, V, n_responses = 4):
    x = params['x']
    t = params['t']
    P_in = params['P_in']
    n = params['n']

    P_0 = Ra * P_in

    Y = S * V( Rb * V( S * Ta * P_in ) )
    for _ in range(n_responses):
        P_i =  Ta * Y
        P_0 += P_i
        Y = S * V( Rb * V( S * Ra * Y ) )

    p_tx = prepare_result(P_0, n)
    return p_tx

def prepare_result(P, n):
    p = np.real(fft.ifft2(P))
    p = fft.fftshift( p, axes = 1 )
    p = np.roll(p, -n, axis = 1)
    return p
```

Appendix B

SSPA article: Propagating leaky Lamb waves

The following article was submitted to the Proceedings of the 44$^{\text{th}}$ Scandinavian Symposium on Physical Acoustics. The work is a condensed version of the specialization project written in the autumn of 2020, with some relevant insights developed during the first months of working on the thesis.

The work looks at modeling already initialized Lamb waves, using a different approach to the thesis. In summary, the surface velocity profile can be specified for a Lamb wave packet and mode type, and propagated cheaply in the frequency domain. The leakage to adjacent fluids is included by using an angular spectrum approach.

A fast semi-analytical method for propagating leaky Lamb wavefields

Håvard Kjellmo Arnestad[1], Erlend Magnus Viggen[2]

[1] Department of Physics, Norwegian University of Science and Technology
[2] Centre for Innovative Ultrasound Solutions, Department of Circulation and Medical Imaging, Norwegian University of Science and Technology
Contact email: havard.arnestad@gmail.com

Abstract

A fast method is presented for calculating the wavefields from initialized leaky Lamb waves on plates immersed in sufficiently light fluids. The method works by precomputing the dispersion relation and attenuation, and propagating the wavefields in the frequency domain. An angular spectrum approach is used to include leakage into surrounding fluid. Compared to matching FEM simulations, the computations are performed in the order of seconds, rather than hours. The method also benefits from being much easier to set up correctly, but is on the other hand less general in that it cannot handle e.g. scattering from defects. The correspondence is shown to be good for the case of interest.

1 Introduction

Due its simple geometry, plates and plate-like structures are often encountered in nature as well as in the man-made world. The examples range from the ice on a frozen lake to the hull of a ship, or the casings in an oil well. In situations where such systems are to be probed, acoustic methods are often chosen due to being relatively non-invasive. The methods rely on different principles, but can be broadly categorized into response and modal methods [1]. In response methods, one studies the response from a known excitation, using e.g. reflection coefficients, and in modal methods, one studies the propagation characteristics, such as attenuation or propagation speed. For a plate with a specified initial wavefield, the modal approach is the only feasible option.

The propagation properties of acoustic waves in plates are described by Lamb wave theory, which is a special case of elastic waves in layered media, with only a single layer in a vacuum. In most practical situations, however, the plate is in contact with a fluid on one or both sides, making it "leaky" in the sense that the plate wave is attenuated as waves are radiated into the surrounding medium. The radiation makes fluid-immersed transducers suitable for measuring the radiated wavefront from e.g. a wavepacket propagating on the plate, as is done in pitch-catch well logging [2–5].

Full simulation of ultrasonic plate waves in e.g. COMSOL Multiphysics can be very slow as the domain must be finely meshed. Proper initialization of wave packets is also more complicated than one first may think, because multiple fields must be correctly set up at all relevant frequencies.

ISBN 978-82-8123-021-7

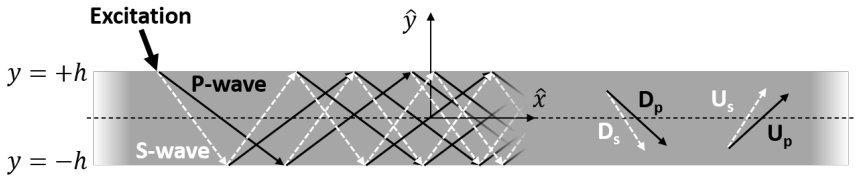

Figure 1: Schematic development of a Lamb wave. D_p, D_s, U_p and U_s represent a steady pattern of P- and S-waves traveling upwards and downwards in the plate. There is vacuum outside the plate boundaries at $y = \pm h$.

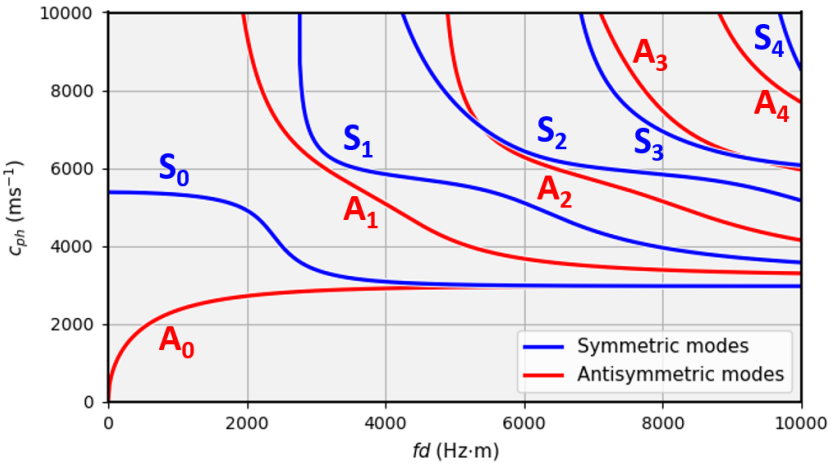

Figure 2: Phase velocities for Lamb modes in a generic steel plate as a function of the frequency-thickness product fd, where $d = 2h$ is the thickness of the plate.

Faster simulation can be achieved by exploiting that the propagation characteristics are already known from modal Lamb wave analysis, as will be presented in this article. The semi-analytical method presented here uses a Fourier decomposition of the wavefield for each mode, where propagation is achieved by adjusting the phase of the mode according to its dispersion relation. Radiation into the surrounding fluid medium is implemented using an angular spectrum approach, relying directly on the aforementioned Fourier decomposition. Attenuation is included using a perturbation-based method valid for light fluids (i.e., with a much lower density than that of the plate).

2 Theory

2.1 Lamb wave theory

Lamb waves are the modal solution of guided waves in a free plate. Consider Fig. 1, which represents a slab of elastic media such as steel. As the plate is excited, waves are reflected from the two free boundaries. Any propagating wavemodes must eventually create a steady pattern of plane waves which leads to different propagating modes that are symmetric (S_0, S_1, etc.) or antisymmetric (A_0, A_1, etc.) with respect to the midplane of the plate. Examples of possible phase and group velocities for these modes are shown in Fig. 2 and 3. To understand how these modes come to be, first consider that two types of waves can be supported in an elastic plate: longitudinal P-waves (for primary/pressure),

ISBN 978-82-8123-021-7

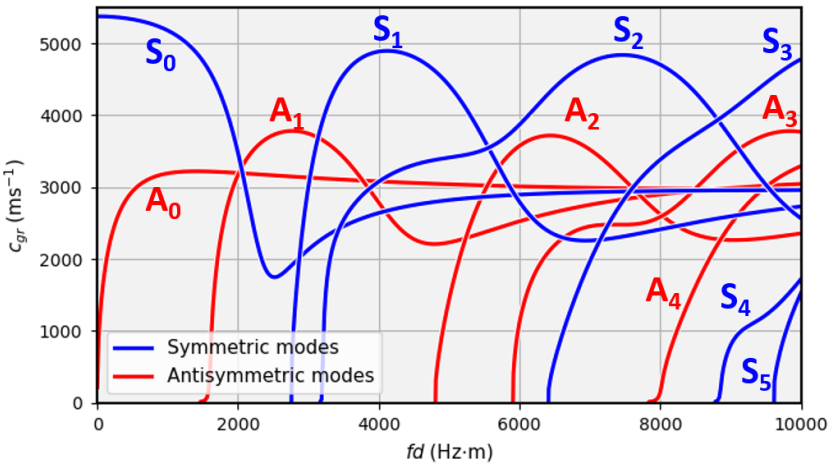

Figure 3: Group velocities for a steel plate as a function of the frequency-thickness product fd.

and transversal S-waves (for secondary/shear), with sound speeds given by

$$c_p = \sqrt{\frac{\lambda + 2G}{\rho}}, \tag{1a}$$

$$c_s = \sqrt{\frac{G}{\rho}}. \tag{1b}$$

Here, λ and G are the first and second Lamé constants that define the stress-strain relationship in isotropic media, and ρ is the density. The Lamé constants can be expressed from the more experimentally available Young's modulus E and Poisson's ratio ν as

$$\lambda = \frac{\nu E}{(1+\nu)(1-2\nu)}, \tag{2a}$$

$$G = \frac{E}{2(1+\nu)}. \tag{2b}$$

The general displacement field $\boldsymbol{u}$ can be written using Helmholtz decomposition theorem from the scalar (ϕ) and vector ($\boldsymbol{\Psi}$) wave potentials as

$$\boldsymbol{u} = \nabla\phi + \nabla \times \boldsymbol{\Psi} = \boldsymbol{u}_p + \boldsymbol{u}_s. \tag{3}$$

A solution is sought in the x-y plane, where the fields are invariant in the z-direction. It can be shown that the u_z-components depends only on the potentials Ψ_x and Ψ_y that are associated with the horizontally polarised shear wave (SH). The other two components depend on potentials ϕ and $\Psi_z = \psi$, associated with longitudinal waves (P) and vertically polarised shear waves (SV), respectively. It is therefore possible to seek solutions separately for the P + SV wave combination. In the remaining analysis the SH waves are discarded because they do not couple to a fluid.

In a solid layer, the fields of a right-going wave may thus be expressed as the superposition of four plane waves. These are the P- and SV-waves (from here on abbreviated as S) propagating in the upwards and downwards directions. Snell's law requires that the wave vectors are oriented so that they all have the same component β, equal to k_x in this situation, along the waveguide propagation direction. That implies the concept

ISBN 978-82-8123-021-7

of transverse resonance for plates; with lossless boundaries, the mode solutions are traveling along the waveguide axis and are standing waves in the transverse direction. The potentials from these four plane waves can be written as

$$\phi = \left[D_p e^{i\gamma_p y} + U_p e^{-i\gamma_p y}\right] e^{i(\omega t - \beta x)}, \tag{4a}$$

$$\psi = \left[D_s e^{i\gamma_s y} + U_s e^{-i\gamma_s y}\right] e^{i(\omega t - \beta x)}, \tag{4b}$$

where D_p and D_s are the wave potential amplitudes of downward-moving P- and S-waves respectively, and U_p and U_s are the amplitudes of upwards-moving waves. The horizontal wavenumbers β are the same for all the plane waves, as mentioned. Because of the different wave speeds, the wavenumbers of P- and S-waves differ: $k_p = \omega/c_p$ and $k_s = \omega/c_s$. The vertical wavenumbers k_y, are therefore also different for P- and S-waves, and are denoted by γ_p and γ_s respectively:

$$\gamma_s = \sqrt{k_s^2 - \beta^2}, \tag{5a}$$

$$\gamma_p = \sqrt{k_p^2 - \beta^2}. \tag{5b}$$

The real power of the formulation emerges when introducing the field variables as expressed via the four wave components. Naturally, when two layers are in contact, the boundary conditions need to be matched. For elastic waves that means the continuity of particle displacement, and normal and shear stress (σ_{yy} and σ_{xy}). One can obtain expressions for the stresses by calculating the strain from particle displacement, and then pipe the result into the constitutive relation for stress, which is where the Lamé constants are introduced. As can be verified with a textbook on the matter [6, 7], one obtains

$$\sigma_{xx} = \lambda\left(\frac{\partial^2\phi}{\partial x^2} + \frac{\partial^2\phi}{\partial y^2}\right) + 2G\left(\frac{\partial^2\phi}{\partial x^2} + \frac{\partial^2\psi}{\partial x \partial y}\right), \tag{6a}$$

$$\sigma_{xy} = G\left(2\frac{\partial^2\phi}{\partial x \partial y} - \frac{\partial^2\psi}{\partial x^2} + \frac{\partial^2\psi}{\partial y^2}\right), \tag{6b}$$

$$\sigma_{yy} = \lambda\left(\frac{\partial^2\phi}{\partial x^2} + \frac{\partial^2\phi}{\partial y^2}\right) + 2G\left(\frac{\partial^2\phi}{\partial y^2} - \frac{\partial^2\psi}{\partial x \partial y}\right). \tag{6c}$$

Any stress component with a z-index is zero, and although σ_{xx} is not an imposed boundary condition, it will be needed in a later section. The last step is to substitute the plane wave formulation of the potentials into the stress and displacement equations. A bit of rearrangement yields a matrix equation for the stress and displacement through the plane wave amplitudes in $y = 0$, which is an arbitrary origin.

$$\begin{bmatrix} \sigma_{yy}(y) \\ \sigma_{xy}(y) \\ u_y(y) \\ u_x(y) \end{bmatrix} = \begin{bmatrix} G(\beta^2 - \gamma_s^2) & G(\beta^2 - \gamma_s^2) & -2G\beta\gamma_s & 2G\beta\gamma_s \\ 2G\beta\gamma_p & -2G\beta\gamma_p & G(\beta^2 - \gamma_s^2) & G(\beta^2 - \gamma_s^2) \\ i\gamma_p & -i\gamma_p & i\beta & i\beta \\ -i\beta & -i\beta & i\gamma_s & -i\gamma_s \end{bmatrix} \begin{bmatrix} D_p e^{+i\gamma_p y} \\ U_p e^{-i\gamma_p y} \\ D_s e^{+i\gamma_s y} \\ U_s e^{-i\gamma_p y} \end{bmatrix}. \tag{7}$$

Similar matrices using a different coordinate convention can be found from e.g. Hovem [7] or Lohne et al. [8]. Using a matrix formulation gives a systematic way of working with guided waves in multi-layered media, such as plates in contact with different fluids or solids. Here we limit ourselves to free plates and will not go into more details or generalizations than needed.

ISBN 978-82-8123-021-7

The plate considered is a single layer with with thickness $d = 2h$, and boundaries to vacuum at $y = \pm h$. The vacuum boundary conditions require that the relevant stresses are zero. Evaluated with respect to the mid-plane of the plate,

$$\begin{bmatrix} \sigma_{yy}(+h) \\ \sigma_{xy}(+h) \\ \sigma_{yy}(-h) \\ \sigma_{xy}(-h) \end{bmatrix} = \begin{bmatrix} 0 \\ 0 \\ 0 \\ 0 \end{bmatrix} = \begin{bmatrix} ae^{+i\gamma_p h} & ae^{-i\gamma_p h} & -be^{+i\gamma_s h} & be^{-i\gamma_s h} \\ ce^{+i\gamma_p h} & -ce^{-i\gamma_p h} & ae^{+i\gamma_s h} & ae^{-i\gamma_s h} \\ ae^{-i\gamma_p h} & ae^{+i\gamma_p h} & -be^{-i\gamma_s h} & be^{+i\gamma_s h} \\ ce^{-i\gamma_p h} & -ce^{+i\gamma_p h} & ae^{-i\gamma_s h} & ae^{+i\gamma_s h} \end{bmatrix} \begin{bmatrix} D_p \\ U_p \\ D_s \\ U_s \end{bmatrix}, \tag{8}$$

where $a = G(\beta^2 - \gamma_s^2)$, $b = 2G\beta\gamma_s$, and $c = 2G\beta\gamma_p$ are introduced for compactness. With a priori knowledge about the solution or by close consideration, one can see that there is a good match between the first two columns, as well as the last two. Therefore, instead of solving for the up- and down-going wave components, a solution to their combinations is sought:

$$\begin{bmatrix} 0 \\ 0 \\ 0 \\ 0 \end{bmatrix} = \begin{bmatrix} +a\cos(\gamma_p h) & +ai\sin(\gamma_p h) & -ib\sin(\gamma_s h) & -b\cos(\gamma_s h) \\ +ci\sin(\gamma_p h) & +c\cos(\gamma_p h) & +a\cos(\gamma_s h) & +ai\sin(\gamma_s h) \\ +a\cos(\gamma_p h) & -ai\sin(\gamma_p h) & +ib\sin(\gamma_s h) & -b\cos(\gamma_s h) \\ -ci\sin(\gamma_p h) & +c\cos(\gamma_p h) & +a\cos(\gamma_s h) & -ai\sin(\gamma_s h) \end{bmatrix} \begin{bmatrix} D_p + U_p \\ D_p - U_p \\ D_s + U_s \\ D_s - U_s \end{bmatrix}. \tag{9}$$

Then the following substitutions are performed $D_p + U_p \to A_2$, $D_p - U_p \to A_1$, $D_s + U_s \to B_2$, and $D_s - U_s \to B_1$. The potentials in Eq. (4) can thus be rewritten as

$$\phi = \left[A_2\cos(\gamma_p y) + iA_1\sin(\gamma_p y)\right]e^{i(\omega t - \beta x)}, \tag{10a}$$

$$\psi = \left[B_2\cos(\gamma_s y) + iB_1\sin(\gamma_s y)\right]e^{i(\omega t - \beta x)}. \tag{10b}$$

The substitutions will take on a more significant meaning soon, as they explain the symmetric and antisymmetric modes in the final solution.

The final step is to further simplify the matrix by row operations on row 1 and 3 and row 2 and 4:

$$\begin{bmatrix} 0 \\ 0 \\ 0 \\ 0 \end{bmatrix} = \begin{bmatrix} a\cos(\gamma_p h) & 0 & 0 & -b\cos(\gamma_s h) \\ ci\sin(\gamma_p h) & 0 & 0 & ai\sin(\gamma_s h) \\ 0 & -ai\sin(\gamma_p h) & +ib\sin(\gamma_s h) & 0 \\ 0 & c\cos(\gamma_p h) & a\cos(\gamma_s h) & 0 \end{bmatrix} \begin{bmatrix} A_2 \\ A_1 \\ B_2 \\ B_1 \end{bmatrix}. \tag{11}$$

To have a wave that can exist without forcing, the matrix must have a determinant of 0. Otherwise, it would be invertible and a non-zero solution of the vector of unknowns could not exist. Writing out the determinant gives

$$\begin{aligned} &[a^2\cos(\gamma_p h)\sin(\gamma_s h) + bc\cos(\gamma_s h)\sin(\gamma_p h)] \\ \cdot&[a^2\cos(\gamma_s h)\sin(\gamma_p h) + bc\cos(\gamma_p h)\sin(\gamma_s h)] = 0. \end{aligned} \tag{12}$$

The determinant is also the product of two individual 2-by-2 determinants in the two upper and two bottom rows. Each can be equal to 0 on its own, as seen from the two square brackets. It will be shown that the two brackets are associated with the symmetric and antisymmetric modes.

After choosing the material parameters and thickness for the plate, the two remaining unknowns are frequency and wavenumber. The two can be matched to give the dispersion relation $\omega(\beta)$ by solving for the zeros of a transcendental characteristic equation (one of the two brackets), a method for which is presented later. The wavefields in the plate can be described entirely once the dispersion relation is known.

ISBN 978-82-8123-021-7

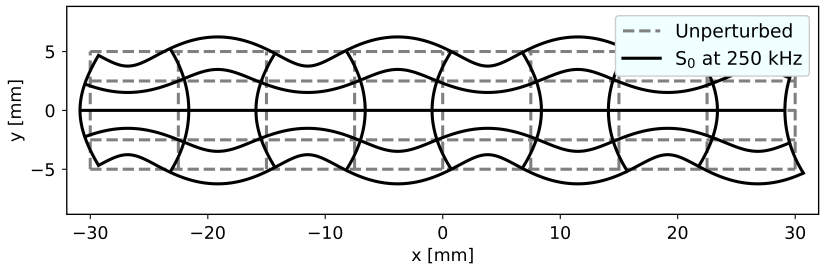

Figure 4: Displacement field of the S_0 mode at 250 kHz in a 1 cm thick steel plate.

2.1.1 Symmetric solution

When the first part of the characteristic equation (12), which describes the components A_2 and B_1, is set to zero, the dispersion relation is implicit in

$$\frac{\tan(\gamma_s h)}{\tan(\gamma_p h)} + \frac{4\beta^2\gamma_s\gamma_p}{(\beta^2-\gamma_s^2)^2} = 0. \tag{13}$$

To obtain the dispersion relation in practice, the roots of Eq. (13) have to be found numerically.

When the dispersion relation holds, the corresponding 2-by-2 submatrix in Eq. (11) has a determinant of 0, and therefore also a free row. That makes it possible to express the ratio of A_2 and B_1 as

$$R_S = \frac{B_1}{A_2} = \frac{(\beta^2-\gamma_s^2)\cos(\gamma_p h)}{2\beta\gamma_s\cos(\gamma_s h)}. \tag{14}$$

The potentials ϕ and ψ are then known, with the exception of an arbitrary scaling that will be represented by K. Substitution back into the relationships (3) and (6) give the full field equations for symmetric Lamb waves

$$\phi^S = K\cos(\gamma_p y) \tag{15a}$$
$$\psi^S = iKR_S\sin(\gamma_s y) \tag{15b}$$
$$v_x^S = i\omega K[\beta\cos(\gamma_p y) - \gamma_s R_S\cos(\gamma_s y)] \tag{15c}$$
$$v_y^S = \omega K[\gamma_p\sin(\gamma_p y) + \beta R_S\sin(\gamma_s y)] \tag{15d}$$
$$\sigma_{xx}^S = iGK[(2\gamma_p^2-\beta^2-\gamma_s^2)\cos(\gamma_p y) + 2\gamma_s\beta R_S\cos(\gamma_s y)] \tag{15e}$$
$$\sigma_{xy}^S = -GK[2\beta\gamma_p\sin(\gamma_p y) + (\beta^2-\gamma_s^2)R_S\sin(\gamma_s y)] \tag{15f}$$
$$\sigma_{yy}^S = iGK[(\beta^2-\gamma_s^2)\cos(\gamma_p y) - 2\gamma_s\beta R_S\cos(\gamma_s y)] \tag{15g}$$

Note that the displacements have been converted to velocities by multiplication with $i\omega$. The common phasor $e^{i(\omega t-\beta x)}$ is also omitted from all quantities.

The notion of symmetric waves come from the field equations. The x-velocities v_x are symmetric around the mid-plane of the plate if described by cosines as seen in Eq. (15c), whereas the y-velocity v_y is symmetric if described by sines as seen in Eq. (15d). For antisymmetric modes, the sines and cosines are swapped. The displacement field of an S_0 symmetric Lamb wave is shown in Fig. 4.

ISBN 978-82-8123-021-7

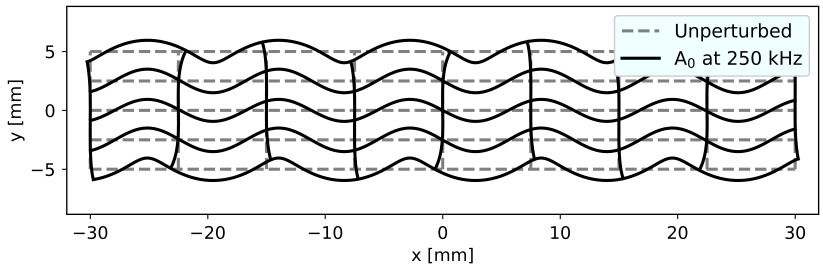

Figure 5: Displacement field of the A_0 mode at 250 kHz in a 1 cm thick steel plate.

2.1.2 Antisymmetric solution

The second part of the characteristic equation (12) describes the antisymmetric modes, and the dispersion relation is implicit in

$$\frac{\tan(\gamma_p h)}{\tan(\gamma_s h)} + \frac{4\beta^2\gamma_s\gamma_p}{(\beta^2-\gamma_s^2)^2} = 0. \tag{16}$$

The same steps as for the symmetric solution are followed. When the dispersion relation holds, the corresponding 2-by-2 submatrix in Eq. (11) has a free row since the determinant is 0. That makes it possible to express the ratio of A_1 and B_2 as

$$R_A = \frac{B_2}{A_1} = \frac{(\beta^2-\gamma_s^2)\sin(\gamma_p h)}{2\beta\gamma_s \sin(\gamma_s h)}. \tag{17a}$$

With the potentials known, again with the exception of an arbitrary scaling K, substitution back into the relationships (3) and (6) gives the full field equations for antisymmetric Lamb waves. Examples of the displacement fields of the A_0 and A_1 modes at 250 kHz are given in Fig. 5 and 6.

$$\phi^A = iK\sin(\gamma_p y) \tag{18a}$$
$$\psi^A = KR_A\cos(\gamma_s y) \tag{18b}$$
$$v_x^A = i\omega K[\beta\sin(\gamma_p y) - \gamma_s R_A \sin(\gamma_s y)] \tag{18c}$$
$$v_y^A = -\omega K[\gamma_p\cos(\gamma_p y) + \beta R_A\cos(\gamma_s y)] \tag{18d}$$
$$\sigma_{xx}^A = KGi[(2\gamma_p^2 - \beta^2 - \gamma_s^2)\sin(\gamma_p y) + 2R_A\beta\gamma_s\sin(\gamma_s y)] \tag{18e}$$
$$\sigma_{xy}^A = KG[2\beta\gamma_p\cos(\gamma_p y) + R_A(\beta^2-\gamma_s^2)\cos(\gamma_s y)] \tag{18f}$$
$$\sigma_{yy}^A = iKG[(\beta^2-\gamma_s^2)\sin(\gamma_p y) - 2R_A\beta\gamma_s\sin(\gamma_s y)] \tag{18g}$$

2.2 Lamb wave attenuation in light fluids

The Lamb wave derivation assume a free plate in vacuum. The interaction with a surrounding fluid or solid would need to be included already in the boundary conditions in Eq. (8). However, in situations where the plate is much denser than the surrounding material, as with a steel plate in water, the Lamb wave structure can be assumed to be unperturbed except for the addition of an imaginary attenuation term α to the wavenumber:

$$k_x = k_{xr} + ik_{xi} = \beta - i\alpha. \tag{19}$$

ISBN 978-82-8123-021-7

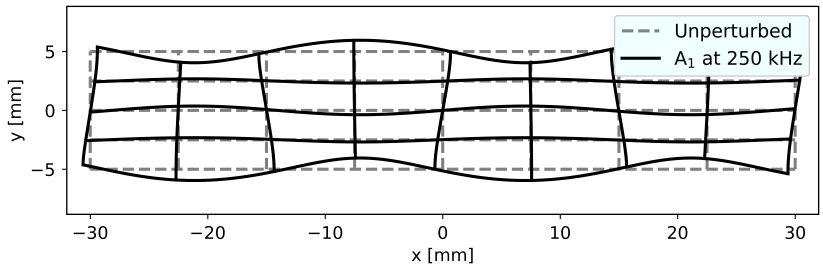

Figure 6: Displacement field of the A_1 mode at 250 kHz in a 1 cm thick steel plate.

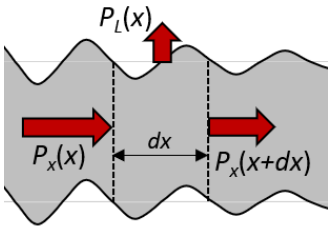

Figure 7: Balance of energy flow into a small element of a plate.

For a wave of initial amplitude A, this implies exponential decay with distance as

$$Ae^{i(\omega t - k_x x)} = Ae^{-\alpha x} \cdot e^{i(\omega t - \beta x)}, \tag{20}$$

with an the attenuation α often measured in neper per meter (Np/m), or in decibel $8.686 \cdot \alpha$ (dB/m).

Several perturbation techniques can be used to calculate approximate attenuation curves. Merkulov [9] used Schoch's characteristic equation (a generalization of Eq. (13) and (16) to include the effect of two-sided fluid loading) to come to an approximation of the attenuation by doing a first order perturbation and assuming the density of the fluid to be small. Another perturbation method is presented by Auld [10], starting from a complex reciprocity relation. The same numerical attenuation values are obtained with both methods through different equations. Here we will look a at a more intuitive method presented in 1982 by Watkins et al. [11] that leads to the same equations as Auld's method.

The main assumption is that the wave retains its structure although power is lost. Consider a differential element of the plate of unit depth, as illustrated in Fig. 7. In steady state a time averaged power $P_x(x)$ is incident from the left, and a power $P_x(x+dx)$ leaves from the right. On the top of the plate a total time-averaged power $P_L(x) = I_L(x) \cdot dx$ is lost to the medium through radiation. Conservation of energy requires that

$$P_x(x+dx) - P_x(x) = -I_L(x) \cdot dx \quad \longrightarrow \quad \frac{dP_x(x)}{dx} = -I_L(x). \tag{21}$$

The time-averaged power flow along the plate can be calculated as

$$P_x = -\frac{1}{2}\int_{-h}^{h} (v_x \sigma_{xx}^* + v_y \sigma_{xy}^*) dy. \tag{22}$$

The next step is to calculate the radiated intensity I_L. Here we only look at the case where the plate is in contact with a fluid, but it is similarly possible to calculate radiated intensity into a solid by taking into account how the vertical and horizontal velocity components contribute to radiated P- and S-waves. For fluids it is enough to consider that

ISBN 978-82-8123-021-7

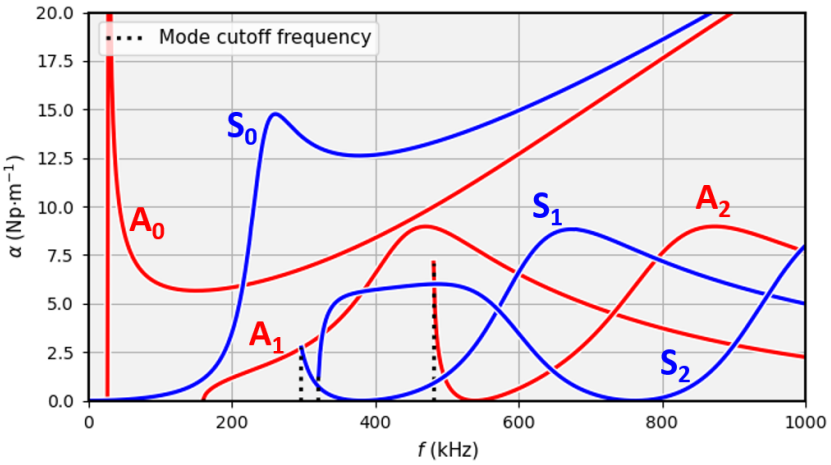

Figure 8: Perturbation values of attenuation for Lamb waves in a 1 cm thick steel plate in contact with water on both sides. Only the first three S- and A-modes are shown. The black dotted lines indicate cutoff frequencies.

the normal velocity is continuous on the interface, and related to the pressure through Euler's equation. The radiated intensity on one side of the plate is [12]

$$I_L = \frac{Z_f |\bar{v}_{ys}|^2}{\sqrt{1 - \left(\frac{c_f}{c_{ph}}\right)^2}}, \tag{23}$$

where $\bar{v}_{ys}$ is the RMS-value of the vertical velocity at the surface of the plate in contact with the fluid. c_f is the speed of sound in the fluid, and Z_f is the specific acoustic impedance, for water $Z_f = 1.48\,\text{MRayl}$.

The intensity and power flow both scale with the square of the amplitude. Hence, $I_L \propto P_x$, and the power flow and radiated intensity exponentially damped as e.g.

$$P_x(x) = P_x(0)e^{-2\alpha x}. \tag{24}$$

This can be inserted into Eq. (21), which can then be re-expressed as

$$\alpha = \frac{I_L}{2P_x} = \frac{\text{Power lost per metre into medium}}{2 \times \text{Power flow along the plate}}. \tag{25}$$

By knowing the dispersion relation, Eq. (22) can be integrated numerically, and Eq. (23) can be evaluated with the same arbitrary scaling K. The result for a steel plate in water is shown in Fig. 8. The curves are identical to Merkulov's first order approximation, but the power flow method benefits by being easier to understand and more flexible; it can treat radiation into solids, and preliminary findings [13] suggest that one can use inhomogeneous ("damped") waves [14] to partially correct for the singularity at coincidence (spike in A_0 mode) and the absence of subsonic radiation. Around coincidence, the real wavenumber also changes appreciably, but the physics get more complicated at lower frequencies, and the current scope is on the higher frequencies. Note that the attenuation curves can deviate significantly from the perturbation solution at higher frequencies if the plate is in contact with water on only one side, or if the fluids have different impedance.

For the purposes of this work, it is more suitable to define the attenuation as happening in time. If ω is taken to be real, the imaginary wavenumber gives a complex

ISBN 978-82-8123-021-7

propagation speed $c = c_r + ic_i$, where $c_r \neq c_{ph}$. To achieve the same attenuation within time interval Δt as with α over the distance $\Delta x = c_{ph}\Delta t$, one can add an imaginary part $i\omega_i$ to ω,

$$Ae^{-\alpha\cdot\Delta x} = Ae^{i\cdot i\omega_i\cdot\Delta t} \quad \longrightarrow \quad \omega_i = \alpha\frac{\Delta x}{\Delta t} = \alpha c_{ph} = \frac{\alpha}{\beta}\omega, \tag{26}$$

and discard the imaginary part of the wavenumber.

2.3 The angular spectrum approach

The angular spectrum method is a superposition method for modeling the propagation of a wave field when the solution is supplied on the plane $y = y'$ [12]. It is based on the fact that $e^{i(\omega t - \boldsymbol{k}\cdot\boldsymbol{r})}$ is a solution of the Helmholtz equation

$$\nabla^2 p + k^2 p = 0, \tag{27}$$

when the wave vector components satisfy

$$k^2 = k_x^2 + k_y^2 + k_z^2 = \beta^2 + k_y^2 = \frac{\omega^2}{c^2}. \tag{28}$$

Note that the wavenumber along an arbitrary propagation direction in the waveguide is given by $\beta^2 = k_x^2 + k_z^2$. Since k is constant for each frequency, the three wavenumbers are not independent. Choosing k_y as dependent, one has that $k_y = \pm\sqrt{k^2 - k_x^2 - k_z^2}$, where the appropriate root must be chosen.

When a vibrating steel plate is in contact with e.g. air, the wavefield in the x-z plane is given because it is imposed by the velocity field of the steel plate. The traces of the wavefronts in the air must match the wavefronts on the steel. The component k_y can thus be real or imaginary as a consequence. The latter implies a non-propagating evanescent wave into the air, when the phase velocity of the plate wave is subsonic with respect to the surrounding air.

First consider an initial complex wavefield at $t = 0$ on the plate surface at $y = y'$, expressed through its vertical surface velocity v_{ys}. It can be decomposed into a sum of plane waves through the Fourier transform

$$V_{ys}(k_x, k_z) = \mathcal{F}_x\mathcal{F}_z\{v_{ys}(t = 0, x, y = y', z)\}, \tag{29}$$

which is also known as the angular spectrum. For waves propagating on a plate, the dispersion relation $\omega(\beta)$ is already known, and using Eq. (26), the attenuation with time can be included.

The time-evolution of each plane wave component has a simple description, only changing by a phase factor and attenuated. Therefore, the propagated wavefield on the plate can be obtained by injecting a "time propagator", and performing the inverse Fourier transform:

$$v_{ys}(t, x, y = y', z) = \iint \underbrace{V_{ys}(k_x, k_z)}_{\text{Angular spectrum}} \cdot \overbrace{e^{i(k_x x + k_z z)}}^{\text{Fourier Basis}} \cdot \underbrace{e^{i(\omega(\beta) + i\omega_i)t}}_{\substack{\text{Time}\\ \text{propagator}}} dk_x dk_z. \tag{30}$$

The normal velocity field is interesting on a plate, but the pressure p is more meaningful in a fluid. Euler's equation in the frequency domain can be used to relate the normal velocity to the fluid pressure just above the plate

$$i\omega\rho\boldsymbol{V} = -\nabla P. \tag{31}$$

ISBN 978-82-8123-021-7

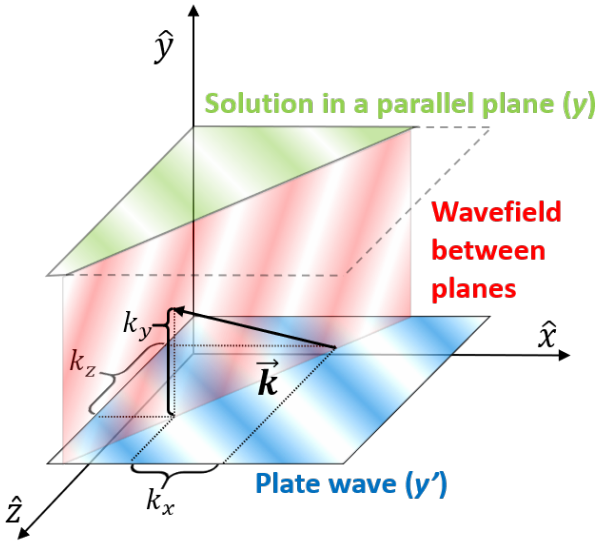

Figure 9: Propagation of a monochromatic wavefield from a plate (blue) into a parallel plane (green). The colored gradients represent wavefronts. The wave vector components k_x and k_z are imposed by the plate at $y = y'$. The wavefield between the planes, here shown as a cross section (red), can be calculated as different solution planes.

Doing the conversion using the dispersion relation frequency $\omega(\beta)$ brings some benefits that will be discussed in section 3.3. In that case one can calculate the angular spectrum of the pressure field above the plate at $t = 0$, $P(k_x, k_z)$. Then, it is possible using the method represented in Eq. (30) to propagate the wavefield to different times of interest, giving $P(t, k_x, k_z)$. Performing a Fourier transform over the t-dimension, one obtains $P(\omega', k_x, k_z)$, with ω' given by the sampling of t, and not the dispersion relation. Since k_y in the fluid is given by k_x and k_z via Eq. (28), one can propagate the wavefield between parallel planes, as shown in Fig. 9, as

$$p(t,x,y,z) = \iiint \underbrace{P(\omega', k_x, k_z)}_{\text{Angular spectrum}} \cdot \overbrace{e^{i(\omega' t + k_x x + k_z z)}}^{\text{Fourier Basis}} \cdot \underbrace{e^{ik_y(y'-y)}}_{\substack{\text{Propagator to} \\ \text{parallel planes}}} dk_x dk_z d\omega'. \tag{32}$$

In practice, the implementation uses the Fast Fourier Transform (FFT) or its inverse (IFFT). Hence, the solution domain will have to be sampled to resolve the shortest wavelength and highest frequency, and it will be periodic. The method naturally handles effects such as diffraction, dispersion, and attenuation.

Another method known as normal mode expansion (NME) [6, 15] is similar in some aspects to the presented method. It is a method for calculating the excitation of waveguides, and works by computing "modal participation factors" that carry a similar meaning to the angular spectrum coefficients here.

3 Method

3.1 Numerical solution of the Lamb dispersion relation

Equations (13) and (16) implicitly relate the frequency ω to a wavenumber β along the propagation direction. For any frequency, there are a finite number of purely propagating

ISBN 978-82-8123-021-7

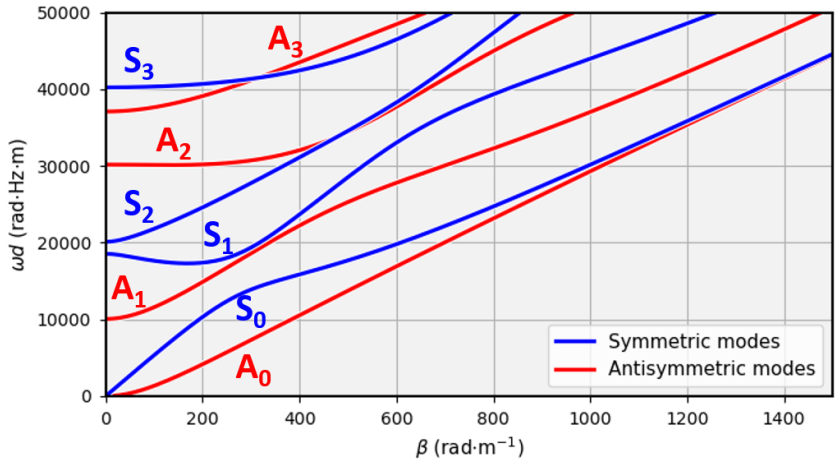

Figure 10: Dispersion curves as they are traced out. Notice that the curves are not one-to-one, and more predictable than e.g. the phase velocity Fig. 2.

modes (A_0, S_0, A_1, S_1, etc.), as shown e.g. in Fig. 2. Tracing out the dispersion curves is necessary, and this section describes a procedure to do so.

The first step is to recognize that γ_s and γ_p will change from being real to imaginary depending on the wavenumber β and frequency. This causes (13) and (16) to switch between having real and imaginary roots. As an example of a special case, it is known that the phase velocity for the A_0 mode is bounded between 0 and the Rayleigh wave velocity $c_R < c_s$, making the vertical wavenumbers γ_s and γ_p imaginary. For other modes, one or both of the vertical wavenumbers may become real at some point. To simplify analysis, it is therefore useful to rewrite the characteristic equations so they take on only real values for real horizontal wavenumbers β. From Rose [6], this can be done as

$$\frac{\tan(\gamma_s h)}{\gamma_s} + \frac{4\beta^2\gamma_p \tan(\gamma_p h)}{(\gamma_s^2 - \beta^2)^2} = 0 \quad \text{for symmetric modes,} \tag{33a}$$

$$\gamma_s \tan(\gamma_s h) + \frac{(\gamma_s^2 - \beta^2)^2 \tan(\gamma_p h)}{4\beta^2\gamma_p} = 0 \quad \text{for antisymmetric modes.} \tag{33b}$$

The curves change sign when crossing 0, so a root-finding algorithm can be used. However, caution should be taken as the equations also change sign when crossing a pole. Depending on the algorithm used, one should test that the obtained root is in fact fairly close to 0. The curves are traced out as $\omega(\beta)$, as seen in Fig. 10 for two reasons. Firstly, these curves are two-to-one, meaning we can capture the back-propagating modes (negative group velocity, e.g. S_1 mode at low frequencies). Secondly, as Lowe points out [1], they are more easily traced out than say $c_{ph}(\omega)$ which perhaps is the most intuitive choice to go for.

Tracing out the modes is a bit involved, in particular due to the possibility of having holes in the curves. The holes are regions where no roots are found for a mode, and the consequences are potentially that a mode is missed, or that one reaches a dead end when following a curve. In brief, the algorithm used here works as follows:

1. Choose either Eq. (33a) or (33b).

ISBN 978-82-8123-021-7

2. Make a list of β values: $(\beta_0, \ldots, \beta_i, \beta_{i+1} \ldots \beta_n)$ for a fine search for roots/modes along the ω axis.

3. For each β_i, trace out the modes found as follows:

   i Store the values of each root as the intersection with a mode.

   ii Do a similar search nearby $(\beta_i + \delta\beta)$ to estimate the derivative $\partial\omega/\partial\beta$.

   iii Trace the modes (as far as possible) down to β_{i-1} and up to β_{i+1}, taking small steps of e.g. $\Delta\beta = 5$, and store the result as a piece of a mode curve for the index i.

4. Starting from $i = 0$, go through each curve piece, and splice with the best matching curve piece in $i = 1$ (if any), then for $i = 2$, and so on:

   i Splice two curve pieces if they overlap at some point with a similar angle (< 5 degrees).

   ii If any curve pieces remain, they are attempted to be matched based on how well linear extrapolation finds the midpoint between the unconnected ends. An upper tolerable error is defined from the derivatives $\partial\omega/\partial\beta$, and length of the gap.

   iii Unmatched curve pieces are at this point considered as new modes.

5. The fully traced modes are then labeled e.g. A_0, A_1, etc. based on their lowest frequency, in line with how higher modes have higher cut-off frequencies [16].

6. The mode curves are finally fitted with a spline function to get $\omega(\beta)$. For the inverse function $\beta(\omega)$ the fit ignores the back-propagating modes, so it is a one-to-one function.

When a spline function is obtained, it is quite easy and fast to work with, as the mode tracing is separate from everything else. The method above has worked very well for steel plates and similar materials up to at least 1 MHz·mm, but for very different material parameters it is difficult to assess general robustness. Using the above method will therefore require inspection, and potential tweaking of hyperparameters such as the step length $\Delta\beta$. It should also be mentioned that at very low frequencies, the A_0 and S_0 modes may be difficult to trace due to issues relating to the numerical range and precision of e.g. floats or doubles in the characteristic equations. In those situations, the low frequency approximations given in [16] can be used. Finally, in cases where one is interested in general leaky Lamb dispersion relations, the wavenumber is complex, and the search for roots is significantly more difficult, but still possible as described by Lowe [1].

3.2 Plate wave propagation

To propagate a wavefield on a plate, the first step is to choose the dimensions and discretization of the plate. The Nyquist sampling theorem requires more than two samples per smallest wavelength to be simulated. Then, the vertical surface velocity v_{ys} profile is specified, and here we will consider the simple case of a Gaussian wavepacket propagating along the x-direction, $\theta = 0$, on the plate. It can be expressed as

$$v_{ys}(t = 0, x, z) = e^{-\frac{(x-x_0)^2+(z-z_0)^2}{2\sigma^2}} \cdot e^{-i\beta_c[\cos\theta(x-x_0)+\sin\theta(z-z_0)]}, \tag{34}$$

ISBN 978-82-8123-021-7

where β_c is the wavenumber at the center frequency of the wavepacket, and x_0 and z_0 the initial location. The wavefield is complex valued, which is necessary for defining the propagation direction. The spatial extent of the wavepacket is given by σ^2, using the full width at half maximum (FWHM), $\sigma \approx \text{FWHM}/2.355$. In this work $\text{FWHM} = 2\lambda_c = 4\pi/\beta_c$.

An attractive feature of the method is that specifying only v_{ys} is enough, even though one has velocity components in the x-direction, and stress/strain fields inside the plate. The reason is that all field relations are implicit in the Lamb wave assumption and dispersion relation. The only situation where v_{ys} cannot capture a Lamb wave mode, is for certain frequencies in the higher modes. Looking at Fig. 8, the S_1 mode has 0 attenuation at a particular frequency, and the reason is that $v_{ys} = 0$ even though there is a wave with non-zero power flow P_x. For each Lamb mode the procedure of calculating propagation is:

1. **Starting point:** Complex wavefield or wavepacket at $t = 0$, (x, z).
2. **Fourier transform:** Wavenumber domain, (k_x, k_z).
3. **Propagate to different times:** Using the "time propagator" in Eq. (30), (t, k_x, k_z).
4. **Inverse Fourier transform:** Propagated wavefields, (t, x, z).

The parenthesis at each step shows the the dimensions of the data worked with. A reason why the method is fast is that optimized FFT routines can be used, along with broadcasting/vectorization. Using Python, the step from (k_x, k_z) to (t, k_x, k_z) is written on one line using Numpy arrays, completely avoiding inefficient Python loops.

Table 1: Material parameters used.

Material	ρ (kg·m^{-3})	c_p (m·s^{-1})	c_s (m·s^{-1})
Steel	7850	5900	3200
Water	1000	1480	-

3.3 Including leakage to fluid

Sometimes a plate wave can be interesting to model on its own, but in most practical settings the interaction with a surrounding fluid is key. A few modifications to the list in the previous section is needed; new steps are marked with (*):

1. **Starting point:** Complex wavefield or wavepacket at $t = 0$, (x, z).
2. **Fourier transform:** Wavenumber domain, (k_x, k_z).
3. *** Convert to pressure:** Using Euler's equation (alternatively after step 6).
4. *** Add attenuation:** $\omega \to \omega(1 + i\frac{\alpha}{\beta})$.
5. **Propagate to different times:** Using the "time propagator", (t, k_x, k_z).
6. *** Transform to frequency domain:** ω' given by sampling of t, (ω', k_x, k_z).

ISBN 978-82-8123-021-7

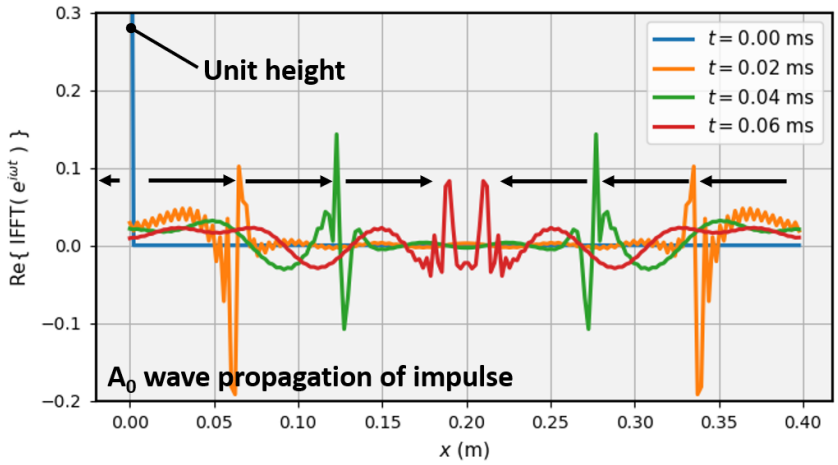

Figure 11: The equivalent convolution kernels that propagates a wavefield as a leaky A_0 Lamb wave by a time t.

i If step 3 is moved, reduce spectral leakage from the "sudden" initialization of the plate wave with a window function in time, e.g. Tukey (see next section).

ii Zero padding to avoid temporal wrap-around with y (see next section).

7. * **Propagate to parallel planes of interest:** Using Eq. (32), (ω', k_x, y, k_z).

8. **Inverse Fourier transform:** Wavefield in fluid, (t, x, y, z).

Step 3, converting to pressure, can alternatively be moved to after step 6. The difference is between using the frequency from the dispersion relation ω, or the frequency from the time sampling t, ω'. Doing the conversion in step 3 with ω avoids an unwanted "startup wave" as in Fig. 16.

3.4 Frequency domain periodicity

The method works in the frequency domain where the solution is periodic. To understand the implications of that, we start by looking at the "time propagator" in more detail. It works like a filter that is applied in the frequency domain by multiplication. In the spatial domain, it would be a convolution by a kernel that is a function of propagation time, as shown in Fig. 11.

The intial impulse splits into a left- and right-going pulse. Which direction is determined by the wavenumber, so if the initialized wavefield is defined to move to the right, the left-going pulse will be zero. The peak in this particular case moves at roughly the typical group velocity (A_0 mode), and attenuation is included. Once the pulse moves to the right end ($x = 0.4$ m) it will wrap back to the beginning ($x = 0.0$ m).

To avoid wraparound effects, one must essentially the avoid the effects of circular convolution that may turn up when doing the convolution in the frequency domain without zero-padding. To have linear convolution, the length L after convolution must be given by

$$L = N + M(t) - 1, \tag{35}$$

where N is the number of samples in the domain, and $M(t)$ is the appropriate number of samples in the convolution kernel. In the circular convolution case $L = N$, and $M(t)$

ISBN 978-82-8123-021-7

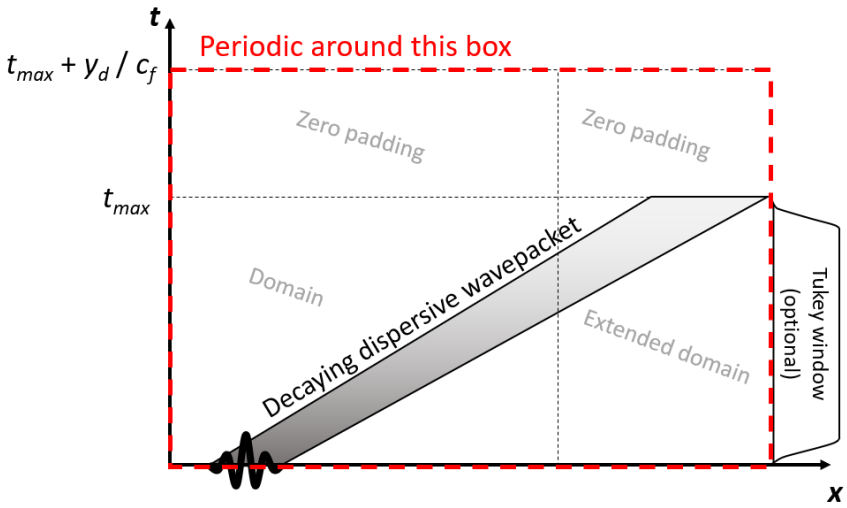

Figure 12: Illustrations of necessary domain extension and zero padding in time to avoid wrap-around artifacts. The Tukey window is optional, but reduces spectral leakage if one does the conversion to pressure after step 6 in the recipe.

is then the zero-padding needed to extend the domain, see Fig. 12. It can be decided by taking into account the largest group velocity of interest, the propagation time, and the spatial sampling rate. It may not be necessary to use full domain extension if, for instance, the wavefield consists of a well localized wavepacket on one side of the domain.

When the wavefield of the plate is propagated into the fluid, the propagation delay plays a role. The wavefield a distance y_d away from the plate surface is unaffected by the current plate vibration until a time $t_d = y_d/c_f$ has passed, depending on the sound speed in the fluid c_f. From step 6 in the recipe in sec. 3.3, the solution is periodic in time, and when moving away from the radiating plate surface, the wavefield is determined by a increasingly distant past. Therefore, as the distance y increases, the delayed time will eventually cause a wrap-around in the solution. To avoid this, sufficient zero padding in time must be used. The amount depends on how far away from the plate one wants to propagate the wavefield. A schematic representation of necessary zero padding is shown in Fig. 12.

4 Results and discussion

4.1 Free plate propagation

The method is implemented in Python, and compared with equivalent simulations in COMSOL Multiphysics. To verify 1D propagation for a free plate, an A_0 wavepacket propagating to the right is initialized at $x_0 = -25$ cm with a center frequency of 250 kHz. The vertical midplane velocity is measured.

The COMSOL simulation is realized by calculating the necessary fields $\boldsymbol{u}(x,y)$ and $v(x,y)$, using e.g. Eq. (18c), at the center frequency of 250 kHz, and windowing using a Gaussian function. This is an approximation, as the windowing introduces a bandwidth of frequencies that are not properly modeled. It is deemed unfeasible to synthesize the different fields one frequency at a time, but for this example, the maximum deviance in intensity I_x that contributes to the power flow P_x is 2%. For all simulations 6 quadratic

ISBN 978-82-8123-021-7

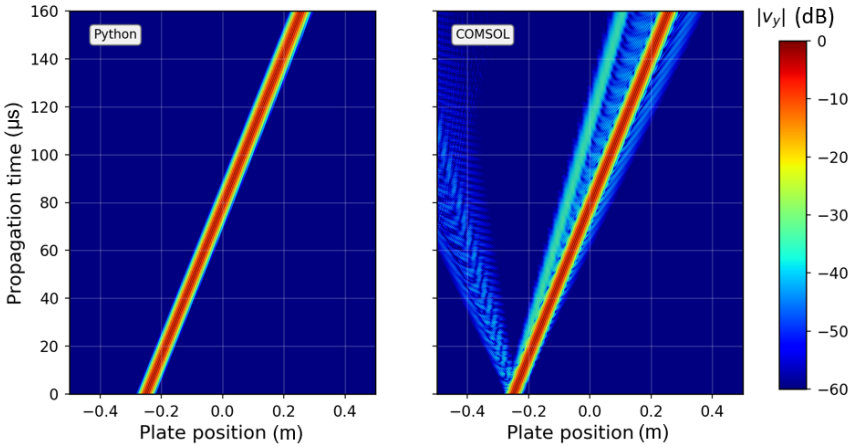

Figure 13: Comparison of 1D propagation for a free plate. The presented method is shown in the Python implementation. The COMSOL simulation shows additional modes due to the approximation used when initializing the fields.

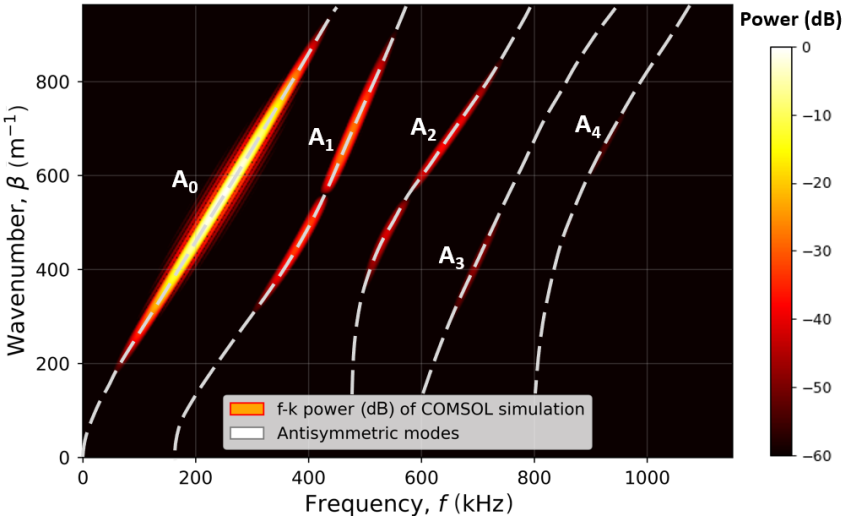

Figure 14: f-k plot from the COMSOL simulation between $-0.2\,\mathrm{m}$ to $0.3\,\mathrm{m}$ and from $20\,\mu\mathrm{s}$ to $140\,\mu\mathrm{s}$. The modes A_1, A_2 etc. come from the inexact initialization in COMSOL.

elements per wavelength at 500 kHz is used, unless stated otherwise.

The propagation in the two cases can be seen in Fig. 13. The method presented in this work shows a single very weakly dispersive wavepacket. In COMSOL, the targeted A_0 wavepacket is simulated in the same way, but additional modes are also present. The explanation is the approximation used when initializing the fields. The f-k plot in Fig. 14 shows clearly that the deviation comes from higher-order antisymmetric Lamb modes, confirming that the error is related to the initialization and not numerical.

A verification of 2D propagation is also shown in Fig. 15, where one sees the wavepacket from above the plate as it propagates and diffracts. The two different solutions are shown on each side of the symmetry axis. For the same reasons as in 1D, there are additional modes in this simulation, but it is quite clear that the main A_0 wavepacket behaves similarly. The boundary conditions at $z = \pm 0.1\,\mathrm{m}$ are different; they are periodic in the Python implementation, and fixed in COMSOL. The reason touches on the motivations

ISBN 978-82-8123-021-7

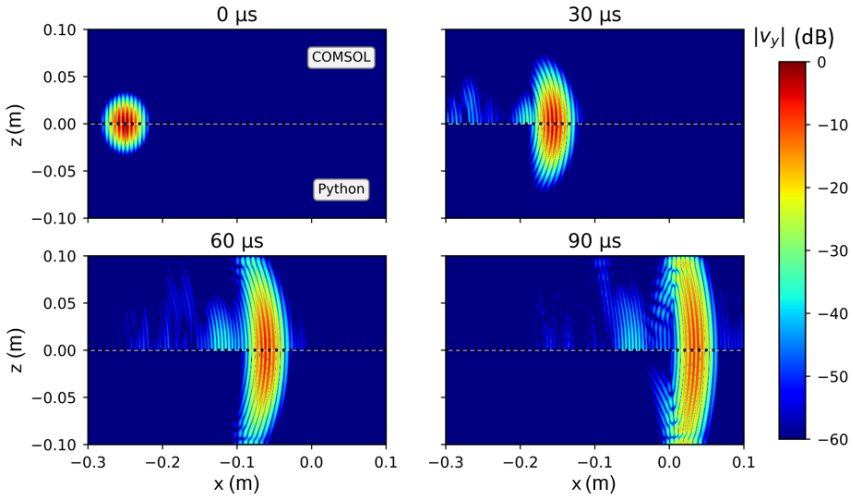

Figure 15: 2D propagation, with different solutions above and below the propagation axis. The x-z-plane represents the plate surface.

for the work, as a very fine mesh is needed for simulating ultrasonic waves. Also, the 2D propagation requires a 3D model to capture the plate thickness, and the memory usage and simulation time had to be reduced. Even when using two planes of symmetry, reducing the maximum frequency to 400 kHz, and shrinking down the domain into what is seen, it still took roughly 8 hours to compute. Although no formal benchmarking has been performed, the computation time on the same computer was on the order of a couple of seconds using the presented method.

4.2 Leaky wave propagation

Simulations of fluid interaction are performed in 1D. The setup consists of a steel plate of 1 cm thickness with water on both sides, as seen in Fig. 16. Here it is assumed that the Lamb waves do not change their propagation characteristics except for being attenuated.

The COMSOL simulation shows a "startup" wave that seem to spread almost circularly from the initial position. It is not seen in the vertical surface velocity, and is therefore not a form of interface wave, but an artifact that occurs when a wave suddenly "pops" into existence. The comparison is done by monitoring the pressure 1 cm above the plate, as illustrated with the red dotted line.

In this work, the artificial "startup" wave is not present, as seen in Fig. 17. The reason has already been discussed, and is attributed to the velocity to pressure conversion before propagating the wavefield in time. Doing the conversion to pressure at a later stage introduces the "startup" wave. A finer comparison of the waveforms 1 cm above the plate is shown in Fig. 18. As soon as the "startup" wave and the leaked wavefield separate after some time, it shows that both attenuation and wave shape is modeled quite well. A slight shift of the waveform is likely owing to the minor influence of the water loading on the exact real horizontal wavenumber β, and/or numerical dispersion in COMSOL.

ISBN 978-82-8123-021-7

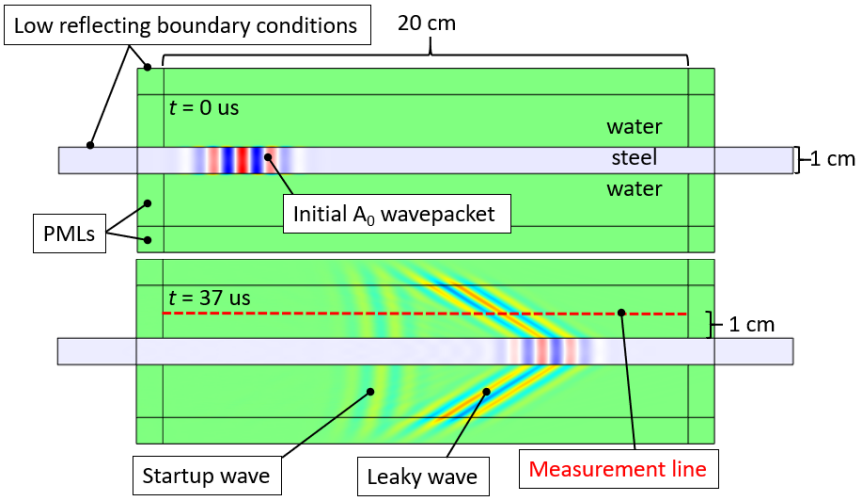

Figure 16: COMSOL model used to verify leaky wave propagation. The measurement line indicates the x-axis shown in Fig. 18.

5 Conclusion

A fast semi-analytical method that can propagate initialized leaky Lamb wavefields has been presented. Although no formal benchmarks have been performed, it is clear that computations are done within seconds, while matching computations in COMSOL have usually taken several hours. The speed-up is mainly attributed to

1. having precomputed the propagation characteristics in e.g. the dispersion relation,
2. not having to discretize the direction normal to the plate and having all field relations implicit, and
3. benefiting from optimized FFT routines and vectorization.

The method has been tested for A_0 wave propagation under the assumption that the fluid is sufficiently light compared to the plate so that classical Lamb wave theory together with a perturbative method for calculating attenuation is sufficient. The agreement is good, and assumed sufficient for most applications. Because the unwanted "startup" wave is not turning up in the presented method, it is well suited for calculating leaked wavefields in a fluid from known wavefields on a plate.

Acknowledgment

The contribution of E.M. Viggen to this work was supported by the Research Council of Norway under grant number 237887.

References

[1] M. J. S. Lowe, "Matrix techniques for modeling ultrasonic waves in multilayered media," *IEEE Transactions on Ultrasonics, Ferroelectrics, and Frequency Control*, vol. 42, no. 4, pp. 525–542, 1995.

ISBN 978-82-8123-021-7

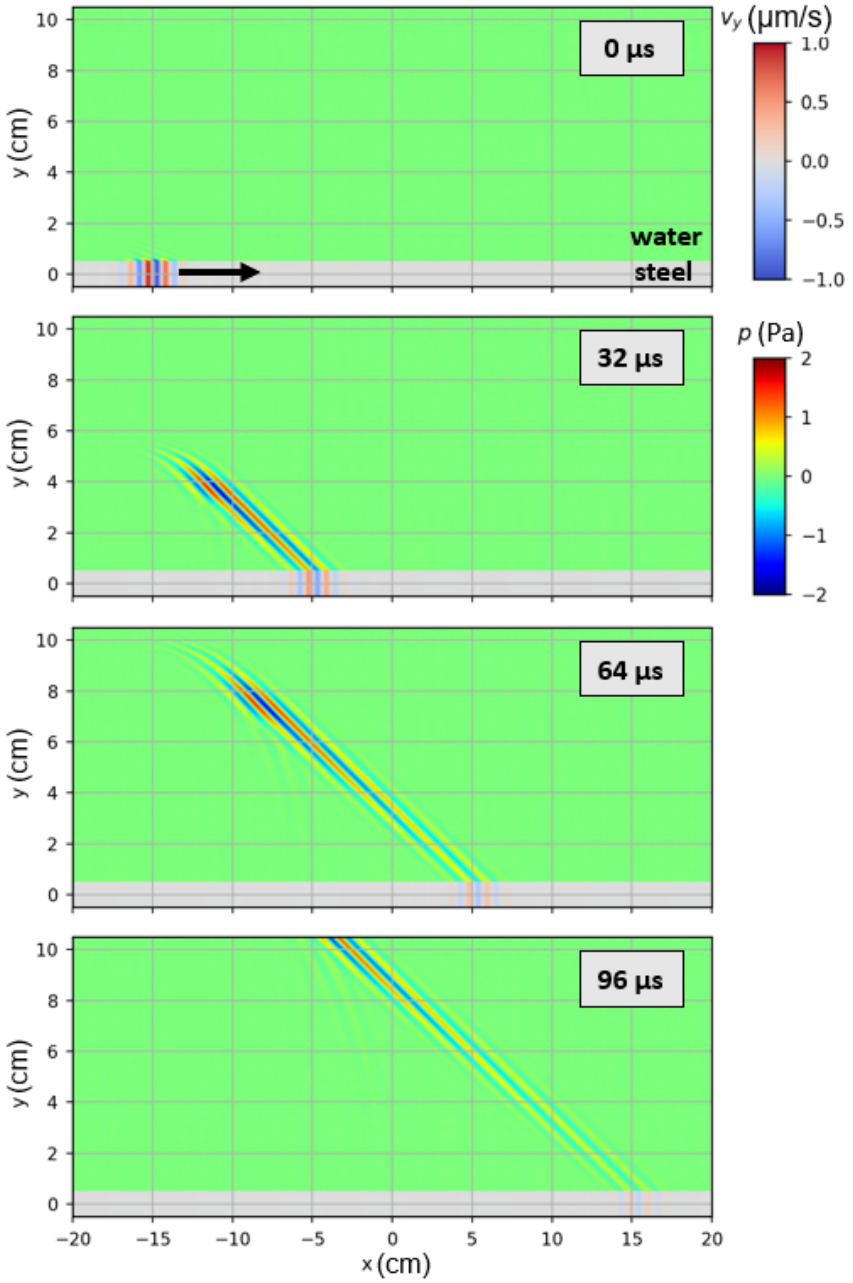

Figure 17: Sequence of snapshots from a simulation of an A_0 wavepacket on a steel plate in water, using the method presented in this work.

ISBN 978-82-8123-021-7

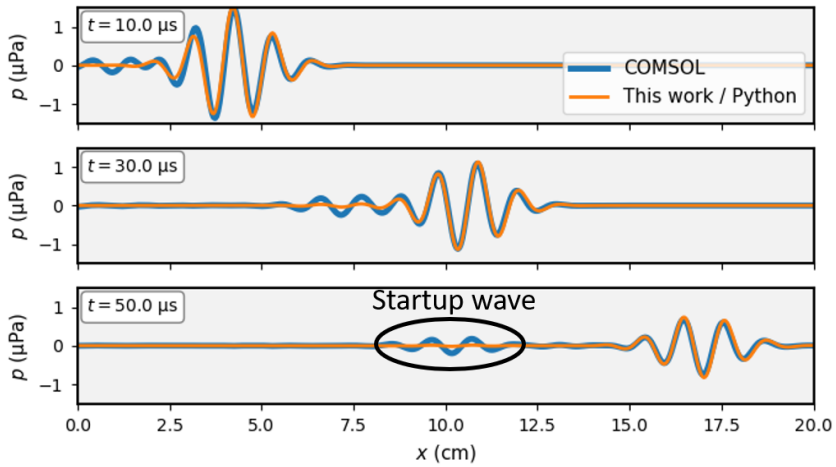

Figure 18: Comparison of this work with COMSOL. The biggest difference is the absence of the "startup wave" which is an artifact when a wavepacket suddenly comes into existence.

[2] R. van Kuijk, S. Zeroug, B. Froelich, M. Allouche, S. Bose, D. Miller, J.-L. le Calvez, V. Schoepf, and A. Pagnin, "A novel ultrasonic cased-hole imager for enhanced cement evaluation." Presented at the International Petroleum Technology Conference, 2005.

[3] C. Klieber, T. Brill, S. Catheline, Y. Vincensini, and F. Mege, "Visualization of Leaky Ultrasonic Lamb Wave Experiments in Multilayer Structures," *Physics Procedia*, vol. 70, pp. 314–317, 2015.

[4] E. M. Viggen, T. F. Johansen, and I.-A. Merciu, "Simulation and modeling of ultrasonic pitch-catch through-tubing logging," *Geophysics*, vol. 81, no. 4, pp. D383–D393, 2016.

[5] ——, "Simulation and inversion of ultrasonic pitch-catch through-tubing well logging with an array of receivers," *NDT & E International*, vol. 85, pp. 72 – 75, 2017.

[6] J. L. Rose, *Ultrasonic Guided Waves in Solid Media*. Cambridge University Press, 2014.

[7] J. Hovem, *Marine Acoustics: The Physics of Sound in Underwater Environments*. Peninsula Publishing, 2012.

[8] K. D. Lohne, P. Lunde, and M. Vestrheim, "Ultrasonic signal transmission in plates – study of a steel plate immersed in water," ser. Proceedings to the 31th Scandinavian Symposium on Physical Acoustics, 2008.

[9] L. G. Merkulov, "Damping of normal modes in a plate immersed in a liquid," *Soviet Physics-Acoustics*, vol. 10, no. 2, pp. 169–173, 1964.

[10] B. A. Auld, *Acoustic Fields and Waves in Solids*, 2nd ed., ser. Acoustic Fields and Waves in Solids. Krieger Publishing Company, 1990, vol. II.

[11] R. D. Watkins, W. H. B. Cooper, A. B. Gillespie, and R. B. Pike, "The attenuation of lamb waves in the presence of a fluid," *Ultrasonics*, vol. 20, no. 6, pp. 257 – 264, 1982.

ISBN 978-82-8123-021-7

[12] G. Williams, *Fourier Acoustics: Sound Radiation and Nearfield Acoustical Holography*. Elsevier Science, 1999.

[13] E. M. Viggen and H. K. Arnestad, "Understanding sound radiation from surface vibrations moving at subsonic speeds," in *Proceedings of the 44th Scandinavian Symposium on Physical Acoustics*. Norwegian Physical Society, 2021, p. 4, extended abstract.

[14] N. Declercq, R. Briers, J. Degrieck, and O. Leroy, "The history and properties of ultrasonic inhomogeneous waves," *IEEE transactions on ultrasonics, ferroelectrics, and frequency control*, vol. 52, pp. 776–91, 2005.

[15] A. M. Kamal, B. Lin, and V. Giurgiutiu, "Exact analytical modeling of power and energy for multimode lamb waves excited by piezoelectric wafer active sensors," *Journal of Intelligent Material Systems and Structures*, vol. 25, no. 4, pp. 452–471, 2014.

[16] I. A. Viktorov, *Rayleigh and Lamb Waves*. Plenum Press, 1967.

ISBN 978-82-8123-021-7

Appendix C

SSPA extended abstract: Subsonic radiation

The following extended abstract was submitted to the Proceedings of the 44$^{\text{th}}$ Scandinavian Symposium on Physical Acoustics. The work explores how inhomogeneous waves can explain subsonic radiation, which happens below the coincidence frequency. The effect was initially puzzling, as waves are expected to be evanescent, with zero net radiated intensity. The power flow method for calculating attenuation is developed to include the inhomogeneous waves, and used to demonstrate the validity for flexural Lamb waves.

Understanding sound radiation from surface vibrations moving at subsonic speeds

Erlend Magnus Viggen[1], Håvard Kjellmo Arnestad[2]

[1] Centre for Innovative Ultrasound Solutions, Department of Circulation and Medical Imaging, Norwegian University of Science and Technology
[2] Department of Physics, Norwegian University of Science and Technology
Contact email: erlend.viggen@ntnu.no

Extended abstract

The interaction between a vibrating surface and an adjacent fluid is a common topic in many subfields of acoustics, for example building acoustics, noise control, and acoustic non-destructive testing. In the most fundamental formulation, the specified normal velocity v_y of the vibrating surface at $y = 0$ and the resulting fluid pressure p can be expressed as

$$v_y(x, 0, t) = v_{y0}\, \mathrm{e}^{\mathrm{i}(k_x x - \omega t)}, \tag{1a}$$

$$p(x, y, t) = p_0\, \mathrm{e}^{\mathrm{i}(k_x x + k_y y - \omega t)}\,. \tag{1b}$$

Here, the fluid wavenumber y-component k_y can be calculated from the surface wavenumber k_x and the fluid wavenumber $k_f = \omega/c_f$ as

$$k_y = \sqrt{k_f^2 - k_x^2} = k_f \sqrt{1 - (k_x/k_f)^2}. \tag{2}$$

With c_f being the fluid sound speed and $c_v = \omega/k_x$ being the surface vibration speed, this can also be expressed as $k_y = k_f \sqrt{1 - (c_f/c_v)^2}$.

Classic treatments of this problem (see e.g. [1]) find two solution domains depending on the surface vibration speed c_v. In the *supersonic* domain ($c_v > c_f$), the wavenumber k_y is real-valued, and (1b) expresses a plane fluid wave radiating away from the surface. In the *subsonic* domain ($c_v > c_f$), however, k_y is imaginary-valued, so that (1b) expresses an evanescent, non-radiating fluid wave that decays exponentially away from the surface.

However, multiple articles have shown radiating fluid waves to exist even in the subsonic domain, specifically for Rayleigh waves [2] and Lamb waves [3–5]. These results follow by numerically solving the complex dispersion equations for the investigated type of wave. While this mathematical approach is standard and correct, it does not explain *why* this subsonic radiation can occur. One brief qualitative explanation is provided in [2], where the subsonic radiation is related to the attenuation of the surface vibration. This attenuation is caused by the loss of the power radiated into the fluid by the pressure wave.

In our work, we investigate subsonic radiation more closely through a simple physical model. We take the formulation in (1) and (2) and generalise it to an attenuated

ISBN 978-82-8123-021-7

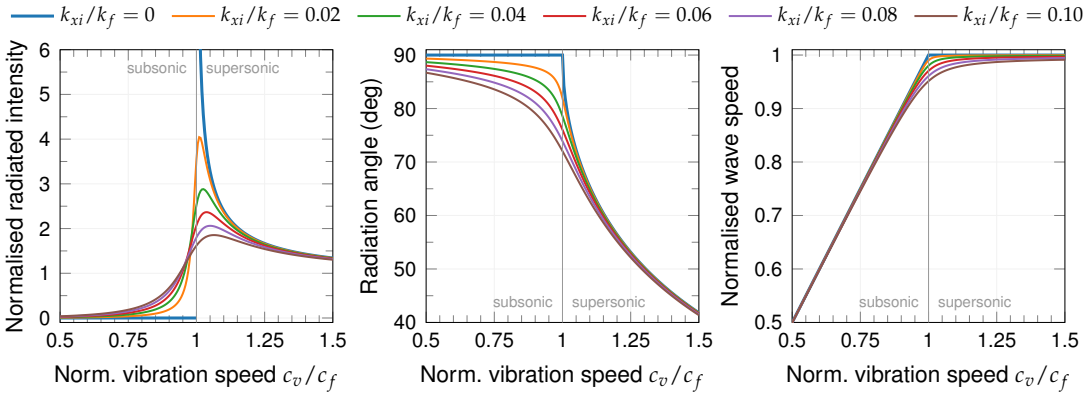

Figure 1: Properties of the wave radiated from an attenuated surface vibration. Left: Normalised radiated intensity $I_{y0}/(v_{y0}^2 Z_f/2) = (k_{yr}/k_f)/|k_y/k_f|^2$. Middle: Radiation angle $\theta = \arctan(k_{xr}/k_{yr})$. Right: Normalised fluid wave speed $c/c_f = k_f/\sqrt{k_{xr}^2 + k_{yr}^2}$.

surface vibration using a complex surface wavenumber $k_x = k_{xr} + \mathrm{i}k_{xi}$, where the real part relates to the surface vibration speed as $k_{xr} = \omega/c_v$ and the imaginary part provides an exponential attenuation $\mathrm{e}^{-k_{xi}x}$.

The complex surface wavenumber k_x makes $k_y = k_{yr} + \mathrm{i}k_{yi}$ complex as well. In fact, closer investigation of (2) reveals that *any* propagating ($k_{xr} > 0$) and attenuated ($k_{xi} > 0$) surface vibration leads to a radiating ($k_{yr} > 0$) fluid wave whose pressure increases exponentially with distance from the surface ($k_{yi} < 0$). (While the latter fact might at first seem troubling, [5] explains why this is the correct physical behaviour for the inhomogeneous fluid wave [2, 6] that an attenuated surface vibration radiates.)

We then investigate the properties of the radiated wave further. The left plot in Fig. 1 shows that if the surface vibration is not attenuated ($k_{xi} = 0$), the radiated time-averaged intensity I_y has a discontinuous singularity at the supersonic-subsonic transition and is zero in the subsonic domain. If the surface vibration is attenuated, however, I_y is smooth and continuous at the transition, showing power radiation in the entire subsonic domain. The middle plot in Fig. 1 shows that the fluid wave will only ever graze the surface ($\theta = 90°$) in the subsonic domain if the surface vibration is not attenuated. Finally, if the surface vibration is not attenuated, the right plot in Fig. 1 shows a sharp transition in the actual fluid wave speed c from the fluid sound speed c_f in the supersonic domain to the surface vibration speed c_v in the subsonic domain. For attenuated surface vibrations, this transition is smoothed due to the lower speed of the inhomogeneous radiated waves.

For a more physically realistic treatment, instead of simply imposing a particular attenuation of the surface vibration, we connect the radiated power to the power lost in the surface vibration. With a surface vibration power flow $P_x(x) = P_{x0}\,\mathrm{e}^{-2k_{xi}x}$, this implies $-\partial P_x/\partial x = 2k_{xi}P_x = I_y$ [5]. With I_y and potentially P_x depending on the variable k_{xr} and the unknown k_{xi}, valid propagation modes are represented by the roots of the function $f(k_{xr}, k_{xi}) = 2k_{xi} - I_{y0}(k_{xr}, k_{xi})/P_{x0}(k_{xr}, k_{xi})$ plotted in Fig. 2. The figure shows two such modes: One 'classic' non-radiating subsonic mode, and one radiating supersonic mode that extends into the subsonic domain, demonstrating very similar behaviour to the subsonic radiation shown for A_0 Lamb waves in [3–5].

To validate our results, we apply them to leaky A_0 Lamb waves on a 1 cm thick steel plate radiating into air on both sides. A number of perturbation methods already exist

ISBN 978-82-8123-021-7

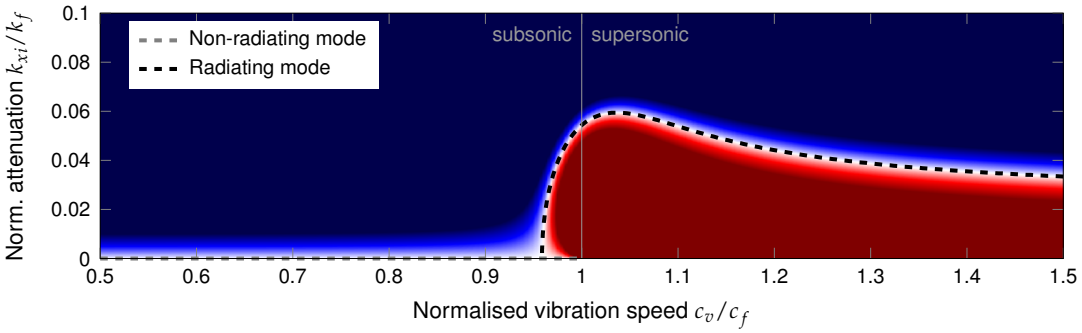

Figure 2: Diverging colour plot of the function $f(k_{xr}, k_{xi}) = 2k_{xi} - I_{y0}(k_{xr}, k_{xi})/P_{x0}(k_{xr}, k_{xi})$, with arbitrary values chosen for material constants and power flow. White colour and dashed lines indicate the function's roots ($f = 0$), which represent valid propagating modes.

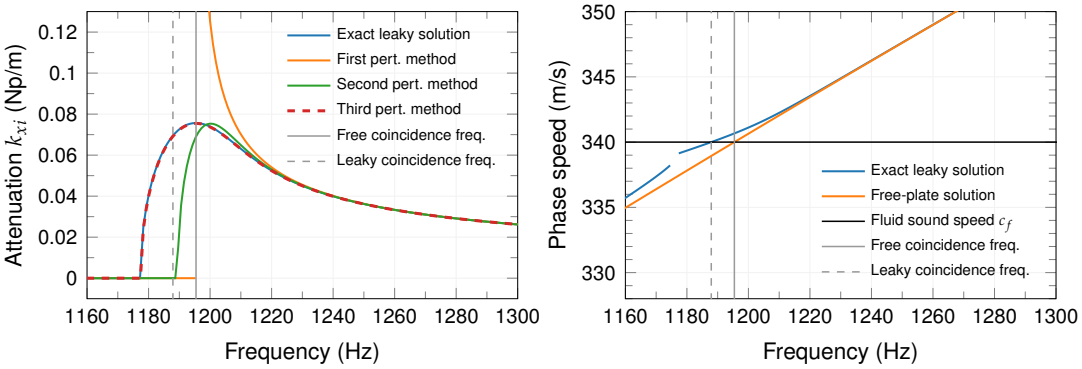

Figure 3: Comparison of exact leaky A_0 Lamb wave solutions for a 1 cm steel plate in air against approximate solutions. Left: Attenuation due to radiation. Right: Phase speed of leaky and free Lamb waves.

to predict the attenuation of leaky Lamb waves from free-plate solutions, as summarised in [7], but none of them can predict subsonic radiation. Our results can be used as an improved perturbation method to overcome this weakness. We base this perturbation on the dispersion relations $k_{xr}^{\text{free}}(\omega)$ and $k_{xr}^{\text{leaky}}(\omega)$ of free and leaky A_0 Lamb waves, respectively, in addition to the field equations for free Lamb waves. We then compare the results against the exact attenuation $k_{xi}^{\text{leaky}}(\omega)$.

The left plot in Fig. 3 shows our attenuation results. First, we calculate the attenuation based on the roots of $2k_{xi} - 2I_{y0}(k_{xr}^{\text{free}}, 0)/P_{x0}(k_{xr}^{\text{free}}, 0)$, i.e., as a simple perturbation to a non-attenuated surface vibration. This results in the same attenuation as existing perturbation methods, with no radiation in the subsonic domain. Second, we take the attenuation of the surface vibration into account, finding the roots of $2k_{xi} - 2I_{y0}(k_{xr}^{\text{free}}, k_{xi})/P_{x0}(k_{xr}^{\text{free}}, k_{xi})$. This results in the same qualitative behaviour as the exact solution, although the attenuation peak and cutoff frequencies are different. The reason for this difference is apparent from the phase speed of the free and leaky Lamb waves in the right plot in Fig. 3: Close to the supersonic-subsonic transition, the two diverge, leading to different coincidence frequencies. Third, we take this phase speed divergence into account by finding the roots of $2k_{xi} - 2I_{y0}(k_{xr}^{\text{leaky}}, k_{xi})/P_{x0}(k_{xr}^{\text{leaky}}, k_{xi})$. This shows a very good match with the exact solution, thus validating our results.

In summary, we have found that subsonic radiation occurs because any attenuated

ISBN 978-82-8123-021-7

surface vibration will radiate power into the fluid. Our simple power flow model, which connects the power radiated into the fluid to the power lost in the surface vibration, shows that such subsonic radiation can occur in a small area of the subsonic domain. Furthermore, we have shown that this model can be used as a perturbation method for leaky Lamb waves that improves on existing ones. A full match with the exact attenuation, however, requires using the exact phase speed, which itself is part of the exact leaky solution.

Acknowledgement

This work was supported by the Research Council of Norway under grant no. 237887.

References

[1] T. E. Vigran, *Building Acoustics*, 1st ed. CRC Press, 2008.

[2] V. Mozhaev and M. Weihnacht, "Subsonic leaky Rayleigh waves at liquid-solid interfaces," *Ultrasonics*, vol. 40, no. 1-8, pp. 927–933, 2002.

[3] H. Dabirikhah and C. W. Turner, "The coupling of the A_0 and interface Scholte modes in fluid-loaded plates," *The Journal of the Acoustical Society of America*, vol. 100, no. 5, pp. 3442–3445, 1996.

[4] D. A. Kiefer, M. Ponschab, S. J. Rupitsch, and M. Mayle, "Calculating the full leaky Lamb wave spectrum with exact fluid interaction," *The Journal of the Acoustical Society of America*, vol. 145, no. 6, pp. 3341–3350, 2019.

[5] D. A. Kiefer, M. Ponschab, and S. J. Rupitsch, "From Lamb waves to quasi-guided waves: On the wave field and radiation of elastic and viscoelastic plates," 2020, preprint published on ResearchGate, doi: 10.13140/RG.2.2.32631.44968.

[6] N. Declercq, R. Briers, J. Degrieck, and O. Leroy, "The history and properties of ultrasonic inhomogeneous waves," *IEEE Transactions on Ultrasonics, Ferroelectrics and Frequency Control*, vol. 52, no. 5, pp. 776–791, 2005.

[7] H. K. Arnestad and E. M. Viggen, "A fast semi-analytical method for propagating leaky Lamb wavefields," in *Proceedings of the 44th Scandinavian Symposium on Physical Acoustics*. Norwegian Physical Society, 2021, p. 22.

ISBN 978-82-8123-021-7

Håvard Kjellmo Arnestad

A Fast Simulation Method for Ultrasonic Wave Propagation in Coupled Non-parallel Plates

NTNU
Norwegian University of
Science and Technology